

**THE SEARCH FOR COMPACT BINARY  
COALESCENCE IN ASSOCIATION WITH SHORT  
GRBS WITH LIGO/VIRGO S5/VSR1 DATA**

By  
**Nickolas V Fotopoulos**

A THESIS SUBMITTED IN  
PARTIAL FULFILLMENT OF THE  
REQUIREMENTS FOR THE DEGREE OF

DOCTOR OF PHILOSOPHY

IN  
PHYSICS

at  
The University of Wisconsin–Milwaukee  
May 2010

**THE SEARCH FOR COMPACT BINARY  
COALESCENCE IN ASSOCIATION WITH SHORT  
GRBS WITH LIGO/VIRGO S5/VSR1 DATA**

By  
**Nickolas V Fotopoulos**

A THESIS SUBMITTED IN  
PARTIAL FULFILLMENT OF THE  
REQUIREMENTS FOR THE DEGREE OF

DOCTOR OF PHILOSOPHY

IN  
PHYSICS

at  
The University of Wisconsin–Milwaukee  
May 2010

---

Jolien Creighton

Date

---

Graduate School Approval

Date

# THE SEARCH FOR COMPACT BINARY COALESCENCE IN ASSOCIATION WITH SHORT GRBS WITH LIGO/VIRGO S5/VSR1 DATA

By

Nickolas V Fotopoulos

The University of Wisconsin–Milwaukee, 2010

Under the Supervision of Professor Jolien Creighton

## ABSTRACT

During LIGO's fifth science run (S5) and Virgo's first science run (VSR1), x-ray and gamma-ray observatories recorded 33 short, hard gamma-ray bursts (short GRBs), 22 of which had high quality data in two or more detectors. The most convincing explanation for the majority of short GRBs is that in the final stages of an inspiral between a neutron star and a companion compact object, the neutron star is tidally disrupted, providing material to accrete, heat, and eject on sub-second timescales. I describe a search for the gravitational-wave signatures of compact binary coalescence in the vicinity of short GRBs that occurred during S5/VSR1.

---

Jolien Creighton

Date

© Copyright 2010  
by  
**Nickolas V Fotopoulos**

*to*  
*Mom and Bub*

# TABLE OF CONTENTS

<b>Acknowledgments</b>	<b>ix</b>
<b>List of Tables</b>	<b>xi</b>
<b>List of Figures</b>	<b>xiv</b>
<b>1 Introduction</b>	<b>1</b>
<b>2 Short GRBs, CBCs, and gravitational waves</b>	<b>3</b>
2.1 Short gamma-ray burst phenomenology . . . . .	4
2.2 Gamma-ray burst detectors . . . . .	6
2.3 Compact binary coalescence progenitor model . . . . .	6
2.3.1 GRB-GW time delay . . . . .	8
2.4 Gravitational-wave theory . . . . .	10
2.4.1 Gravitational waves from linearized gravity . . . . .	11
2.4.2 The transverse-traceless (TT) gauge . . . . .	13
2.4.3 Gravitational waves from accelerating quadrupoles . . . . .	15
2.4.4 The energy transported by gravitational waves . . . . .	16
2.5 Gravitational waves from compact binary inspirals . . . . .	17
2.6 Science enabled by gravitational-wave detection of short GRBs . . . . .	19
<b>3 Gravitational-wave detectors</b>	<b>22</b>
3.1 Interferometric gravitational-wave detection: The road to $10^{-21}$ . . . . .	23
3.1.1 The Michelson laser interferometer . . . . .	24
3.1.2 Higher laser power . . . . .	25
3.1.3 Fabry–Perot resonant arm cavities . . . . .	26
3.1.4 Power recycling . . . . .	27

3.2	Geometry . . . . .	28
3.3	Initial LIGO and initial Virgo . . . . .	29
3.4	S5/VSR1 . . . . .	36
3.5	S5/VSR1 calibration . . . . .	37
<b>4</b>	<b>Identifying and ranking search candidates</b>	<b>41</b>
4.1	Deriving information from measurements, Bayesian-style . . . . .	42
4.2	Matched filtering . . . . .	45
4.2.1	The distribution of data with noise . . . . .	45
4.2.2	The distribution of data with signal and noise . . . . .	48
4.2.3	Matched filter signal-to-noise ratio . . . . .	49
4.3	Post-matched-filtering likelihood ratios . . . . .	49
4.3.1	Constructing a likelihood ratio . . . . .	51
4.3.2	The warts of actual implementation . . . . .	53
<b>5</b>	<b>Statistical interpretations</b>	<b>57</b>
5.1	Detection criteria . . . . .	57
5.1.1	Determining the threshold for a single GRB . . . . .	57
5.2	Constraining parameter space . . . . .	58
5.2.1	Exclusions and likelihood ratios for sub-populations . . . . .	61
5.2.2	Handling multi-modal distributions . . . . .	62
5.2.3	Handling empty trials . . . . .	63
5.2.4	Handling counting uncertainty . . . . .	64
5.3	Population statement . . . . .	64
<b>6</b>	<b>A pipeline for externally triggered CBC searches</b>	<b>67</b>
6.1	Experimental setup . . . . .	68
6.2	Data quality . . . . .	71
6.3	The role of H1-H2 in triggered and untriggered CBC searches . . . . .	71
6.4	The untriggered S5/VSR1 low-mass candidate-generation pipeline . . . . .	72
6.5	Waveform consistency tests . . . . .	75
6.6	Trigger consistency cuts in the untriggered search . . . . .	77
6.7	The triggered S5/VSR1 low-mass pipeline . . . . .	79
6.7.1	Modifications to untriggered candidate generation . . . . .	79

6.7.2	Pipeline superstructure . . . . .	80
<b>7</b>	<b>A worked example: GRB 070201</b>	<b>84</b>
7.1	The significance of GRB 070201 . . . . .	84
7.2	Data and data quality . . . . .	85
7.3	Diagnostics throughout the pipeline . . . . .	87
7.3.1	Template banks . . . . .	87
7.3.2	Single-detector distributions . . . . .	90
7.3.3	Coincidence cuts . . . . .	92
7.3.4	Waveform consistency cuts . . . . .	96
7.3.5	Effective SNR ranking . . . . .	100
7.3.6	Effective SNR ranking by chirp mass . . . . .	101
7.3.7	Likelihood-ratio ranking . . . . .	107
7.4	Significance . . . . .	118
7.5	Distance exclusion . . . . .	121
<b>8</b>	<b>The search for CBCs in association with short GRBs in S5/VSR1</b>	<b>129</b>
8.1	Sample selection . . . . .	131
8.2	Tuning . . . . .	133
8.3	Results . . . . .	134
8.3.1	Individual GRB results . . . . .	134
8.3.2	Distance exclusions . . . . .	137
8.3.3	Population statement . . . . .	139
8.3.4	Discussion . . . . .	140
<b>9</b>	<b>Epilogue</b>	<b>142</b>
	<b>Bibliography</b>	<b>144</b>

# Acknowledgments

The LIGO Scientific Collaboration has been a safe and nurturing home in which to mature as a scientist. Its members and the members of the Virgo Collaboration count among my greatest teachers and friends. The LIGO and Virgo instruments provided the data that are the basis for this dissertation and the start of my career. Thank you, National Science Foundation, for funding LIGO and being behind my funding. Thank you Italian Istituto Nazionale di Fisica Nucleare and the French Centre National de la Recherche Scientifique for funding Virgo.

Jolien Creighton and Patrick Brady, you taught me how to think, prioritize, and manage. You gave me every advantage and opportunity a grad student could have and I appreciate it from the bottom of my heart. Jolien, your gentle kindness, your ability to derive anything on the board, your C and  $\text{\LaTeX}$  mastery, and your ability to snatch flying, screaming monkeys from the air have been especially inspirational.

Alex Dietz, we have been close partners throughout the work contained in this thesis. Your enthusiasm and hard work made it possible and fun. Our live box-openings were a big hit and I think we produced a nice product together. Xavier Siemens and Warren Anderson, you've never led me astray. We work, play, and eat meat together and you have mentored me well in all of these.

To my dear GRBeings, thank you for taking part in this search. It was a genuine pleasure to work more closely with you. You gave me great insight and spotted a great many things that my untrained eyes missed. Thank you, Jordi Burguet-Castell, Damir Buskulic, James Clark, Steve Fairhurst, Andy Lundgren, Frédérique Marion, Valeriu Predoi, Alan Weinstein, and Peng Peng Yu.

There are so many others with whom I have fond memories of useful scientific discussion and mentorship that I cannot possibly hope to name you all. Thank you Rana Adhikari, Luis Anchordoqui, Stuart Anderson, Dani Atkinson, Stefan

Ballmer, Berit Behnke, Rahul Biswas, Marie-Anne Bizouard, Lindy Blackburn, Duncan Brown, Kipp Cannon, Sarah Caudill, Nelson Christensen, Jessica Clayton, Thomas Dent, Anamaria Effler, Missy Frei, Tobin Fricke, John Friedman, Stefanos Giampanis, Evan Goetz, Lisa Goggin, Romain Gouaty, Chad Hanna, Kari Hodge, Tomoki Isogai, Gareth Jones, Peter Kalmus, Vicky Kalogera, Shivaraj Kandhasamy, Jonah Kanner, Erik Katsavounidis, Keita Kawabe, Drew Keppel, Scott Koranda, Ben Lackey, Mike Landry, Albert Lazzarini, Isabel Leonor, Ilya Mandel, Vuk Mandic, Szabi Marka, Adam Mercer, Richard O'Shaughnessy, SangHoon Oh, Christian Ott, Chris Pankow, Pinkesh Patel, Larne Pekowski, Larry Price, Jocelyn Read, Tania Regimbau, Emma Robinson, Jamie Rollins, Lucía Santamaria-Lara, Peter Saulson, Antony Searle, Abhay Shah, Peter Shawhan, Jake Slutsky, Patrick Sutton, Michele Vallisneri, Ruslan Vaulin, Cheryl Vorvick, Michal Was, Matt West, John Whelan, Stan Whitcomb, Darren White, and Alan Wiseman.

Support staff are too often overlooked; you hold up the vast machinery of the scientific establishment and I am grateful. Thank you Meagan Bell, Mary Eckert, John Kempken, Steve Kennedy, Adam Miller, Brian Moe, Steve Nelson, Ross Oldenburg, Greg Skelton, Pamela Urban, Kate Valerius, and Marie Woods

Most of all, I thank my parents. You gave me every advantage and opportunity a son could be given, as well as a great deal of good food and travel. You granted me critical thinking, a high esteem for careful work, and some measure of emotional intelligence. I do my best for you.

# List of Tables

1	GRB detection capabilities of missions in the IPN . . . . .	7
2	Priors and ranges on simulation parameters . . . . .	110
3	On-source CBC candidates associated with GRB 070201 . . . . .	118
4	Parameters of the 22 GRBs selected for the S5/VSR1 search . . . . .	130
5	Summary of individual GRB search results . . . . .	135

# List of Figures

1	Geometry of the compact binary coalescence model of short GRBs . . .	9
2	Sketch of a Michelson interferometer . . . . .	24
3	Sketch of a Michelson interferometer with Fabry–Perot cavities . . . .	26
4	Sketch of a Michelson interferometer with Fabry–Perot cavities and power recycling . . . . .	27
5	LIGO strain sensitivities . . . . .	34
6	Primary known contributors to the H1 detector noise spectrum . . .	35
7	Histogram of LIGO BNS horizon distance during S5 . . . . .	36
8	LIGO’s differential arm length control loop . . . . .	38
9	Sketch of a frequentist confidence belt construction . . . . .	59
10	Experimental setup: segmentation . . . . .	70
11	Schematic of the untriggered S5/VSR1 CBC search pipeline . . . . .	76
12	Schematic of the triggered S5/VSR1 CBC search pipeline . . . . .	83
13	UV image of the M31 galaxy and the $3\sigma$ IPN error box of GRB 070201	86
14	A GRB 070201 template bank for H1 . . . . .	88
15	A GRB 070201 template bank for H2 . . . . .	89
16	SNR versus time for H1 and H2 around GRB 070201 . . . . .	91
17	Histograms of SNR for H1 and H2 around GRB 070201 . . . . .	91
18	SNR versus time for coincident H1–H2 triggers around GRB 070201 .	92
19	Histograms of SNR for H1 and H2 around GRB 070201 . . . . .	93
20	The second-stage GRB 070201 template bank for H1 . . . . .	94
21	The second-stage GRB 070201 template bank for H2 . . . . .	95
22	Second-stage SNR versus time for H1 and H2 around GRB 070201 . .	97
23	Histograms of second-stage SNR for H1 and H2 around GRB 070201	97
24	H2 SNR versus H1 SNR for second-stage coincident triggers around GRB 070201 . . . . .	98

25	$\chi^2$ versus $\rho$ for second-stage coincident triggers around GRB 070201 .	99
26	Zoomed $\chi^2$ versus $\rho$ for second-stage coincident triggers around GRB 070201 . . . . .	100
27	$r^2$ versus $\rho$ for second-stage coincident triggers around GRB 070201 .	101
28	H1 effective SNR versus H1 SNR for second-stage coincident triggers around GRB 070201 . . . . .	102
29	H2 effective SNR versus H2 SNR for second-stage coincident triggers around GRB 070201 . . . . .	103
30	H2 effective SNR versus H1 effective SNR for second-stage coincident triggers around GRB 070201 . . . . .	104
31	Combined effective SNR for off-source coincidences around GRB 070201	105
32	Combined effective SNR for clustered off-source coincidences around GRB 070201 . . . . .	106
33	False-alarm probability versus effective SNR for GRB 070201 . . . . .	108
34	Efficiency versus effective SNR for GRB 070201 . . . . .	109
35	Likelihood ratio versus effective SNR for GRB 070201 . . . . .	112
36	Maximum likelihood ratio versus maximum effective SNR for GRB 070201	114
37	ROC curve for maximum likelihood versus maximum effective SNR for GRB 070201 . . . . .	116
38	Efficiency versus distance for GRB 070201 . . . . .	117
39	Maximum likelihood ratio versus maximum effective SNR for GRB 070201 including the loudest event . . . . .	119
40	Significance of the maximum likelihood ratio for GRB 070201 . . . . .	120
41	Maximum likelihood ratios for sub-populations of GRB 070201 . . . . .	121
42	$\ln p(\Lambda(m_{\text{comp}})   D)$ and confidence belts for $m_{\text{comp}}$ between 19 and $22 M_{\odot}$ for GRB 070201 . . . . .	123
43	$\ln p(\Lambda(m_{\text{comp}})   D)$ and confidence belts for $m_{\text{comp}}$ between 19 and $22 M_{\odot}$ for GRB 070201 . . . . .	125
44	$\ln p(\Lambda(m_{\text{comp}})   D)$ and confidence belts for $m_{\text{comp}}$ between 19 and $22 M_{\odot}$ for GRB 070201 . . . . .	126
45	FC confidence intervals for all companion-mass sub-populations for GRB 070201 . . . . .	127
46	Cumulative FAPs for the most significant candidates for each GRB .	136

47 Lower 90% distance limits to NS–NS and NS–BH systems . . . . . 138

# Chapter 1

## Introduction

Gamma-ray bursts are extremely bright flashes of gamma-rays that originate at cosmological distances. The timescales, energetics, and sky locations suggest that many short-duration gamma-ray bursts arise in the final stages of the inspiral of a neutron star with another neutron star or black hole. In Newtonian gravity, two bodies will orbit one another indefinitely, tracing out the same paths every revolution. In Einstein's general relativity, some energy is lost every orbit, causing the orbit to gradually shrink until the bodies collide. The lost energy radiates away in the form of gravitational radiation or gravitational waves.

The Laser Interferometer Gravitational-Wave Observatory (LIGO), GEO600, and Virgo are ambitious efforts to detect gravitational waves. They are sensitive to the alternating squeezings and stretchings of spacetime that are gravitational waves. Gravitational waves will give us new observational handles on the dynamics of the mass and energy of violent astrophysical events. Scientific interest in LIGO and

Virgo continues to grow, with prominent appearances in the Astro2010 Decadal Survey [1, 2, 3, 4] and with over 665 authors from the LIGO and Virgo collaborations on the latest observational results [5]. Detecting gravitational waves in association with the usual electromagnetic signatures will revolutionize astronomy.

This thesis details the why and how of joint electromagnetic and gravitational-wave observations, particularly as applied to short gamma-ray bursts. Chapter 2 contains a review of the phenomenology of short gamma-ray bursts and the compact binary coalescence progenitor model, plus a derivation of the gravitational-wave signal of interest. Chapter 3 contains a description of the LIGO and Virgo detectors, built to detect those gravitational waves. Chapter 4 will build a theoretical framework for detecting the known signals in noise-dominated data streams. Chapter 5 will describe techniques for relating detection or non-detection back to statements about the universe. Chapter 6 will describe a workflow for processing data to generate gravitational-wave signal candidates taking into account the real-world limitations of data handling. The application of this pipeline to the event GRB 070201 is presented in Chap. 7 and the results of the search pipeline as applied to all short GRBs in the LIGO/Virgo S5/VSR1 science run appears in Chap. 8. Finally, I discuss the significance of the work and what the future holds for the field in Chap. 9.

## Chapter 2

# Short GRBs, CBCs, and gravitational waves

The past decade has seen dramatic progress in the understanding of gamma-ray bursts (GRBs), intense flashes of gamma-rays that are observed to be isotropically distributed over the sky (see, e.g., [6, 7] and references therein). The short-time variability of the bursts indicates that the sources are very compact. GRBs are directly observed with gamma-ray and X-ray satellites in the Interplanetary Network [8] such as *HETE*, *Swift*, *Konus-Wind*, *INTEGRAL*, and *Fermi* (see [9, 10, 11, 12, 13] and references therein).

In Sec. 2.1, I summarize observations of short gamma-ray bursts, followed in Sec. 2.3 by the community's current best guess as to the progenitors. Section 2.4 steps through the basics of gravitational-wave theory and Sec. 2.5 derives the Newtonian-order gravitational-wave signal for the inspiral phase of a compact

binary coalescence. Finally, Sec. 2.6 will spell out what science we can extract from observations of compact binary coalescence in association with a short GRB.

## 2.1 Short gamma-ray burst phenomenology

GRBs are usually divided into two types [14, 15], distinguished primarily by the duration of the prompt burst. Long-duration bursts with a duration of  $\gtrsim 2$  s are generally interpreted to be associated with hypernova explosions in star-forming galaxies. Several nearby long GRBs have been spatially and temporally coincident with core-collapse supernovae as observed in the optical [16, 17, 18, 19]. Follow-up observations by X-ray, optical, and radio telescopes of the sky near long GRBs have yielded detailed measurements of afterglows from more than 500 GRBs to date; some of these observations resulted in strong host-galaxy candidates, which allowed redshift determination for more than 200 bursts [20]. Similar followups of short GRBs seldom find afterglows and the afterglows that are detected are significantly dimmer than long GRB afterglows. Besides host galaxy identification, afterglow light-curves provide many clues to the post-burst activity of the central engine, to the local environment of the progenitor system, and to the beaming angle. Only 3 short GRBs have measured late-time afterglows at the time of this writing [21].

The majority of short GRBs, with a duration  $\lesssim 2$  s, are thought to arise from the coalescence of a neutron star (NS) with another compact object (see [21] and

references therein), such as a NS or black hole (BH). There is growing evidence that finer distinctions may be drawn between bursts [22, 23]. For example, it is estimated that up to  $\sim 15\%$  of short GRBs could be associated with soft gamma repeaters [24, 25], which emit bursts of X-rays and gamma rays at irregular intervals with lower fluence than compact binary coalescence engines [26, 27]. While long GRBs follow the Amati relation, which relates the isotropic-equivalent energy release to the redshift-corrected peak spectral energy, short GRBs have been shown to not follow the relation [28].

Short GRBs are exceedingly bright [21], emitting  $E_{\gamma}^{\text{iso}} \approx 10^{49}\text{--}10^{51}$  erg isotropic equivalent energy in  $\sim\text{MeV}$  gamma rays per burst, or  $L_{\gamma}^{\text{iso}} \approx 10^{50}\text{--}10^{52}$  erg/s in luminosity. Isotropic equivalent energy refers to an extrapolation of a burst's apparent brightness assuming that the outflow is isotropic rather than beamed. For comparison, long GRBs are slightly brighter at  $E_{\gamma}^{\text{iso}} \approx 10^{52}\text{--}10^{54}$  erg and  $L_{\gamma}^{\text{iso}} \approx 10^{50}\text{--}10^{52}$  erg/s. A solar mass of energy is  $M_{\odot}c^2 \approx 10^{54}$  erg and the Milky Way galaxy outputs  $L_{\text{MW}} \approx 10^{44}$  erg/s. The gravitational binding energy of a binary neutron star system released in the last few orbits is  $\Delta E_{\text{GW}} \approx 10^{53}$  erg, which can explain the energetics of a short GRB with even a small fraction of the energy being converted to gamma-rays.

Redshift and afterglow light curve measurements exist for only three short GRBs at present [21]. Of these, only one has a clean light curve in which the jet break is obvious. From the jet break of GRB 051221, the jet opening angle is  $0.16 \text{ rad} \approx 9.2^{\circ}$ .

## 2.2 Gamma-ray burst detectors

Of paramount importance to a search for gravitational waves in association with short GRBs is a well localized sky position and Earth-crossing time. In the time of LIGO's S5 science run, described further in Sec. 3.4, there were 213 reported GRBs. Of these, 178 had their sky positions localized by *Swift*, 15 by INTEGRAL, 2 by HETE, 1 by SuperAGILE, and 17 by the triangulation of multiple instruments in the Interplanetary Network (IPN). Some capabilities of current IPN missions are summarized briefly in Table 1. All IPN missions have wide field-of-view gamma-ray detectors and a few are far enough from planets to have an unoccluded view of the sky. Of the IPN missions, *Swift*, *Fermi*, INTEGRAL, and SuperAGILE have the capability of following up an initial, poorly localized detection with onboard imaging telescopes, allowing refined sky localization and a deeper observation of GRB light curves.

## 2.3 Compact binary coalescence progenitor model

In the compact binary coalescence model of short GRBs, a NS and compact companion in otherwise stable orbit lose energy to gravitational waves and inspiral. Disruption of the NS(s) provides matter, which can be ejected in relativistic jets. The prompt gamma-ray emission is widely thought to be created by internal shocks, the interaction of outgoing matter shells at different velocities, while the afterglow is

Mission / Experiment	Time resolution s	Energy keV	Orbit	Distance from Earth light seconds
RHESSI	Time-tagged	30–10000	LEO	0.024
<i>Fermi</i> GBM	Time-tagged	8–1000	LEO	0.024
SuperAGILE/MCAL	Time-tagged	10–40/300–100000	LEO	0.024
<i>Suzaku</i> HXD	0.016	50–5000	LEO	0.024
<i>Swift</i> BAT	Time-tagged	15–150	LEO	0.024
INTEGRAL SPI-ACS	0.050	> 80	Eccentric	0.5
<i>Konus-Wind</i>	0.002	15–10000	Sun–Earth L1	4.6
<i>Mars Odyssey</i> GRS	0.032	50–10000/30–1300	Mars orbit	1000
MESSENGER GRNS	1.0	40–200	En route to Mercury	600

Table 1 : GRB detection capabilities of missions in the IPN at the end of 2009. Time-tagged means that the detector assigns each photon an individual time-stamp rather than counting photons within a fixed integration time. LEO stands for low-earth orbit. This table was adapted from [29].

thought to be created by external shocks—the interaction of the outflowing matter with the interstellar medium.

### 2.3.1 GRB-GW time delay

A critical parameter in searching for gravitational-wave counterparts to GRBs is the difference in their arrival times at the Earth.

Several semianalytical calculations of the final stages of a NS–BH inspiral show that the majority of matter plunges onto the BH within 1 s [30]. Numerical simulations of the mass transfer suggest a timescale of milliseconds [31] or some seconds at most [32]. Also, it has been found in simulations that the vast majority of the NS matter is accreted onto the BH directly and promptly (within hundreds of milliseconds) without a torus that gets accreted later [33, 34].

In the current GRB fireball model [7, 21], some combination of mass and Poynting flux carries energy away in jets along the rotational axis of the final BH. The central engine can be highly variable in power over a timescale shorter than its total duration. If significant fraction of the ejecta are outflowing at Lorentz factor  $\Gamma \gg 1$ , we imagine that the variability will be of order  $\Gamma$  also. A second outflow with Lorentz factor  $2\Gamma$  a time  $\delta t_{\text{engine}}$  later will impact the first outflow at a distance  $r_{\text{sh}}$  from the engine. As measured by an observer at infinity at rest with respect to the engine,  $r_{\text{sh}} \approx \frac{8}{3}c\delta t_{\text{engine}}\Gamma^2$ , where  $v$  is the velocity corresponding to  $\Gamma$ . Assuming that gravitational waves propagate at the speed of light, the delay between the signals will be the path difference, as in Fig. 1. With this naïve picture, the total time

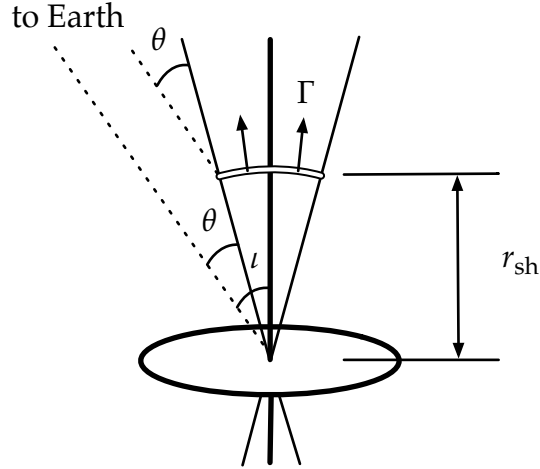


Figure 1 : Geometry of the compact binary coalescence model of short GRBs.  $r_{\text{sh}}$  is the distance between the central engine and the inner shock.  $\iota$  is the inclination angle, which is the angle between the line of sight of Earth and the orbital axis. Although we generally believe that Earth is within the jet opening angle, we depict the angle  $\theta$  between our line of sight with the engine and our line of sight with the nearest outflow direction for generality.

delay observed at Earth will be

$$\begin{aligned} \delta t_{\text{GW-EM}} &= \frac{r_{\text{sh}}}{v} - \frac{r_{\text{sh}}}{c} \cos \theta \\ &= \frac{8}{3} \delta t_{\text{engine}} \Gamma^2 (1 - \cos \theta) , \end{aligned} \quad (2.1)$$

where  $\theta$  is the angle between our line of sight to the central engine and our line of sight to the internal shock. Note that  $\theta$  is distinct from the inclination angle  $\iota$ , which is the angle between our line of sight and the orbital angular momentum vector. The central engine's dynamical timescale is between the light-crossing time of the final BH and the plunge time of the NS matter, so we take  $t_{\text{engine}} \approx 10$  ms. Short GRBs have Lorentz factors  $\Gamma$  measured to be in the range 10–50 [21]. To receive a substantial gamma-ray flux at Earth, it is reasonable to assume that we are within

the jet opening angle. Setting  $\theta = 0$  gives  $\delta t_{\text{GW-EM}} = 0$  ms. At maximum, we must be within  $\theta \approx 1/\Gamma$  of the shock front, which gives  $\delta t_{\text{GW-EM}} \approx 40$  ms. We dismiss the interstellar and intergalactic media as contributing to the time delay, as the index of refraction at these energies ( $1 \text{ MeV} = 2.4 \times 10^{20} \text{ Hz}$ ) is negligible.

Thus, if the speed of gravitational radiation equals the speed of light as we expect, then for an observer in the cone of the collimated outflow, the gravitational-wave inspiral signal will arrive within a second before the electromagnetic signal from internal shocks.

## 2.4 Gravitational-wave theory

Wheeler captures the essence of General Relativity with the phrase [35]:

Spacetime grips mass, telling it how to move;

And mass grips spacetime, telling it how to curve.

More specifically, Einstein's equation tells us how spacetime curves in response to the matter, energy, and motion within it. The motion of a free-falling point-particle will follow a locally straight path through the curved spacetime, a geodesic of the curved spacetime. In general, the motion of matter is captured in the equations of covariant conservation.

### 2.4.1 Gravitational waves from linearized gravity

Einstein's equation is

$$G_{\alpha\beta} = \frac{8\pi G}{c^4} T_{\alpha\beta}, \quad (2.2)$$

where  $G_{\mu\nu}$  is the Einstein curvature tensor,  $T_{\mu\nu}$  is the stress-energy tensor,  $G$  is Newton's gravitational constant, and  $c$  is the speed of light. The Einstein tensor is related to the Ricci curvature by

$$G_{\alpha\beta} = R_{\alpha\beta} - \frac{1}{2} g_{\alpha\beta} R, \quad (2.3)$$

where  $R \equiv g^{\alpha\gamma} R_{\alpha\gamma}$ ,  $R_{\alpha\gamma} \equiv R_{\alpha\beta\gamma}{}^{\beta}$ , and  $R_{\alpha\beta\gamma}{}^{\delta}$  is the Riemann curvature tensor. We see that the left-hand side of Eq. (2.2) is purely curvature and the right-hand side is purely stress-energy. The matter equations of motion are

$$\nabla_{\alpha} T^{\alpha}{}_{\beta} = 0, \quad (2.4)$$

where  $\nabla_{\alpha}$  is the metric-compatible covariant derivative.

We linearize the equations by considering the metric

$$g_{\mu\nu} = \eta_{\mu\nu} + h_{\mu\nu}, \quad (2.5)$$

where  $\eta_{\mu\nu}$  is the Minkowski spacetime metric and  $h_{\mu\nu}$  is a small perturbation. I choose the sign convention that  $\eta_{\mu\nu} = \text{diag}(-1, 1, 1, 1)$ . In Cartesian coordinates associated with the flat metric  $\eta_{\mu\nu}$ , the linearized Riemann tensor has the form

$$R_{\alpha\beta\gamma\delta} = \frac{1}{2} (-\partial_{\alpha}\partial_{\gamma}h_{\beta\delta} + \partial_{\alpha}\partial_{\delta}h_{\beta\gamma} + \partial_{\beta}\partial_{\gamma}h_{\alpha\delta} - \partial_{\beta}\partial_{\delta}h_{\alpha\gamma}) + \mathcal{O}(h^2). \quad (2.6)$$

If we introduce the trace-reversed perturbation  $\bar{h}_{\mu\nu} = h_{\mu\nu} - \frac{1}{2}\eta_{\mu\nu}h$ , we obtain the field equations

$$-\square\bar{h}_{\alpha\beta} - \eta_{\alpha\beta}\partial^\gamma\partial^\delta\bar{h}_{\gamma\delta} + \partial^\gamma\partial_\alpha\bar{h}_{\beta\gamma} + \partial^\gamma\partial_\beta\bar{h}_{\alpha\gamma} = \frac{16\pi G}{c^4}T_{\alpha\beta}, \quad (2.7)$$

where  $\square \equiv \partial_\alpha\partial^\alpha$  is the D'Alembertian operator.

Coordinate transformations or gauge transformations alter metric perturbations as

$$h_{\alpha\beta} \rightarrow h_{\alpha\beta} + \partial_\alpha\zeta_\beta + \partial_\beta\zeta_\alpha. \quad (2.8)$$

This form of transformation admits the gauge condition

$$\partial^\alpha\bar{h}_{\alpha\beta} = 0. \quad (2.9)$$

With this choice, called the Lorenz gauge, the field equations simplify to

$$\square\bar{h}_{\alpha\beta} = -\frac{16\pi G}{c^4}T_{\alpha\beta} + \mathcal{O}(h^2), \quad (2.10)$$

which in vacuum ( $T_{\alpha\beta} = 0$ ) are manifestly wave equations.

The vacuum solutions of Eq. (2.10) are

$$\bar{h}_{xx} = \bar{h}_{xx}(ct - z), \quad (2.11)$$

$$\bar{h}_{yy} = \bar{h}_{yy}(ct - z), \quad (2.12)$$

$$\bar{h}_{xy} = \bar{h}_{xy}(ct - z) = \bar{h}_{yx}, \quad (2.13)$$

where the other components are zero by the Lorenz gauge condition of Eq. (2.9).

The coordinates are also rotated so that the waves propagate in the  $z$  direction.

Unreversing the trace, we find our metric perturbations

$$h_{xx} = \frac{1}{2} (\bar{h}_{xx} - \bar{h}_{yy}) \quad (2.14)$$

$$h_{yy} = \frac{1}{2} (\bar{h}_{yy} - \bar{h}_{xx}) \quad (2.15)$$

$$h_{xy} = \bar{h}_{xy} = h_{yx} . \quad (2.16)$$

### 2.4.2 The transverse-traceless (TT) gauge

It is informative to simplify the gravitational-wave solution further by considering monochromatic waves. Other waves can be expressed as a superposition of monochromatic waves. Consider solutions of the form

$$\bar{h}_{\mu\nu} = A_{\mu\nu} \cos(k_\alpha x^\alpha), \quad (2.17)$$

where  $A_{\mu\nu}$  is a constant, symmetric tensor specifying any polarization and amplitude information and  $k_\alpha$  is a null vector specifying the direction and frequency. The Lorenz gauge condition of Eq. (2.9), requires that

$$k^\mu A_{\mu\nu} = 0. \quad (2.18)$$

That is, if  $A_{\mu\nu}$  is spatial, then the wave is transverse. Spatial means that  $u^\mu A_{\mu\nu} = 0$  for some time-like vector  $u^\mu$ .

Equation (2.18) is 4 constraints on 10 parameters (10 independent matrix components;  $A_{\mu\nu}$  is symmetric). Further gauge transformations of the form of Eq. (2.8) can be used to force the wave to be trace-free and purely spatial. We choose the infinitesimal gauge transformation with  $\zeta^\mu = C^\mu \sin(k_\alpha x^\alpha)$ .  $A_{\mu\nu}$  therefore transforms

as

$$A_{\mu\nu}^{\text{TT}} = A_{\mu\nu} + C_\mu k_\nu + C_\nu k_\mu - \eta_{\mu\nu} C_\beta k^\beta. \quad (2.19)$$

The transverse-traceless requirement on  $A_{\mu\nu}^{\text{TT}}$  can be restated as constraints on  $C_\beta$ . In particular, we'd like to demand that the components of the polarization are spatial and that the tensor is traceless. That is,

$$A_{\mu\nu}^{\text{TT}} u^\mu = 0 \quad (2.20)$$

$$\eta^{\mu\nu} A_{\mu\nu}^{\text{TT}} = 0, \quad (2.21)$$

where  $u^\mu$  is a time-like vector. This is the TT gauge. Note that as there is no trace,  $h_{\mu\nu} = \bar{h}_{\mu\nu}$ . Although it appears that there are 5 constraints here, there are only 4, as the Lorenz gauge condition already constrains the  $k^\mu$  direction.

As mentioned above, linearity allows us to determine a TT gauge for the general solution  $h_{\mu\nu}$  above. Thus,

$$h_{0\mu}^{\text{TT}} = 0 \quad (2.22)$$

$$h_{ij}^{\text{TT}} = h_{ij}^{\text{TT}}(ct - z) \quad (2.23)$$

$$\partial_j h_{ij}^{\text{TT}} = 0 \Rightarrow h_{iz}^{\text{TT}} = 0 \quad (2.24)$$

$$h_{xx}^{\text{TT}} + h_{yy}^{\text{TT}} = 0. \quad (2.25)$$

With the gauge fixed, the perturbed metric is left with two degrees of freedom. We define  $h_{xx}^{\text{TT}} = -h_{yy}^{\text{TT}} \equiv h_+$  and  $h_{xy}^{\text{TT}} = h_{yx}^{\text{TT}} \equiv h_\times$ , the only two independent functions in the  $h_{\mu\nu}$ . We can thus express the full gravitational-wave tensor as a sum over polarizations

$$h_{ij}^{\text{TT}} = h_+ e_{ij}^+ + h_\times e_{ij}^\times \quad (2.26)$$

$$e_{ij}^+ = \begin{pmatrix} 0 & 0 & 0 & 0 \\ 0 & 1 & 0 & 0 \\ 0 & 0 & -1 & 0 \\ 0 & 0 & 0 & 0 \end{pmatrix} \quad (2.27)$$

$$e_{ij}^\times = \begin{pmatrix} 0 & 0 & 0 & 0 \\ 0 & 0 & 1 & 0 \\ 0 & 1 & 0 & 0 \\ 0 & 0 & 0 & 0 \end{pmatrix}. \quad (2.28)$$

### 2.4.3 Gravitational waves from accelerating quadrupoles

So far, we've explored the dynamics of gravitational waves in the radiation zone, but they were produced somehow. We consult our wave equation, Eq. (2.10), with the source term intact for guidance. Rewrite the wave equation as

$$\begin{aligned} \square \bar{h}^{\mu\nu} &= -\frac{16\pi G}{c^4} T^{\mu\nu} + \mathcal{O}(h^2) \\ &\equiv -\frac{16\pi G}{c^4} (T^{\mu\nu} + t^{\mu\nu}) \\ &\equiv -\frac{16\pi G}{c^4} \tau^{\mu\nu}, \end{aligned} \quad (2.29)$$

where  $\tau^{\mu\nu}$  is the effective stress-energy, containing both real stress-energy, the stress-energy of gravitational waves, and other nonlinear contributions. The latter are important in near-zone physics, where perturbations from flatness are extreme. As an extreme example of where the latter term dominates, consider binary black hole orbits, for which  $T^{\mu\nu} = 0$ . The effective stress-energy satisfies

$$\partial^\alpha \tau_{\alpha\beta} = 0 \quad (2.30)$$

by the gauge condition Eq. (2.9). This condition is sufficient that we may treat  $\tau^{\alpha\beta}$  exactly as a stress-energy and with all the usual properties thereof.

Far away from a compact system, to leading order in the slow-motion limit we obtain

$$h_{ij}^{\text{TT}} = \frac{2G}{c^4 r} \frac{\partial^2}{\partial t^2} \mathcal{J}_{ij}^{\text{TT}}(ct - r) \quad (2.31)$$

$$\mathcal{J}^{ij}(t) = \int \left( x^i x^j - r^2 \delta^{ij} \right) \tau^{00}(t, \vec{x}) d^3x. \quad (2.32)$$

That is, the gravitational wave amplitude varies inversely with our distance from the source  $r$  and linearly with the second time-derivative of the quadrupole moment of the effective energy. Note that  $\mathcal{J}_{ij}$  is measurable within or near the dynamical system of interest, while  $\mathcal{J}_{ij}^{\text{TT}}$  involves projections within the observer's frame. Note also that the moment of inertia  $I_{ij} = \int x^i x^j \tau^{00}(t, \vec{x}) d^3x$  is equally as good as  $\mathcal{J}_{ij}$  in this calculation, as it differs only in the trace. The full multipole expansion is worked out in great detail in [36].

#### 2.4.4 The energy transported by gravitational waves

Returning to Eq. (2.29), we can evaluate the leading-order stress-energy of gravitational waves explicitly. It is

$$T_{\mu\nu}^{\text{GW}} = \frac{c^4}{32\pi G} \left\langle \frac{\partial h^{\text{TT}ij}}{\partial x^\mu} \frac{\partial h_{ij}^{\text{TT}}}{\partial x^\nu} \right\rangle. \quad (2.33)$$

The average  $\langle \cdot \rangle$  is over a volume, necessary to make the quantity gauge invariant. The volume should be over several wavelengths so that boundary terms vanish, but small enough that geodesics do not cross.

The energy carried away in gravitational waves can also be expressed in terms of the quadrupole moment. Substituting the stress-energy tensor, Eq. (2.33), into the quadrupole formula, Eq. (2.32), we obtain the energy flux and luminosity

$$\begin{aligned} \frac{dE}{dt dA} &= T_{0z}^{\text{GW}} = -T_{00}^{\text{GW}} \\ &= -\frac{c^3}{32\pi G} \left\langle \frac{\partial h^{\text{TT}ij}}{\partial t} \frac{\partial h_{ij}^{\text{TT}}}{\partial t} \right\rangle \\ &= -\frac{G}{8\pi c^5 r^2} \left\langle \ddot{\mathcal{J}}^{\text{TT}ij} \ddot{\mathcal{J}}_{ij}^{\text{TT}} \right\rangle \end{aligned} \quad (2.34)$$

$$\begin{aligned} L &= -\int \frac{dE}{dt dA} dA \\ &= \frac{G}{5c^5} \left\langle \ddot{\mathcal{J}}^{ij} \ddot{\mathcal{J}}_{ij} \right\rangle. \end{aligned} \quad (2.35)$$

## 2.5 Gravitational waves from compact binary inspirals

Imagine two point particles in circular orbit. Let us find the gravitational radiation from this binary system, using otherwise Newtonian physics to describe the orbit and the second time-derivative of its quadrupole moment.

In a Cartesian coordinate system with the center of mass at the origin and the orbital angular momentum axis along the  $z$  axis, the moment of inertia tensor is

$$I = \frac{1}{2} \mu a^2 \begin{pmatrix} \frac{1}{2}(1 + \cos 2\phi) & \sin 2\phi & 0 \\ \sin 2\phi & \frac{1}{2}(1 + \cos 2\phi) & 0 \\ 0 & 0 & 0 \end{pmatrix}, \quad (2.36)$$

where  $a$  is the orbital separation,  $\mu = m_1 m_2 / M$  is the reduced mass,  $M = m_1 + m_2$  and  $\phi$  is the orbital phase. The observer sits at polar angle  $\iota$ . By straightforward

application of Eq. (2.32), gives

$$h_+ = -\frac{2\mu a^2 \omega^2}{D} \cos 2\phi (1 + \cos^2 \iota) \quad (2.37)$$

$$h_\times = -\frac{4\mu a^2 \omega^2}{D} \sin 2\phi \cos \iota, \quad (2.38)$$

where  $D$  is the distance between the source and the observer and  $\omega = d\phi/dt$  is the angular velocity of the orbit. Note that the gravitational wave oscillates at twice the frequency of the orbit:  $f_{\text{GW}} = 2f_{\text{orb}}$ .

The gravitational-wave luminosity saps energy from the system at a rate of

$$L_{\text{GW}} = \frac{32c^5}{5G} \eta^2 \left(\frac{v}{c}\right)^{10}, \quad (2.39)$$

where  $v = a\omega = (\pi GM f_{\text{GW}})^{1/3}$  and  $\eta = \mu/M$ . By the Virial Theorem, the energy of the orbit is  $E_{\text{N}} = -\frac{1}{2}\mu v^2$ . Equating  $L = -dE_{\text{N}}/dt$ , we obtain a differential equation for  $dv/dt$ . Substituting this into  $df/dt = df/dv \cdot dv/dt$  and making judicious use of Kepler's second law, we find that

$$\frac{df}{dt} = \frac{96c^6}{5G^2} \frac{\eta}{\pi M^2} (\pi GM f)^{11/3}. \quad (2.40)$$

Finally, we introduce a new quantity called the chirp mass,  $\mathcal{M} = \eta^{3/5} M = \mu^{3/5} M^{2/5}$  and its analogue, the chirp time,  $\mathcal{M}_t = G\mathcal{M}/c^3$  and obtain our final waveform

$$h_+(t) = -\frac{c\mathcal{M}_t}{D} \frac{1 + \cos^2 \iota}{2} \left(\frac{t_c - t}{5\mathcal{M}_t}\right)^{-1/4} \cos \left[ 2\phi_c - 2 \left(\frac{t_c - t}{5\mathcal{M}_t}\right)^{5/8} \right] \quad (2.41)$$

$$h_\times(t) = -\frac{c\mathcal{M}_t}{D} \cos \iota \left(\frac{t_c - t}{5\mathcal{M}_t}\right)^{-1/4} \sin \left[ 2\phi_c - 2 \left(\frac{t_c - t}{5\mathcal{M}_t}\right)^{5/8} \right], \quad (2.42)$$

where  $t_c$  is the coalescence time, i.e. when the frequency diverges to infinity. The behavior of such a waveform is to begin monotonically, then rise quickly in frequency and amplitude near the coalescence time. Waveforms of this form are often called “chirps”.

Post-Newtonian corrections don’t alter the qualitative form very much.  $\mathcal{M}$  remains a crucial parameter, giving us poor insight into the component masses  $m_1$  and  $m_2$ . As  $\mathcal{M}$  sets the timescale of the chirp, we measure a redshifted chirp mass  $\mathcal{M}(1+z)$  for sources at cosmological distances. To make cosmological measurements, it is important to note that  $D$  is the luminosity distance. (For a review of cosmological distance measures, see the pedagogical article [37].)

## 2.6 Science enabled by gravitational-wave detection of short GRBs

Compact binary coalescence is anticipated to generate strong gravitational waves in the sensitive frequency band of Earth-based gravitational-wave detectors [38]. The direct detection of gravitational waves associated with a short GRB would provide the critical evidence that the progenitor is indeed a compact binary. With such a detection it would be possible to measure component masses [39, 40], measure component spins [41], constrain NS equations of state [42, 43], and test general relativity in the strong-field regime [44]. Furthermore, measurement of luminosity distance [45], which would translate into a measurement of the Hubble expansion and dark energy that does not rely upon other rungs in the cosmic distance ladder.

Mass and spin determinations and confirmations of general relativity are long-understood aspects. The NS equation of state is a highly coveted measurement that has occupied x-ray astronomy for many years. Understanding what equations of state are allowed has ramifications for the standard model of particle physics as well as astronomy. Recent work has found that while there are many physical models for NS interiors, yielding many different equations of state, one can parametrize the equations by a small number of parameters with reasonable fidelity, allowing each observational constraint to rule out large swaths of parameter space and a large number of models at once [46]. Gravitational-wave measurements of binary NSs with Advanced LIGO at a distance of 100 Mpc will constrain the radius of a NS to within  $\sim 1$  km [43].

The past decade has been widely trumpeted as the era of precision cosmology. The era began with the COsmic Background Explorer (COBE), which earned its leaders the 2006 Nobel Prize. COBE was followed by the Wilkinson Microwave Anisotropy Probe (WMAP) [47], which measured the cosmic microwave background with greater precision, by the Sloan Digital Sky Survey (SDSS), which measured the baryon acoustic peak in the large-scale distribution of luminous red galaxies [48], and the Hubble Key Project that traced out the distance-redshift relationship of Type Ia supernovae [49]. Type Ia supernovae are found to be “standard candles”; that is, their absolute luminosity is known, so a measurement of flux from such an event tells us its distance. Compact binary coalescence detections will give us luminosity distance but with gravitational-wave measurements alone, we

cannot disambiguate the chirp mass from the redshift. A coincident electromagnetic measurement will provide measurements of the sky position and, with some luck, a galaxy association, which provides the redshift. Unfortunately, the luminosity distance is somewhat degenerate with the inclination angle, modifying the early optimistic estimates of the precision with which we can measure the Hubble constant and the dark energy equation of state. Estimates depend on the exact network of gravitational-wave detectors available in the Advanced detector era, but a 1% measurement of the Hubble constant is possible [45].

## Chapter 3

# Gravitational-wave detectors

LIGO [50], Virgo [51], and GEO600 [52] are the world's most sensitive gravitational-wave observatories. Initial LIGO consists of three power-recycled Michelson laser interferometers: an interferometer with 4 km-long, ultra-high-vacuum, Fabry-Perot cavities and power recycling at Livingston, LA, USA, named L1, and two located at Hanford, WA, USA, named H1 and H2, with arm lengths of 4 km and 2 km, respectively. The Virgo detector, named V1, is located at Cascina, Italy and has a similar configuration to the LIGO instruments, but with arms 3 km in length. These instruments have broadband sensitivity to differential changes in arm lengths around 100 Hz, which is well matched to the strain induced by incident gravitational-waves from low-mass compact binary coalescences. Construction and commissioning of LIGO alone took several years with hundreds of scientists and engineers and roughly  $\$3 \times 10^8$  in capital investment plus over  $\$3 \times 10^7/\text{yr}$  for operations.

GEO600 has turned out to be a proving ground for advanced interferometer

technology, donating components and designs to the other detectors. Its most sensitive operation is at higher frequencies than LIGO or Virgo, around 350 Hz. During the S5/VSR1 science run in which LIGO and Virgo ran at design sensitivities, GEO600 underwent upgrades. GEO600 instead participated in an Astrowatch science run (A5) in the epoch between S5/VSR1 and S6/VSR2. Astrowatch was a joint run between H2 and G1 to watch for serendipitous events such as a galactic supernova or other rare, nearby event. As G1 was not used for any analysis described in this thesis, I include no further discussion of it.

Section 3.1 contains the principles of gravitational-wave detection and the road to achieving the desired sensitivity. In Sec. 3.2 I describe detector sensitivity with respect to the sky position. Section 3.3 contains a summary of the operational configurations of Initial LIGO and Virgo instruments. In Sec. 3.4 I describe the S5/VSR1 science run, which contains the data analyzed in this thesis. Section 3.5 describes what goes into the calibration of photodiode counts to strain and gives the final uncertainties for the S5/VSR1 run.

### **3.1 Interferometric gravitational-wave detection: The road to $10^{-21}$**

A gravitational wave has the effect of alternately stretching and squeezing the spatial separation between two suspended mirrors. The counts at one's photodetector must be gauge-invariant. In a gauge where squeezing and stretching is in the time direction, this will have the effect of modulating the flow of time and alter the laser

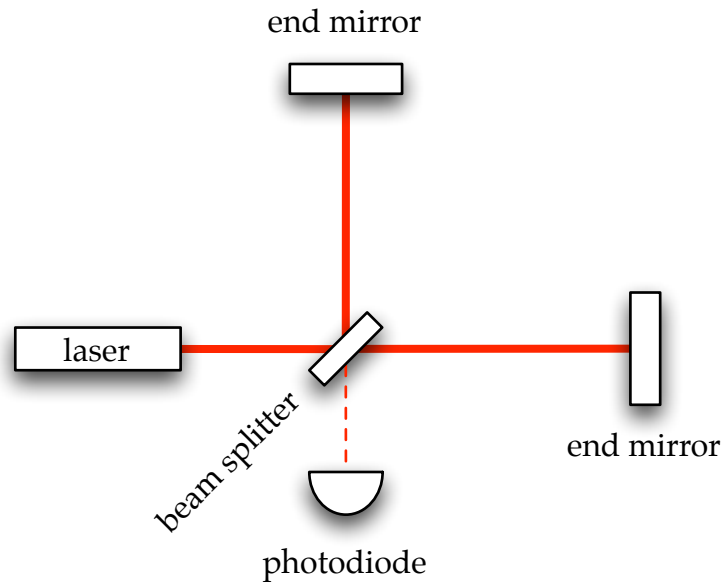


Figure 2 : Sketch of a Michelson interferometer

frequency in an analogous way.

Here I present a simple-minded, classical estimate of interferometer strain response, highlighting the basic elements necessary for operation at the astrophysically interesting strain sensitivity of  $10^{-21}$ .

### 3.1.1 The Michelson laser interferometer

Figure 2 depicts a simple Michelson interferometer with a laser source. If the arm lengths are equal ( $L_1 = L_2 \pmod{\lambda_{\text{laser}}}$ ), the light will recombine at the beam splitter in such a way that all of the power is reflected to the laser and no light is transmitted to the photodetector. A differential displacement of the end mirrors induces a difference in the phase advance of the light in each arm  $\delta(\Delta\phi) = 2\pi(\Delta L_1 - \Delta L_2)/\lambda_{\text{laser}}$ .

With little effort, we can detect a quarter wavelength shift just by seeing 0 intensity on our photodiodes go to maximum intensity. Our sensitivity is thus

$$\delta L_{\text{detectable}} \approx \frac{1}{4} \lambda_{\text{laser}} \quad (3.1)$$

$$\begin{aligned} h_{\text{detectable}} &= \frac{\delta L_{\text{detectable}}}{L} \\ &\approx \frac{1 \mu\text{m}}{4 \cdot 4 \text{ km}} \\ &\approx 10^{-10}, \end{aligned} \quad (3.2)$$

where we have used the LIGO values of  $\lambda_{\text{laser}} = 1064 \text{ nm} \approx 1 \mu\text{m}$  and  $L_1 = L_2 = 4 \text{ km}$ .

From this baseline of  $10^{-10}$ , let us review what other improvements we must make to reach our target of  $10^{-21}$ . Each revolves around resolving a smaller and smaller fraction of a fringe.

### 3.1.2 Higher laser power

In reality, we can resolve phase differences much smaller than a quarter cycle. The statistics of Poisson processes sets the uncertainty of a measurement of  $N$  photons at  $\sqrt{N}$ . Initial LIGO operated with  $P_{\text{laser}} \approx 10 \text{ W}$  [53]. The rate of photons at the beam splitter is

$$\dot{N}_\gamma = \frac{P_{\text{laser}}}{hc/\lambda_{\text{laser}}} \quad (3.3)$$

$$\approx \frac{10 \text{ W} \cdot 10^{-6} \text{ m}}{(6 \times 10^{-34} \text{ J} \cdot \text{s})(3 \times 10^8 \text{ m/s})} \quad (3.4)$$

$$\approx 10^{20} \gamma/\text{s}. \quad (3.5)$$

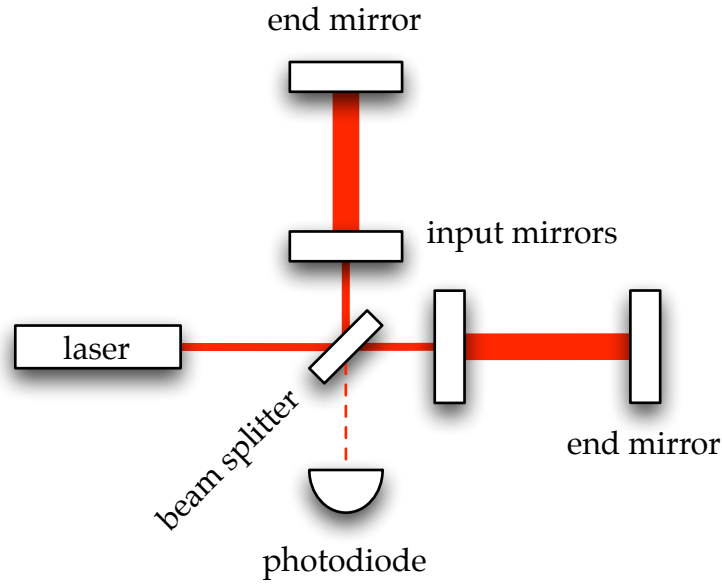


Figure 3 : Sketch of a Michelson interferometer with Fabry-Perot cavities

If we collect photons for  $1/f \approx 10$  ms, we can resolve down to  $\sqrt{f/\dot{N}_\gamma} \approx 10^{-9}$  of a fringe at 100 Hz. This leaves us at a strain sensitivity of

$$h \approx 3 \times 10^{-19} . \quad (3.6)$$

### 3.1.3 Fabry-Perot resonant arm cavities

By inserting input mirrors between the beam splitter and the end mirrors and adjusting them to resonance, one sets up Fabry-Perot cavities. The effect is to allow the light to repeatedly traverse the arm length before eventually returning to the beam splitter. This will magnify the phase shift by a factor equal to the average number of bounces  $G_{\text{arm}}$ . For initial LIGO, the reflectivity of the input mirrors was adjusted to give  $G_{\text{arm}} \approx 130$ . Note that this improves sensitivity for

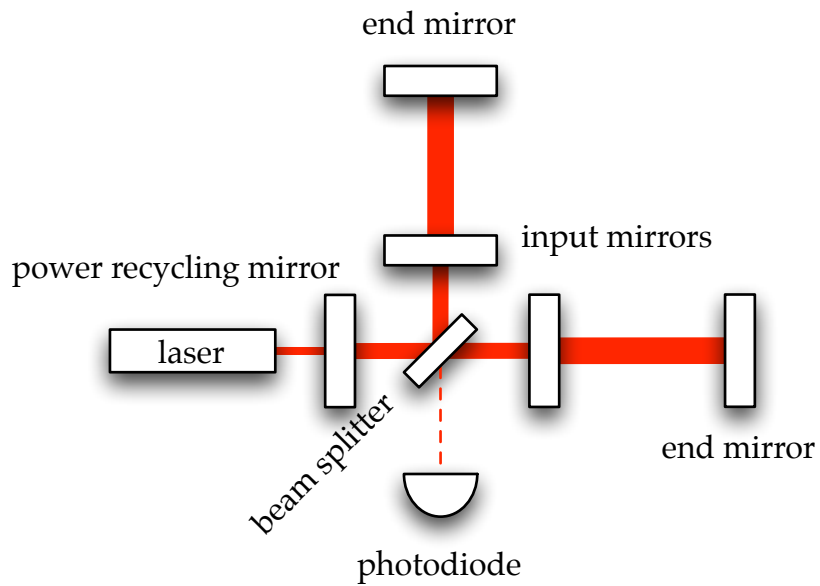


Figure 4 : Sketch of a Michelson interferometer with Fabry-Perot cavities and power recycling

gravitational-wave frequencies at low frequencies, but for frequencies near or above  $f_{\text{arm}} = c/(2\pi G_{\text{arm}}L) \approx 91 \text{ Hz}$ , the so-called cavity pole, there will be a sensitivity reduction, as the gravitational-wave amplitude will change sign over the light storage time  $\tau_{\text{arm}} = \pi/f_{\text{arm}}$  and begin to cancel itself.

With Fabry-Perot cavities, the strain sensitivity at 100 Hz is

$$h \approx 3 \times 10^{-21}. \quad (3.7)$$

### 3.1.4 Power recycling

With the insertion of a power recycling mirror between the laser and beam splitter, as in Fig. 4, and tuning it to resonance, we can increase the power at the beam splitter, increasing our sensitivity further. By tuning the reflectivity of the power

recycling mirror, a power gain of  $G_{\text{pr}} \approx 40^2$  can be achieved. The strain sensitivity is then

$$h \approx 6 \times 10^{-23} \quad (3.8)$$

at 100 Hz. The power recycling gain is determined by the absorptive losses of the optics in the interferometer and  $G_{\text{arm}}$ .

## 3.2 Geometry

One can find a very careful computation of the electromagnetic wavefront propagation through an interferometer in the presence of a gravitational wave in [54] and a vastly simplified derivation based on Killing vectors in [55]. The bottom line is that interferometer response, the difference in phase between the beams recombining at the beam splitter, is

$$h \propto \delta(\Delta\phi) \propto \frac{1}{2}(\hat{\zeta}^l \hat{\zeta}^m - \hat{\xi}^l \hat{\xi}^m) h_{lm}(\hat{k}) \quad (3.9)$$

$$\equiv F_+ h_+ + F_\times h_\times, \quad (3.10)$$

where we have taken the long-wavelength limit ( $fL/c \ll 1$ ) so that we are instantaneously sampling the gravitational waveform,  $\hat{\zeta}$  and  $\hat{\xi}$  are the directions of the interferometer arms, and  $\hat{k}$  is the gravitational wave's propagation direction. The antenna pattern functions  $F_+$  and  $F_\times$  encode the projection between the  $+$  and  $\times$  polarizations as defined in the radiation basis and their definitions in the detector

basis. Their explicit forms are

$$F_+(\theta, \phi, \psi) = -\frac{1}{2}(1 + \cos^2 \theta) \cos 2\phi \cos 2\psi - \cos \theta \sin 2\phi \sin 2\psi \quad (3.11)$$

$$F_\times(\theta, \phi, \psi) = \frac{1}{2}(1 + \cos^2 \theta) \cos 2\phi \sin 2\psi - \cos \theta \sin 2\phi \cos 2\psi, \quad (3.12)$$

where  $\theta$  and  $\phi$  are the spherical polar coordinates of the source in the detector frame and  $\psi$  is the third Euler angle in the Z-X-Z convention of Euler angles, as per Figure 8 in [56], and is frequently called the polarization angle.

Since the polarization angle  $\psi$  is unknown a priori, it is often useful to use the detector response function, also called the beam pattern or the antenna pattern

$$F_{\text{sum}}(\theta, \phi) = \sqrt{F_+^2(\theta, \phi, \psi) + F_\times^2(\theta, \phi, \psi)}. \quad (3.13)$$

The factor is the ratio between the amplitude read by the detector and the amplitude if the source were located directly overhead ( $\theta = \phi = 0$ ), holding all other parameters constant. It is constant with respect to  $\psi$ . The detector response function ranges between 0 and 1. It is plotted in figure 9 of [56]. The most sensitive directions are along the axis orthogonal to the arms, with  $F_{\text{sum}} = 1$ . There are four nulls along the axes  $45^\circ$  from the arms within the detector plane with  $F_{\text{sum}} = 0$ . Along the arms,  $F_{\text{sum}} = 0.5$ .

### 3.3 Initial LIGO and initial Virgo

Initial LIGO and initial Virgo are power-recycled Michelson interferometers with Fabry-Perot arm cavities, as outlined in the preceding sections. LIGO has two

4 km-long interferometers and one 2 km-long interferometer and Virgo has an interferometer with 3 km-long arms. A great deal more than optical configuration went into their design, however. Here is a short list of components go into a real instrument, with all numbers being correct for LIGO and mostly being close for Virgo. A much more complete description can be found in [50] for LIGO and [51] for Virgo.

1. RF readout. Initial instruments used an RF oscillator to induce sidebands of the carrier frequency of the laser. The carrier was held resonant in the entire instrument, but the sidebands were held resonant only in the power-recycling cavity and not in the Fabry–Perot cavities. The sidebands leaked out at the output photodiode providing some light so that phase response was linear rather than quadratic. The gravitational-wave signal was then extracted from its beating against the sidebands [57].
2. Laser frequency stabilization. The expressions given for strain sensitivity were given assuming a constant  $\lambda_{\text{laser}}$ . While lasers are highly monochromatic, even LIGO’s custom-built, pre-stabilized laser is variable to the level of  $10^{-7} \text{ Hz}/\sqrt{\text{Hz}}$  [53]. It gains additional stability from feedback from larger reference cavities. That is, if the laser frequency drifts slightly off resonance, laser power in the cavity will decrease, with longer cavities giving greater sensitivity. Detecting a decrease, one can adjust the length of the lasing cavity to return to resonance. The input mode cleaner provides a 12 m optical cavity

and the Fabry–Perot arms themselves provide an 8 km reference cavity via common mode ( $L_1 + L_2$ ), which is sufficient for high-sensitivity operation [58].

3. Seismic isolation. At low frequencies, seismic noise limits the sensitivity. Multiple-stage stacks of pendulums suspend the major optics (input, output, and recycling mirrors, plus the beam splitter), isolating them from ground motion [59]. L1 employed active isolation, where seismic motion was actively compensated, resulting in a factor of 10 improvement in isolation [60].
4. Acoustic isolation. The optical tables housing the input and output optics couple to the environment of the corner stations via sound, as they are outside of vacuum. The tables are kept in isolation rooms with specialized anechoic foam to damp sound around the tables around 100 Hz, the most sensitive gravitational-wave frequencies.
5. Optical suspensions. The major optics must be suspended to prevent seismic coupling, but the suspensions themselves introduce noise. A great deal of engineering has gone into pushing the suspensions' violin modes to narrow frequency bands, far from the sensitive regions and providing low thermal noise [61].
6. Optical coatings. Thermal noise from the surface of the optics is the dominant noise source in part of our detectors' sensitive bands. New coatings have been

explored to achieve the required low-absorption, low-noise operation [62].

7. Dust removal. A dust particle that wanders into the beam will scatter and absorb light, causing a dip in photodiode readings, which could potentially register as a signal. Stringent vacuum protocol, dust counters, and positive pressure near the in-air optics all contribute to dust mitigation.
8. Scattered light baffles. Stray light can cause photodiodes to make erroneous measurements. A beam that is partially reflected onto a wall can backscatter into a photodiode. The situation is worse with H1 and H2, as there are two interferometers within the same vacuum system. When one instrument loses lock, the stray light causes very obvious noise in the readout of the other. Baffles reduce the potential for scattered light [63].
9. Thermal compensation. With the immense laser power built up in the Fabry–Perot cavities, even an absorption of a few parts per million will cause an optic to heat significantly and non-uniformly. The heating pattern will cause thermal expansion, which will warp the mass, changing the optical properties of the system and introducing undesirable, higher optical modes. The thermal compensation system shines a second laser on the input mirrors in an annular pattern to make the heating, and thus the surface deformation, uniform.
10. Tidal compensation. The ocean obviously deforms in response to solar and lunar tidal fields, but so does the crust of the Earth. Interferometer optical

suspensions are bolted to the ground, and flow with the very low frequency ground motion. One must compensate for the slow drift of the arm lengths to avoid reaching the limits of the finer mirror actuation.

11. Control systems. The instruments are vast and complex. Beyond the obvious problem of length sensing and control, elaborated upon in Sec. 3.5, the angular pointing of dozens of optical components must be controlled very precisely in order for light to bounce hundreds of times between mirrors 4 km apart. The temperature of many components needs regulation. Thermal compensation requires feedback to know how strongly to fire the annular laser beam. The laser intensity and frequency must be continuously adjusted to maintain the required stability. All of these require a real-time data acquisition and control system [64].
12. Vacuum system. Air would disperse the laser, causing unacceptable absorptive loss and distortion of the wavefront. A major capital investment was the multi-kilometer vacuum system to encase the beam and major optics plus a concrete outer shell for protection. The system maintains  $10^{-9}$  Torr, which is ultra-high vacuum.
13. And many more...

Seemingly miraculously, LIGO and Virgo have been constructed and have achieved low-noise operation. LIGO sensitivities during the science run S5/VSR1 are depicted in Fig. 5. Detailed discussion of the noise sources and control systems

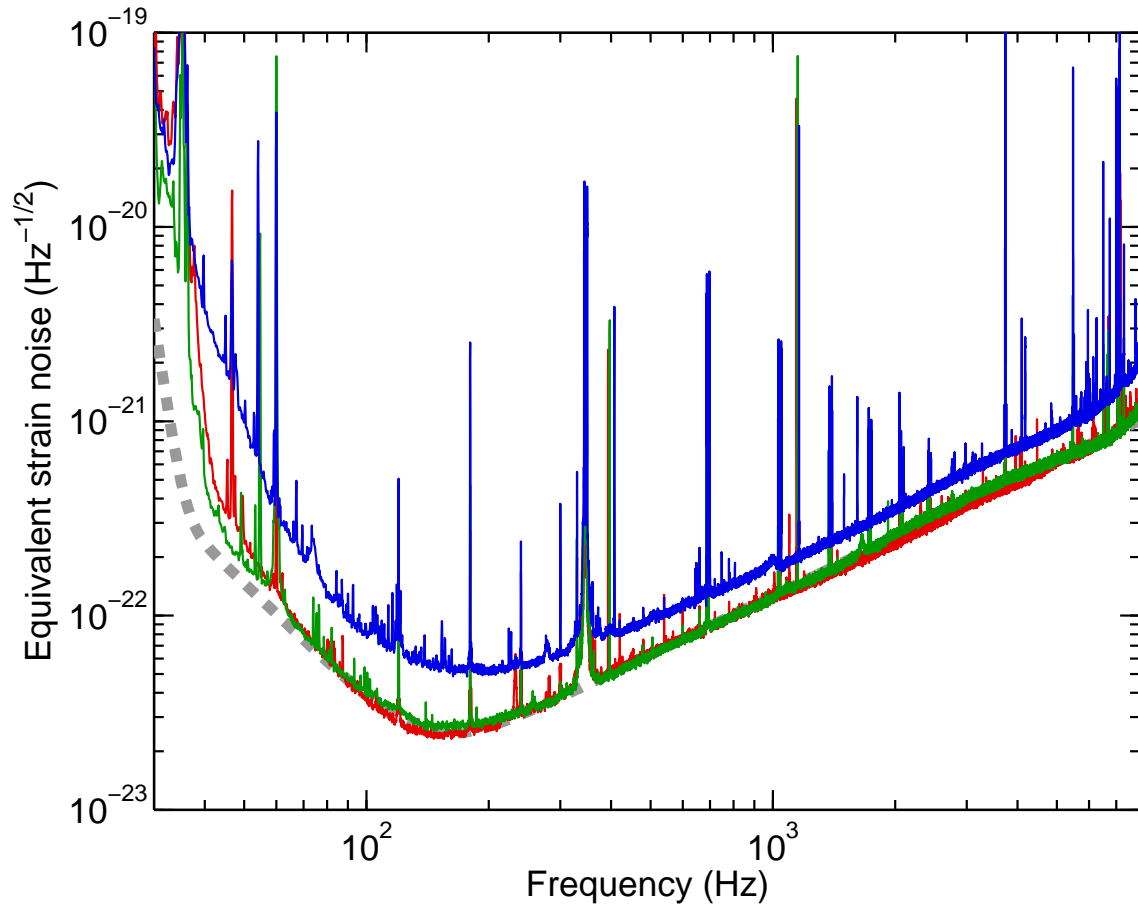


Figure 5 : Strain sensitivities, expressed as amplitude spectral densities of detector noise converted to equivalent GW strain. The vertical axis denotes the rms strain noise in 1 Hz of bandwidth. Shown are typical high sensitivity spectra for each of the three interferometers (red: H1; blue: H2; green: L1), along with the design goal for the 4 km detectors (dashed grey). The figure and caption have been reproduced from figure 6 of [50].

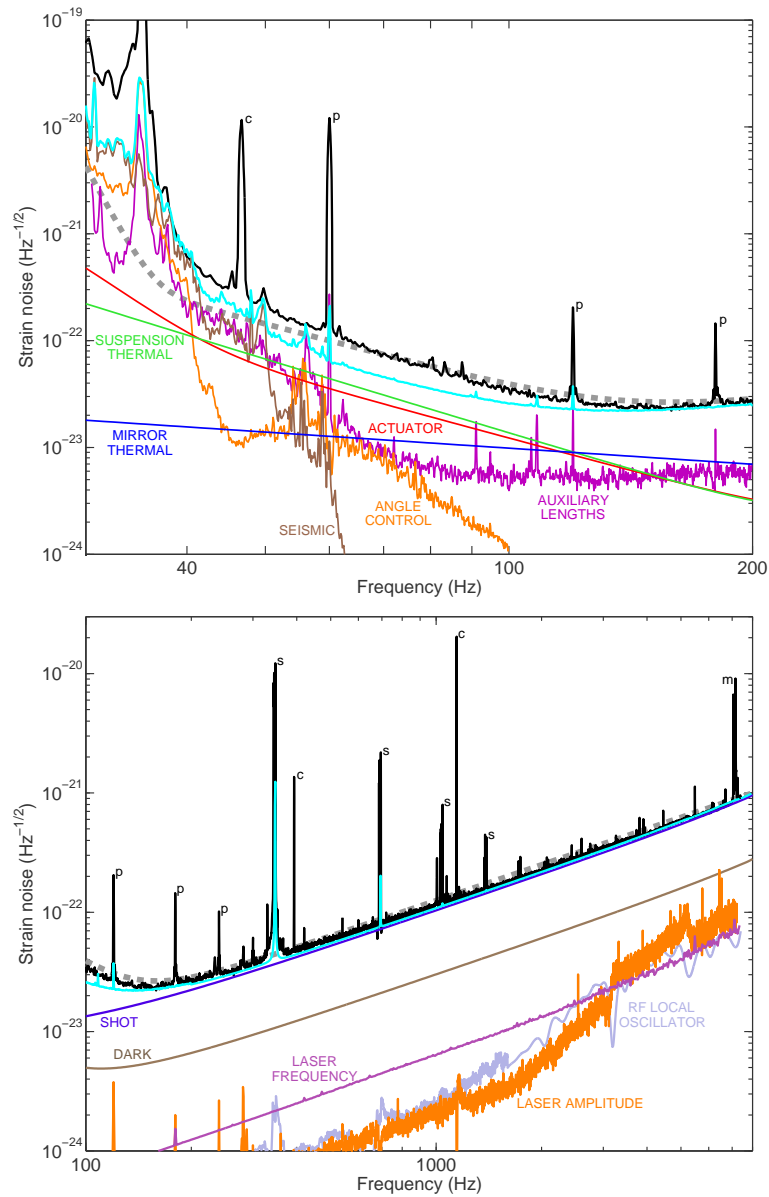


Figure 6 : Primary known contributors to the H1 detector noise spectrum. The upper panel shows the displacement noise components, while the lower panel shows sensing noises (note the different frequency scales). In both panels, the black curve is the measured strain noise (same spectrum as in Fig. 5), the dashed gray curve is the design goal, and the cyan curve is the root-square-sum of all known contributors (both sensing and displacement noises). The labelled component curves are described in the text. The known noise sources explain the observed noise very well at frequencies above 150 Hz, and to within a factor of 2 in the 40–100 Hz band. Spectral peaks are identified as follows: c, calibration line; p, power line harmonic; s, suspension wire vibrational mode; m, mirror (test mass) vibrational mode. The figure and caption have been reproduced from figure 7 of [50].

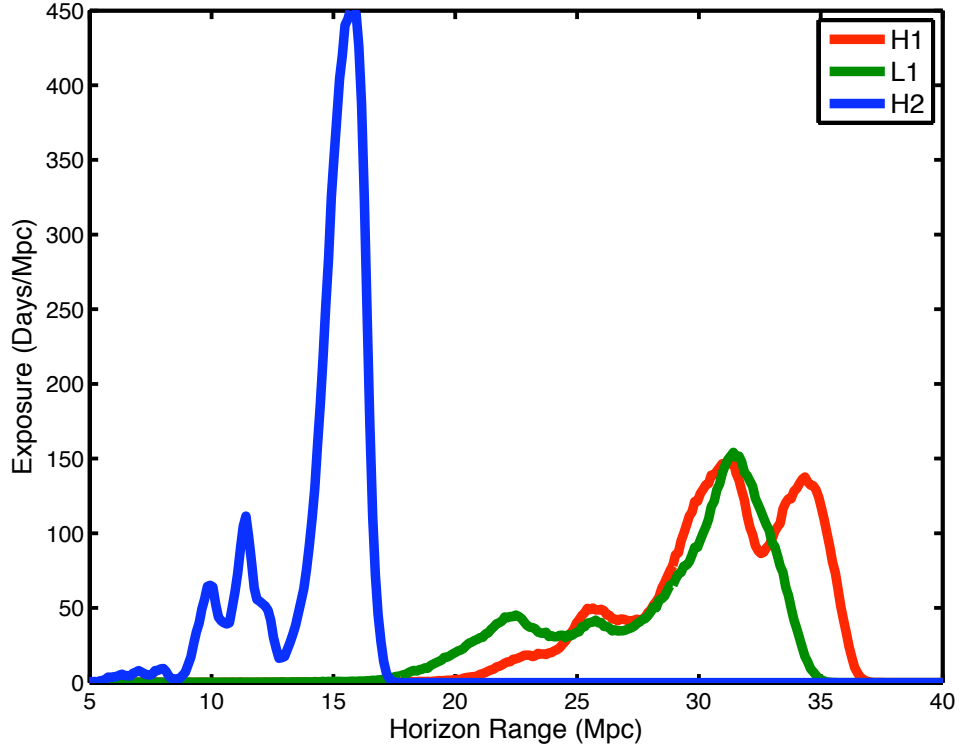


Figure 7 : Histogram of LIGO BNS horizon distance during S5. The horizon distance is the distance to which each interferometer would detect an optimally oriented binary neutron star inspiral at a matched-filter SNR of 8.

can be found in [58]. Figure 6 shows many of the known sources of noise for H1 for illustration.

### 3.4 S5/VSR1

In this thesis, I report on a search for gravitational-wave inspiral signals associated with the short GRBs that occurred during the fifth science run (S5) of LIGO, from 2005 November 4 to 2007 September 30, and the first science run (VSR1) of Virgo, from 2007 May 18 to 2007 September 30. S5 represents the combined operation of

the three LIGO detectors at the NSF-contracted design sensitivity. Figure 7 shows the distribution of distances to which we could detect an optimally oriented binary neutron star system at a matched-filter SNR of 8 over the run. The multi-modal structure reflects upgrades that occurred during the run.

During the S5/VSR1 joint run, 212 GRBs were discovered by different satellite missions (39 of them during VSR1 times), 33 of which we classified as search targets (8 of them in VSR1 times), by the criteria of Sec. 8.1.

In S5/VSR1, LIGO and Virgo operated as a global network. The coincident detection of a gravitational-wave signal allows triangulation of signals, yielding sky localization [65]. In the context of searching for GRB counterparts, this acts as a constraint to reduce background. As an aside, the sky localization can also be used to trigger electromagnetic followup of gravitational-wave candidates. This latter mode will become increasingly important, especially for discovering new astrophysical phenomena.

### **3.5 S5/VSR1 calibration**

I have so far given a simple description of the optical configuration and readout scheme, omitting detailed discussion of the interlocking control loops necessary for stable interferometer operation. The differential arm length must be held constant in order to maintain a dark fringe at the output photodiode. To compensate for drift and shaking, we alter the differential arm length by electromagnetically actuating

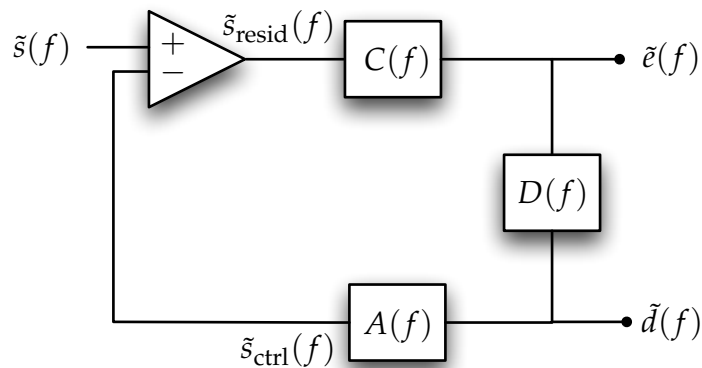


Figure 8 : LIGO's differential arm length control loop

the end mirrors. This extra motion will appear in the photodiode readout, which complicates the interpretation of the readout. We must correct for our intervention in deriving the signal  $s(t)$  that contains the gravitational-wave component and understand what errors enter the measurement.

Figure 8 shows the differential arm length control loop used in LIGO. Therein,  $\tilde{s}(f)$  is the Fourier transform of the gravitational-wave channel  $s(t)$  that we wish to measure.  $\tilde{e}(f)$  is the Fourier transform of LSC-DARM.ERR, the primary readout channel from which  $\tilde{s}(f)$  is derived.  $\tilde{d}(f)$  is the Fourier transform of LSC-DARM.CTRL, an important control channel that feeds back on the end mirrors.  $C(f)$  is the sensing function, characterizing the interferometer's response to strain,  $D(f)$  is a digital, low-pass filter with unity gain set to 40 Hz, and  $A(f)$  is the actuation function, characterizing the mirrors' response to magnetic actuation. Of these,  $D(f)$  and  $A(f)$  are found to be quite static, while  $C(f)$  tends to fluctuate in overall amplitude,

but not in its spectral shape. To this end,  $\gamma(t)$  is used to correct for changes in the instrument sensitivity from drifting input power, drifting alignment, and other slowly varying factors.

$$C(t, f) = \gamma(t)C_0(f) \quad (3.14)$$

With this, it is common to define the open loop gain  $G(t, f)$  and the response function of the interferometer  $R(t, f)$  as

$$G(t, f) = C(t, f)A(f)D(f) \quad (3.15)$$

$$R(t, f) = \frac{1 + G(t, f)}{C(t, f)}. \quad (3.16)$$

Note that we don't measure  $\tilde{s}(f)$  directly; we must infer it from our actual measured values in the control loop. Tracing the signals around the loop, we obtain

$$\tilde{s}(f) = \frac{1 + G(t, f)}{C(t, f)}\tilde{e}(f). \quad (3.17)$$

Actually,  $C(f)$  is not directly measurable, so we infer it from  $G(f)$ ,  $D(f)$ , and  $A(f)$ .  $G(f)$  is fit to a model, whose parameters can be measured by adding a series of loud sinusoids to  $\tilde{d}(f)$  and seeing the response in the readout  $\tilde{e}(f)$ .  $D(f)$  is known since it is composed of digital filters that we insert manually.  $A(f)$  is primarily the response of a pendulum to a driving force, but it also contains some information about the digital electronics that drive the electromagnetic coils that push the mirrors; this is all captured in a model, with a few parameters set by fitting.  $\gamma(t)$  is measured 16 times per second by monitoring the amplitude response to a few sinusoidal excitation signals that actuate an end mirror. These are called calibration lines and they run persistently.

The dominant uncertainties in  $\tilde{s}(f)$  come from measurement uncertainties of  $G(f)$  and  $A(f)$ . They are quantified by comparing the differences between measurements of these spectra and the analytical models. The overall sign of  $G(f)$  is a matter of convention, but important and difficult to make consistent. The final S5/VSR1 calibration is uncertain to 10% for H1 and H2, 13% for L1, and 6% for V1 [66]. The absolute timing accuracy is better than  $\pm 10 \mu\text{s}$ .

## Chapter 4

# Identifying and ranking search candidates

In this chapter, we'll develop the toolkit necessary for the detection of compact binary coalescences (CBCs). For greater depth in the mathematics of signal processing and the likelihood ratio, I recommend Wainstein and Zubakov's very clear textbook treatment [67]. I will not expound upon alternate formulations, but stick to my favorite route to the results I want to describe.

In Sec. 4.1 I introduce the Bayesian framework that will be used to derive the later results of the chapter. Section 4.2 contains a derivation of matched filtering, a sensitive technique for searching for signals of a known form. Matched filtering is optimal for Gaussian noise and is a core part of the LIGO-Virgo CBC search pipeline. It is useful to present the derivation of matched filtering here to set notation and to convey that our final likelihood-ratio method is a natural extension.

Section 6.5 holds discussion of signal consistency tests, a means of combatting the non-Gaussian component of the noise that characterizes real data, and shows how to fold these tests along with the matched filtering SNR into a refined detection statistic. In Sec. 4.3 I develop a post-matched-filtering likelihood-ratio statistic that handles the variation of background rate across signal parameter space as well as the relative efficiency of different instrument combinations.

#### 4.1 Deriving information from measurements, Bayesian-style

Bayesian probability theory gives us the framework to quantitatively inform a set of starting beliefs with measurements. We'd like to know  $p(\mathcal{H} | \vec{s})$ , the conditional probability density of the model or hypothesis  $\mathcal{H}$  given data  $\vec{s}$ . It relies upon what we believed about the model beforehand, encoded in the prior  $p(\mathcal{H})$ , and what the model predicts for the data, encoded in the likelihood  $p(\vec{s} | \mathcal{H})$ . Here is Bayes' Theorem:

$$p(\mathcal{H} | \vec{s}) = \frac{p(\vec{s} | \mathcal{H})p(\mathcal{H})}{p(\vec{s})}, \quad (4.1)$$

Bayes' Theorem relates the posterior probability  $p(\mathcal{H} | \vec{s})$  on the left-hand side to the likelihood  $p(\vec{s} | \mathcal{H})$ , prior  $p(\mathcal{H})$ , and distribution of data  $p(\vec{s})$  on the right-hand side. The prior  $p(\mathcal{H})$  reflects one's knowledge about the model. What percent chance do you think that the model is true?  $p(\vec{s})$  reflects the probability of getting the observed data, summed over all alternative models.  $p(\vec{s} | \mathcal{H})$  is the distribution of possible measurements that one would obtain if the model were true.

I find that the theory is most understandable in terms of odds ratios. Odds ratios are exactly the odds you would use for betting. The reason one bets is because there is some uncertainty in the truth of model  $\mathcal{H}$ . Additional information, such as that provided by searching LIGO data for signals, will refine the betting odds. More precisely, the posterior odds ratio is the product of the prior odds ratio and the Bayes factor, which depends on a measurement. Symbolically, the informed odds of model  $\mathcal{H}_1$  being true to a second model  $\mathcal{H}_0$  being true is

$$\mathcal{O} \equiv \frac{p(\mathcal{H}_1 | \vec{s})}{p(\mathcal{H}_0 | \vec{s})} = \frac{p(\vec{s} | \mathcal{H}_1) p(\mathcal{H}_1)}{p(\vec{s} | \mathcal{H}_0) p(\mathcal{H}_0)}, \quad (4.2)$$

where  $\mathcal{O}$  is the posterior odds and  $p(\mathcal{H}_1)/p(\mathcal{H}_0)$  is the prior odds, before data are taken into account. The fraction  $p(\vec{s} | \mathcal{H}_1)/p(\vec{s} | \mathcal{H}_0)$  is the Bayes factor or marginal likelihood ratio. The right-hand side follows from straightforward application of Bayes' Theorem to the numerator and denominator of the left-hand side.

Applying this to the problem of detection,  $\mathcal{H}_1$  might represent the hypothesis that there exists a signal and  $\mathcal{H}_0$  might be the null hypothesis (no signal). A signal might have a variety of forms. I parameterize the various types of signals with the parameter vector  $\vec{\theta}$ ; then  $\mathcal{H}_1$  represents the hypothesis that any signal at all, integrated (or marginalized) over all possible signal parameters, is present in the

data. Our posterior odds ratio then becomes

$$\mathcal{O} = \frac{p(\vec{s} | \mathcal{H}_1)p(\mathcal{H}_1)}{p(\vec{s} | \mathcal{H}_0)p(\mathcal{H}_0)} \quad (4.3)$$

$$= \frac{\left[ \int p(\vec{s} | \vec{\theta}, \mathcal{H}_1)p(\vec{\theta} | \mathcal{H}_1) d\vec{\theta} \right] p(\mathcal{H}_1)}{p(\vec{s} | \mathcal{H}_0)p(\mathcal{H}_0)} \quad (4.4)$$

$$= \frac{p(\mathcal{H}_1)}{p(\mathcal{H}_0)} \int \frac{p(\vec{s} | \vec{\theta}, \mathcal{H}_1)}{p(\vec{s} | \mathcal{H}_0)} p(\vec{\theta} | \mathcal{H}_1) d\vec{\theta} \quad (4.5)$$

$$\equiv \frac{p(\mathcal{H}_1)}{p(\mathcal{H}_0)} \int \Lambda(\vec{s}, \vec{\theta}) p(\vec{\theta} | \mathcal{H}_1) d\vec{\theta} \quad (4.6)$$

$$\equiv \frac{p(\mathcal{H}_1)}{p(\mathcal{H}_0)} \Lambda(\vec{s}). \quad (4.7)$$

I defined the likelihood ratio  $\Lambda(\vec{s}, \vec{\theta}) = p(\vec{s} | \vec{\theta}, \mathcal{H}_1) / p(\vec{s} | \mathcal{H}_0)$  and the marginal likelihood ratio  $\Lambda(\vec{s}) = \int \Lambda(\vec{s}, \vec{\theta}) p(\vec{\theta} | \mathcal{H}_1) d\vec{\theta}$ . All of the dependence on the data is in these terms.

While  $\Lambda(\vec{s})$  is the correct term for the Bayes factor, if  $p(\vec{s} | \vec{\theta}, \mathcal{H}_1)$  is a sharply peaked function of  $\vec{\theta}$ , the integral can be well approximated by the maximum of  $\Lambda(\vec{s}, \vec{\theta})$  over  $\theta$ . Maximum likelihood techniques save the computational cost of integrating over a potentially large parameter space. Each local maximum of the likelihood identifies a particular set signal parameters  $\vec{\theta}_{\max}$ . The larger the likelihood, the higher the odds that a signal with these parameters is present. Each maximum therefore identifies a candidate signal that can be ranked by the value of the marginal likelihood at  $\vec{\theta}_{\max}$ .

## 4.2 Matched filtering

Let's search Gaussian noise for a particular CBC waveform, i.e., one template. As all of the information in the data is in the marginal likelihood ratio, let us compute that. It consists of a model for the measured data given each hypothesis. The derivation proceeds most simply under the assumption of white noise, and as data can be whitened by a simple, linear transformation, we will generalize the result to non-white data at the end. With this in mind, let us begin by defining a linear signal model,

$$s(t) = h(t) + n(t). \quad (4.8)$$

That is, one's detector readout  $s(t)$  is a linear sum of a true gravitational-wave signal  $h(t)$ , if present, and non-gravitational noise  $n(t)$ . The implementation will make use of discrete-time sampling, where sample  $j$  of the time-series  $x$  with a sampling time of  $\Delta t$  will be denoted

$$x[j] = x(j \Delta t). \quad (4.9)$$

If we observe for some duration  $T$ , there will be  $N = T/\Delta t$  discrete samples of the data. That is,  $\vec{s} = \{s[j] = s(j\Delta t); j = 0 \dots N - 1\}$ .

### 4.2.1 The distribution of data with noise

To compute the likelihood ratio, we need to know the distribution of measured data  $s(t)$  given noise alone and given signal embedded in the noise. We assume

a Gaussian noise distribution. As we further assume white noise, the covariance matrix is proportional to the identity matrix with proportionality factor  $\sigma^2$ . The distribution of noise alone is

$$p_n(\vec{n}) = (2\pi\sigma^2)^{-N/2} \exp\left(-\frac{1}{2\sigma^2} \sum_{j=0}^{N-1} n^2[j]\right). \quad (4.10)$$

We will want to use frequency-domain techniques because they have less computational cost than time-domain techniques. The notation is simplest by passing through the continuous-time domain and expressing our final results in the continuous-frequency domain. If we can multiply by the sampling time  $\Delta t$  and shrink it while holding the total measurement duration  $T = N\Delta t$  constant, we can identify the Riemann integral,

$$\lim_{\substack{\Delta t \rightarrow 0 \\ N\Delta t = \text{const}}} \sum_{j=0}^{N-1} n^2[j] \Delta t = \int_0^T n^2(t) dt. \quad (4.11)$$

If our integration time is sufficiently long, we can approximate this in the frequency domain with Parseval's theorem,

$$\int_{-\infty}^{\infty} n^2(t) dt = \int_{-\infty}^{\infty} |\tilde{n}(f)|^2 df. \quad (4.12)$$

On the road to the continuous-frequency domain, we introduced a factor of the sampling time  $\Delta t$ . We can usefully relate it to the power-spectral density  $S_n(|f|)$  of

the noise  $n(t)$  by:

$$R_n(\tau) = \langle n(t)n(t+\tau) \rangle_t \quad (4.13)$$

$$\begin{aligned} S_n(f) &= 2 \int_0^\infty R_n(\tau) d\tau \\ &\approx 2 \sum_{k=0}^{N-1} R_n[k] \Delta\tau \\ &= 2\sigma^2 \Delta t, \end{aligned} \quad (4.14)$$

where  $R_n(\tau)$  is the autocorrelation function of  $n(t)$  and  $\langle \cdot \rangle_t$  refers to an average over  $t$ . As white noise is wide-sense stationary, we rendered the autocorrelation as an even function of just  $\tau$ , the time-delay. In addition, we used the equality of  $\Delta\tau$  and  $\Delta t$  and that the autocorrelation function of a discrete, white process is  $R_n[k] = \sigma^2 \delta_{k0}$ . Note that  $S_n(f)$  is a constant for white noise.

Putting everything together, we see that

$$p_n(\vec{n}) = (2\pi\sigma^2)^{-N/2} \exp\left(-\frac{1}{2} 2 \int_{-\infty}^{\infty} \frac{|\tilde{n}(f)|^2}{S_n(|f|)} df\right) \quad (4.15)$$

$$= (2\pi\sigma^2)^{-N/2} \exp\left(-\frac{1}{2} 4 \int_0^{\infty} \frac{|\tilde{n}(f)|^2}{S_n(f)} df\right), \quad (4.16)$$

where in the final equality, we used the reality of  $n(t)$ , which implies that  $|\tilde{n}(f)|^2 = |\tilde{n}(-f)|^2$ , to substitute the one-sided power-spectral density. Finally, we expect that our signals of interest will be weak compared to noise, so we use  $S_n(f) = S_s(f)$  in practice.

In fact, though we inserted the power-spectral density into the denominator rather naïvely, it holds in the case of non-white input. Let us create colored noise out of white noise through some colored, linear process  $\tilde{x}(f) = K(f)\tilde{w}(f)$ . We then

get:

$$p_n(\vec{n}) = (2\pi)^{-N/2} |\Sigma|^{-1/2} \exp \left( -\frac{1}{2} \sum_{j=0}^{N-1} \sum_{k=0}^{N-1} n[j] \Sigma_{jk}^{-1} n[k] \right) \quad (4.17)$$

$$= (2\pi)^{-N/2} |\Sigma|^{-1/2} \exp \left( -\frac{1}{2} 4 \int_0^\infty \frac{|\tilde{x}(f)|^2}{K^{-2}(f) S_w(f)} df \right), \quad (4.18)$$

and it turns out that  $S_x(f) = |1/K(f)|^2 S_w(f)$ .  $\Sigma$  is the covariance matrix between elements of  $\vec{x}$  and  $|\Sigma|$  is its determinant. Equation (4.18) is correct for all Gaussian noise, white or colored.

Finally, for notational convenience, let us define the operator  $(\cdot, \cdot)$  as

$$(a, b) = 4\Re \int_0^\infty \frac{\tilde{a}(f) \tilde{b}^*(f)}{S_n(f)} df, \quad (4.19)$$

where  $\Re$  indicates the real part of the integral. This leads us to our final form of the noise distribution in the case of no signal ( $s = n$ ),

$$p(\vec{s} | \mathcal{H}_0) = p_n(\vec{s}) = (2\pi\sigma^2)^{-N/2} \exp \left[ -\frac{1}{2} (s, s) \right]. \quad (4.20)$$

#### 4.2.2 The distribution of data with signal and noise

When considering the expectation value over  $s(t)$ , recall that  $h(t)$  is a deterministic process (pre-determined time-series), so expectation values apply only to  $n(t)$ , a stochastic noise process. Our linear signal model, Eq. (4.8), and the linearity of our filtering operator, Eq. (4.19), makes it easy to generalize the noise distribution to signal. Thus, we can use  $n = s - h$  to immediately arrive at the distribution of data given signal and noise.

$$p(\vec{s} | \mathcal{H}_1) = p_n(\vec{s} - \vec{h}) = (2\pi\sigma^2)^{-N/2} \exp \left[ -\frac{1}{2} (s - h, s - h) \right]. \quad (4.21)$$

### 4.2.3 Matched filter signal-to-noise ratio

We can now write down the likelihood ratio in Eq. (4.7) as

$$\Lambda(\vec{s}) = \frac{(2\pi\sigma^2)^{-N/2} \exp \left[ -\frac{1}{2}(s-h, s-h) \right]}{(2\pi\sigma^2)^{-N/2} \exp \left[ -\frac{1}{2}(s, s) \right]} \quad (4.22)$$

$$= \exp \left( (s, h) - \frac{1}{2}(h, h) \right). \quad (4.23)$$

As  $h(t)$  is deterministic,  $(h, h)$  is a constant scalar. The likelihood is monotonic with  $(s, h)$ , so  $(s, h)$  can be used as a proxy statistic for detection. As  $h$  will have parameters  $\vec{\theta}$ , we should marginalize over them, but in practice, a maximum likelihood approach is employed, yielding discrete events at the maxima  $\vec{\theta}_{\max} = \operatorname{argmax}_{\vec{\theta}}(s, h(\vec{\theta}))$ . These events are called triggers.

While we can substitute gravitational waveforms for CBCs at this point to derive the ultimate signal-to-noise ratio (SNR) used in LIGO-Virgo CBC searches, it is derived fully elsewhere [56]. The key element to take from this section is the likelihood ratio approach, which we will use again in Sec. 4.3 to compensate for non-stationary, non-Gaussian noise.

## 4.3 Post-matched-filtering likelihood ratios

So far, we have only the matched filtering part of the search. Much more goes into the workflow that takes raw data to a final list of gravitational-wave candidates. Chapter 6 contains the details of this process, which involves constructing a collection of template waveforms against which to filter, matched filtering, waveform

consistency tests, and inter-detector trigger consistency tests (coincidence). We also assign an improved ranking statistic  $\rho_{\text{eff}}$ , the effective SNR, based on waveform consistency and matched filter SNR.

At the end of this process, one holds a list of candidates. One generally assigns significance to candidates by reporting the false-alarm probability, that is, the probability that noise alone would produce a louder candidate. The interpretation of this is slightly clouded when one considers the properties of the template bank used in the search. The false-alarm probability is widely disparate for templates of different chirp mass in the presence of non-Gaussianity. High chirp-mass signals are shorter in duration and span less time-frequency volume than low chirp-mass signals, looking more like a generic “glitch”, a short-duration, non-Gaussian noise transient in the data. Glitches are the subject of considerable investigation [68], as they plague all instruments and significantly degrade the performance of transient searches. High-mass signals spanning less time-frequency volume means that the waveform consistency tests have less discriminating power, so a greater fraction of glitches will pass through the pipeline. In short, a simple false-alarm probability based on  $\rho$  or  $\rho_{\text{eff}}$  is suboptimal.

In fact, matters become worse when one considers that candidates can have passed coincidence and waveform consistency in some subset of the available detectors. As H1 and L1 are significantly more sensitive than H2 or V1, one would intuitively consider an H1–L1 candidate as far more significant than an H2–L1 candidate, all else being equal. This is not reflected in a simple  $\rho$  or  $\rho_{\text{eff}}$  ranking.

The element we seek is an efficiency weighting, a factor that favors the regions of recovered-parameter space that are more sensitive to the signals of interest.

In Sec. 4.3.1 I apply the likelihood ratio language in the context of a CBC search after matched filtering has been performed. I also step through algorithms for estimating the likelihood ratio for triggers. Section 4.3.2 presents some real-world difficulties in implementation and the trade-offs made in the search for gravitational waves in association with GRBs.

### 4.3.1 Constructing a likelihood ratio

Our likelihood ratio is defined in Eq. (4.7), but let's write it specialized for our post-matched-filtering, non-Gaussian-data circumstance, without any assumptions as to the nature of the data, as

$$\Lambda(\vec{c}) = \frac{p(\vec{c} | \mathcal{H}_1)}{p(\vec{c} | \mathcal{H}_0)} \quad (4.24)$$

$$\vec{c} = \{\rho_{\text{eff}}, t_c, \vec{\theta}_{\text{template}}\}. \quad (4.25)$$

$\vec{c}$  here is a collection of data about a candidate. It takes the role of  $\vec{s}$  earlier. The numerator can be interpreted as a detection efficiency. It is the probability of getting a candidate like the one we got if there is a signal. Where we are more sensitive, the probability increases. The denominator can be interpreted as the false-alarm probability. It is the probability of getting a candidate like the one we got if there is no signal. Here is where we incorporate varying background rates.

Associating a trigger with a hypothesis requires additional specification on

our part. What population of triggers are we characterizing? Do we mean the distribution of all candidates that come out of the pipeline or do we mean that we will choose the single loudest candidate from each of a finite number of trials? For an externally triggered search where we have a naturally defined foreground and background, we will take the latter approach; the trials are fully defined in Sec. 6.1. For the untriggered CBC searches, the background duration is not a convenient multiple of the foreground duration, so a trial is harder to delineate. There, each candidate is assigned a likelihood ratio separately.

What we haven't specified is the model parameters,  $\vec{\theta}$ . A CBC signal can be completely characterized by several parameters: coalescence time, two mass parameters, six spin parameters, initial orbital inclination relative to our line of sight, sky location, polarization angle, phase, distance, and a other orbital parameters. Short of full numerical relativity calculations, which can take weeks to months for a single waveform, all current waveform-generation routines that are interfaced to LIGO/Virgo data analysis pipelines ignore eccentricity, spin-induced orbital precession, and deviations from the point-particle limit. We must marginalize over all model parameters with our priors as

$$\Lambda(\vec{c}) = \frac{\int p(\vec{c} | \vec{\theta}, \mathcal{H}_1) p(\vec{\theta} | \mathcal{H}_1) d\vec{\theta}}{p(\vec{c} | \mathcal{H}_0)}. \quad (4.26)$$

Measuring the false-alarm probability that appears in the denominator of Eq. (4.26) is straightforward. Looping over each background trial:

1. Employ the pipeline to generate candidates for this trial.

2. If this yields any candidates that are in the neighborhood (not yet defined) of  $\vec{c}$ , add 1 to the count.

At the end, normalize by the total number of iterations.

We carry out the integration in Eq. (4.26) by simple Monte–Carlo integration. In this process, we perform the following loop:

1. Choose a waveform, where each parameter is drawn randomly from its prior.
2. The signal is added to a trial that was previously used for background estimation.
3. Employ the pipeline to generate candidates for this segment of data.
4. If this yields any candidates that are in the neighborhood (not yet defined) of  $\vec{c}$ , add 1 to the count.

At the end, normalize by the total number of iterations.

The likelihood ratio incorporates more information about the candidate than  $\rho_{\text{eff}}$ . It flows naturally from a Bayesian framework and is provably the best one can do given the information described by the candidates. All deficiencies are in the vagaries of implementation.

### 4.3.2 The warts of actual implementation

Implementation is never as clean as the theoretical design. In implementing the likelihood-ratio ranking for the S5/VSR1 search for CBCs associated with short

GRBs, we made compromises, all of which contain room for future improvement.

### Parameter choice

Although the road is open for throwing all candidate parameters into our bag, we consider the most important subset,  $\vec{c} = (\rho_{\text{eff}}, \overline{\mathcal{M}}, C)$ .  $\rho_{\text{eff}}$  here is the combined effective SNR, which is the quadrature sum of the single-detector effective SNRs.  $\overline{\mathcal{M}}$  is the mean chirp mass of the templates of the single-detector triggers.  $C$  is the set of detectors that provided coincident triggers to the candidate;  $C$  is a mnemonic for detector Combination. In its full generality,  $C$  requires specification both of the detectors that provided coincident triggers and the detectors that were accepting triggers at the time; it means something quite different for an H2-L1 candidate if H1 was available and did not see anything or if H1 was not available and could not see anything.

### CDF instead of PDF

Although the likelihood ratios use probability distribution functions (PDFs), we chose to use one minus the cumulative distribution function (CDF) in  $\rho_{\text{eff}}$ . The choice reflects a prejudice that the likelihood ratio should increase monotonically with  $\rho_{\text{eff}}$ , at least within a given  $(\overline{\mathcal{M}}, C)$  bin. Use of the CDF is not rigorously justified, but for the loud tails of the distribution, the correspondence should be good. With the small number of bins, probability estimation is weak. Rather than calculate the right thing poorly, we calculate something not quite right well.

## Binning

Estimating a distribution from a finite number of measurements inevitably requires binning and/or fitting. Binning provides well-defined boxes in which one can take simple fractions for PDF/CDF estimation, but it splits the finite number of trials over them, increasing one's counting uncertainty. In our case, we binned over  $(\overline{\mathcal{M}}, C)$ .

## Linear vs cubic distance prior

The exceptional model parameter is the distance  $D$ . In our Monte–Carlo integration, we draw distance from a prior uniform in  $D$  rather than a more realistic  $D^3$  so that we can assess efficiency both near and far without significant discretization errors. A  $D^3$  reweighting during the tally can correct for this, but it was deemed unnecessary due to using a CDF instead of a PDF for  $\rho_{\text{eff}}$ . That is,  $D$  should dominantly affect  $\rho_{\text{eff}}$ , rather than other parameters in our likelihood ratio, and we're already doing the wrong thing by using a CDF rather than a PDF, so a correction seemed superfluous.

## Background tail extrapolation

With a finite number of trials from which to determine the background distribution and a signal population that extends to nearby  $D$ , it is inevitable that some signals will be louder in  $\rho_{\text{eff}}$  than all background trials. To avoid division by zero in taking the likelihood ratio, one must extrapolate. As the point of the post-matched-filtering

likelihood is to overcome non-Gaussianity, uneven background, and uneven sensitivity, we have no analytical model to use. In our implementation, we used an ansatz that

$$p(\rho_{\text{eff}} \geq \rho_{\text{eff}}^*, \overline{\mathcal{M}}, C | \mathcal{H}_0) = \begin{cases} p_{\text{naive}}(\rho_{\text{eff}} \geq \rho_{\text{eff}}^*, \overline{\mathcal{M}}, C | \mathcal{H}_0) & \text{for } \rho_{\text{eff}}^* < \rho_{\text{eff}}^{\text{extrap}} \\ \mathcal{K}(\overline{\mathcal{M}}, C) \exp(-\rho_{\text{eff}}^\alpha) & \text{for } \rho_{\text{eff}}^* \geq \rho_{\text{eff}}^{\text{extrap}} \end{cases} \quad (4.27)$$

for fitted spectral parameter  $\alpha$ , the fitted extrapolation point  $\rho_{\text{eff}}^{\text{extrap}}$ , and the normalization factor  $\mathcal{K}(\overline{\mathcal{M}}, C)$ , which is determined from continuity. For Gaussian noise and  $\rho_{\text{eff}} \rightarrow \rho$ , we would set  $\alpha = 2$ , but we tune the values based on the noise properties of S5/VSR1.

### **Trials without candidates**

The volume of data demands that we set thresholds in  $\rho$ ,  $\chi^2$ , and  $r^2$  and apply clustering to reduce the rate of triggers, preferentially omitting candidates that are unlikely to be real signals. These efforts pay great dividends. However, this truncation means that not all trials will yield candidates. Trials without candidates have formally undefined  $\rho$ , so have undefined likelihood ratios. In the implementation of the likelihood ratio techniques of this chapter, trials without candidates are given maximum likelihood ratios of 0. Our probability distributions are thus made discontinuous.

# Chapter 5

## Statistical interpretations

With a ranking statistic in hand from Chap. 4, we must determine if our on-source candidates are indeed gravitational-wave detections; the techniques we use are described in Sec. 5.1. We can also constrain the space of possible signals based on what we observed using a Feldman–Cousins approach [69], as described in Sec. 5.2. Finally, with many null results, we can make another attempt at detection—the detection of a population of events that are individually sub-threshold—with the Wilcoxon–Mann–Whitney  $U$ -test, which is discussed in Sec. 5.3.

### 5.1 Detection criteria

#### 5.1.1 Determining the threshold for a single GRB

We would like our results rendered amenable to simple, human interpretation, arranged so that we can set the threshold according to sociologically required

criteria for claiming a detection, e.g., “We require a one-in-a-million false-alarm probability to accept the detection of such a hotly contested object with a history of false alarms.”<sup>1</sup> With a proper likelihood ratio, one can compare likelihood ratios of candidates and set the detection threshold based on the posterior odds ratio. However, the various implementation details described in Sec. 4.3.2 alter the distribution of likelihood ratios relative to the theoretical distribution. Instead of comparing our on-source observation to a theoretical distribution, we can compare it to a measured distribution from the off-source trials.

To that end: for each off-source trial, we find the likelihood ratio of the loudest candidate. Then the false-alarm probability (F.A.P.) is the fraction of background (off-source) trials that yield a likelihood ratio greater than the on-source likelihood ratio. That is,

$$\text{F.A.P.} = p(\Lambda > \Lambda_{\text{obs}} | 0). \quad (5.1)$$

This is the final quantity we report for each GRB.

## 5.2 Constraining parameter space

In adjusting our beliefs of the universe based on our observations, one should employ the well developed Bayesian framework defined in Chap. 4. However, for the S5/VSR1 search we instead used frequentist techniques, constructing our

---

<sup>1</sup>Here, I refer to repeated claims of gravitational-wave detection by Joseph Weber throughout the 1960s, 70s, and 80s [70].

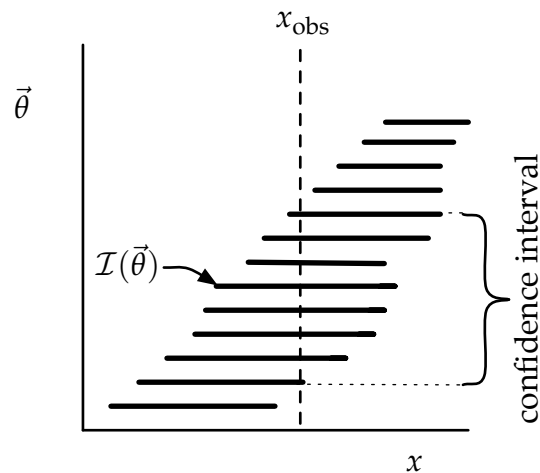


Figure 9 : Sketch of a frequentist confidence belt construction. Each horizontal line is a confidence belt  $\mathcal{I}(\vec{\theta})$  at some confidence level. The vertical dashed line is the observed significance  $x_{\text{obs}}$ . The intersection of the observation with the confidence belts is the confidence interval.

confidence belts in the manner dictated by Feldman and Cousins [69]. This was done because the formalism for correctly constructing a prior distribution on signal strength for each GRB was very rudimentary, and the Bayesian results depend sensitively on how this prior distribution is constructed. I give a walk-through of the frequentist implementation in Sec. 7.5; here I describe the formalism in general terms.

Frequentist techniques for determining what range of physical parameters are compatible with an observation involve constructing confidence belts. We say that the intervals  $\mathcal{I}(\vec{\theta}) = \{x | \vec{\theta}\}$  in detection statistic  $x$  for signals of parameters  $\vec{\theta}$  form a confidence belt at confidence level  $\mathcal{C}$  if

$$\int_{\mathcal{I}(\vec{\theta})} p(x | \vec{\theta}) dx = \mathcal{C}. \quad (5.2)$$

When we make our observation, we obtain our detection statistic  $x_{\text{obs}}$ . Our confidence interval is the region of  $\vec{\theta}$  in which  $x_{\text{obs}} \in \mathcal{I}(\vec{\theta})$ . The interpretation is that the true parameters  $\vec{\theta}_{\text{true}}$  lie in the interval  $100 \times \mathcal{C}\%$  of the time. We can also say that we exclude everything outside of this region with  $\mathcal{C}$  confidence. See Fig. 9 for a sketch of these definitions.

The definition of a confidence belt in Eq. (5.2) leaves considerable ambiguity. For a continuous probability distribution, there may be infinitely many intervals that satisfy the definition. For a complete prescription, we must provide a well-defined means for choosing which  $x$  go into  $\mathcal{I}(\vec{\theta})$ . One intuitive approach is that of Crow and Gardner [71], in which we choose the set of points with the constraint that the extent of the acceptance region,  $|\mathcal{I}(\vec{\theta})|$ , is minimized and in the event that there are ties, we take the pair with the smallest value of upper bound that satisfies this constraint. Put another way,  $\mathcal{I}(\vec{\theta})$  is the locus of  $\{x : p(x | \vec{\theta}) > p^*\}$ , where we gradually lower  $p^*$  until  $\mathcal{I}(\vec{\theta})$  satisfies the criterion of Eq. (5.2). Another obvious approach is to decide that you only want an upper limit, setting the lower end of the interval at  $-\infty$  or the lower edge of a compact domain. This has its problems in that you can construct intervals of zero measure or if you have a detection, then you may have lost interest in an upper limit and would rather constrain the parameters of your detection. It's important to note that "flip-flopping", deciding whether or not to set an upper limit based on what you observe, is incorrect and invalidates the statement that the true parameters lie in the interval  $100 \times \mathcal{C}\%$  of the time.

Feldman and Cousins present a different ordering scheme [69], in which we add

points to our interval ranked by the quantity

$$R(x | \vec{\theta}) = \frac{p(x | \vec{\theta})}{p(x | \vec{\theta}_{\text{best}})}. \quad (5.3)$$

Here,  $p(x | \vec{\theta}_{\text{best}})$  is the probability density of obtaining  $x$  using the the best-fitting, physically allowed  $\vec{\theta}$ .  $\mathcal{I}(\vec{\theta})$  is the locus of  $\{x : R(x | \vec{\theta}) > R^*\}$ , where we gradually decrease  $R^*$  until  $\mathcal{I}(\vec{\theta})$  satisfies the criterion of Eq. (5.2). That is, one continues adding  $x$  values to  $\mathcal{I}(\vec{\theta})$  in order of decreasing  $R(x | \vec{\theta})$  until the probability  $\mathcal{C}$  is covered.

The Feldman–Cousins (FC) method focuses on the most physically interesting region of  $\vec{\theta}$  space by construction, as  $R(x | \vec{\theta}) = 1$  at the best-fit values of  $\vec{\theta}$  and  $R(x | \vec{\theta}) < 1$  everywhere else. Thus, the best-fit value is always in  $\mathcal{I}(\vec{\theta})$  and always within the final confidence intervals. The FC method solves the problems of the pure upper-limit approach, namely that one generally wishes to provide two-sided bounds on detections and upper limits on non-detections. FC can smoothly transition from upper limit to double-sided constraint with varying  $x$ . Zero-measure belts from discontinuities are only problematic if they are in the physically interesting region, which would cause problems for any method of physical interpretation.

### 5.2.1 Exclusions and likelihood ratios for sub-populations

In Sec. 4.3.1, we learned how to concretely construct a likelihood ratio for a given signal population. In the detection search, we choose to include a wide range of masses, as we are interested in the existence of any signal. In making distance

exclusions, we wish to make a more fine-grained astrophysical statement as a function of the NS's companion's mass, so we break up the companion mass  $m_{\text{comp}}$  into multiple bins, forming the likelihood ratio for each and making separate exclusions for each. In the remainder of this section, we will use  $\Lambda(m_{\text{comp}})$  to represent the likelihood ratio of the loudest candidate in a trial being caused by a signal from the mass bin of  $m_{\text{comp}}$ . The procedure to form this likelihood ratio is identical to that of the whole search, but uses only a subset of the injected signals. Equation (5.3) is thus given by

$$R(\Lambda(m_{\text{comp}}) | D) = \frac{p(\Lambda(m_{\text{comp}}) | D)}{p(\Lambda(m_{\text{comp}}) | D_{\text{best}})} \quad (5.4)$$

for each  $m_{\text{comp}}$  bin.

### 5.2.2 Handling multi-modal distributions

If  $R(x | \vec{\theta})$  is multi-modal in  $x$ , then applying the FC construction naively will yield broken  $\mathcal{I}(\vec{\theta})$ , i.e.,  $\mathcal{I}(\vec{\theta})$  have an  $x$  gap for fixed  $\vec{\theta}$ . This is theoretically perfectly valid. However, in our implementation wherein we are bounding regions of  $D$  space, we chose to enforce our a priori belief that  $\Lambda(m_{\text{comp}})$  will be distributed with a single mode for fixed  $D$  and that any apparent extra modes are due to statistical fluctuations in our measurement of  $R(\Lambda(m_{\text{comp}}) | D)$ . To this end, we add  $x$  values to  $\mathcal{I}(\vec{\theta})$  according to the  $R(x | \vec{\theta})$  ranking, but fill in any gaps that form by having  $\mathcal{I}(\vec{\theta})$  extend from the minimum to the maximum of  $\{x : R(x | \vec{\theta}) > R^*\}$ , gradually decreasing  $R^*$  until  $\mathcal{I}(\vec{\theta})$  satisfies the criterion of Eq. (5.2). Belts are thereby forced

to be simply connected.

The FC paper explicitly addresses gaps in the confidence interval for a measurement  $x_{\text{obs}}$ , i.e., when the intersected belts are not contiguous. In this case, the minimum and maximum  $\vec{\theta}$  are taken to form the reported confidence interval. The physical measurement is thus always simply connected.

### 5.2.3 Handling empty trials

The fact that we set thresholds in our analysis pipeline introduces discreteness into our distributions, as described in Sec. 4.3.2. The distribution  $p(\Lambda(m_{\text{comp}}) | D)$  will have a gap in it at low values of  $\Lambda(m_{\text{comp}})$  where no trial produced a detectable event, then there will be a pile-up of trials at  $\Lambda(m_{\text{comp}}) = 0$ , the value we assign to trials with no candidates. The distribution is discontinuous. In the sparsely populated region between  $\Lambda(m_{\text{comp}}) = 0$  and the bulk, our estimation of the ranking  $R(\Lambda(m_{\text{comp}}) | D)$  is poor or nonexistent. To this end, we artificially truncate the lower end of the  $\Lambda(m_{\text{comp}})$  distribution such that the  $\Lambda(m_{\text{comp}}) = 0$  bin sweeps up candidates up to a truncation point,  $\Lambda_{\text{thresh}}$ . In this way, we smooth  $R(\Lambda(m_{\text{comp}}) | D)$  to suppress artifacts at the low  $\Lambda(m_{\text{comp}})$  end. As  $\Lambda_{\text{thresh}}$  exists to prevent a low  $\Lambda(m_{\text{comp}})$  gap, we set it by eye to the value below which threshold effects were apparent at high distances (the noise limit).

### 5.2.4 Handling counting uncertainty

When we count trials to determine the probability  $\int_{\mathcal{I}}(\vec{\theta})p(\Lambda(m_{\text{comp}}) | D) d\Lambda(m_{\text{comp}})$ , we are making a measurement with some uncertainty. With  $N$  Monte–Carlo simulations in a given  $(m_{\text{comp}}, D)$  bin, trying to accumulate up to a true probability of  $\mathcal{C}$ , standard deviation of the measured value  $\hat{\mathcal{C}} = M/N$  is

$$\delta_{\text{MC}} = \sqrt{\frac{\mathcal{C}(1 - \mathcal{C})}{N}}. \quad (5.5)$$

That is, to guarantee coverage of probability  $\mathcal{C}$  in 90% of measurements assuming that the central limit theorem holds, we should continue adding to  $\mathcal{I}(\vec{\theta})$  until we cover  $\mathcal{C} + 1.28 \times \delta_{\text{MC}}$ , where 1.28 standard deviations above the mean is the point at which we accumulate 90% cumulative probability on a Gaussian distribution.

Note that this procedure sets a scale for the number of simulations  $N_{\text{useful}}$  per bin to make a useful measurement, as

$$\frac{1}{N_{\text{useful}}} \leq 1 - (\mathcal{C} + 1.28 \times \delta_{\text{MC}}). \quad (5.6)$$

For  $\mathcal{C} = 90\%$ , this sets the minimum number to 32. For fewer simulations, the belt will cover the entire  $\vec{\theta}$  space spanned by the simulations, which gives no robustness to outliers and has a large measurement uncertainty.

## 5.3 Population statement

If we have no detections in a search for a number of GRBs  $N_{\text{GRB}}$ , we can still imagine that there is a population of real signals in our data set that are individually

sub-threshold for detection claims, but collectively stand out in some way. There are several tests that might apply here, but we chose the Wilcoxon–Mann–Whitney  $U$  test [72]. The  $U$  test answers the question “Is population A drawn from the same parent distribution as population B?” The  $U$  test is non-parametric, that is, it doesn’t require a model for the parent distribution, and it is exceedingly simple to implement. It works on rank alone, so ignores the magnitude of difference between adjacently ranked trials.

Let population A refer to a set of likelihood ratios  $\mathcal{L}_A$  containing  $N_A$  elements and population B refer to a set of likelihood ratios  $\mathcal{L}_B$  containing  $N_B$  elements. Then:

1. Combine the two sets to form  $\mathcal{L}$  and sort them in descending order. Number the elements of  $\mathcal{L}$  by their new orders, starting with 1; each number is a statistic’s rank, comprising  $\mathcal{R}_A$  for elements of A and  $\mathcal{R}_B$  for elements of B, where the  $i^{\text{th}}$  element corresponds to the  $i^{\text{th}}$  position in  $\mathcal{L}$ . Ties should be resolved assigning each identical likelihood ratio a rank equal to the average of the contested ranks to keep the sum invariant. E.g., if two likelihood ratios are tied for second and third place, they should each be given a rank of 2.5.

2. Let

$$R_A = \sum_{i=1}^{N_A} \mathcal{R}_{A,i} \quad (5.7)$$

$$R_B = \sum_{i=1}^{N_B} \mathcal{R}_{B,i}. \quad (5.8)$$

Note that  $R_A + R_B = (N_A + N_B)(N_A + N_B + 1)/2$ , as this is a sum of all

integers from 1 to  $N_A + N_B$ .

3. The  $U$  statistic between population A and population B is given by

$$U_A = R_A - \frac{N_A(N_A + 1)}{2} \quad (5.9)$$

$$U_B = R_B - \frac{N_B(N_B + 1)}{2}. \quad (5.10)$$

Note that with some algebra, we find that

$$U_A = N_A N_B - U_B. \quad (5.11)$$

To characterize population A as being statistically greater than population B, we would look for large  $U_B$  and vice versa. From now on, we will use  $U = U_B$  as our statistic. Now we have  $U$  statistic, but need a means to interpret it. As the  $U$  statistic is formed from the sum of a stochastic process, we can invoke the Central Limit Theorem and make the usual probabilistic interpretations associated with Gaussianity. The mean and standard deviation of the distribution of  $U$  under the null hypothesis that populations A and B are indeed drawn from the same parent distribution are

$$\mu_U = \frac{N_A N_B}{2} \quad (5.12)$$

$$\sigma_U^2 = \frac{N_A N_B (N + 1)}{12}. \quad (5.13)$$

In the case that we only are searching for GRB on-source likelihood ratios being stochastically larger than off-source likelihood ratios, we would use a one-tailed probability, where  $P(U > \mu_U) = 0.5$ ,  $P(U > \mu_U + \sigma_U) = 0.16$ ,  $P(U > \mu_U + 2\sigma_U) = 0.023$ , and  $P(U > \mu_U + 3\sigma_U) = 0.001$ .

## Chapter 6

# A pipeline for externally triggered CBC searches

With matched filtering, coincidence, candidate ranking, and interpretation elements in hand from the efforts of Chapters 4 and 5, we must connect these elements together. A data analysis pipeline is a connected set of components that perform various transformations on the data, such as cataloguing it, moving the data to computing resources, parcelling it into chunks that are digestible, analyzing it to produce triggers, and performing post-analysis operations on triggers to produce a scientific result. The CBC externally triggered pipeline is built out of the same pipeline used for the other, untriggered CBC analyses with a few additions, as we shall see. We will walk through most aspects of trigger production and post-processing in Chap. 7, using GRB 070201 as a case study.

## 6.1 Experimental setup

The binary coalescence model of short GRB formation predicts that the time delay between the arrival of a gravitational wave and the arrival of the subsequent electromagnetic burst is a few seconds. The arrival time of the electromagnetic component is called the trigger time and it is provided by gamma-ray detectors in orbit or in the interplanetary network, as described in Sec. 2.1. We search for gravitational-wave signals within an *on-source segment* of  $[-5, +1)$  s around each trigger time for each GRB of interest, feeling that this window captures the physical model with some tolerance for its uncertainties. We assessed uncertainties in reported trigger times and quantization in our own analysis along integer second boundaries, finding that these each contribute less than 1 s. For example, when the Swift BAT instrument determines that the count rate has risen above a threshold, it waits for the maximum to pass, checking with a 320 ms cadence (N. Gehrels & D. Palmer 2008, private communication); it reports the start time of the block containing the maximum, rather than making any attempt to identify the start of the burst, and does so with a 320 ms granularity. As another example, there have been reports of sub-threshold precursors to many GRBs [73]. For each GRB in our sample, we checked tens of seconds of light curve by eye to look for both excessive difference between the trigger time and the apparent rise time, and also for precursors, but found nothing to suggest that we should correct the published trigger times. The largest timing uncertainty we identified is the delay between the

compact merger and the prompt emission of the internal shocks.

Because we believe that a gravitational wave associated with a GRB only occurs in the on-source segment, we use *off-source trials*, up to 324 6 s-long times that do not intersect the on-source segment, to estimate the distribution of background due to the accidental coincidences of noise triggers. We also re-analyze the off-source trials with simulated signals added to the data to test the response of our search to signals; these we call *injection trials*. The actual number of off-source trials included in the analysis varied by GRB, as the trials that overlapped with data-quality vetoes were discarded [74]. To prevent biasing our background estimation due to a potential loud signal in the on-source trial, the off-source segments do not use data within 48 s of the on-source segment, reflecting the longest duration of templates in our bank; these are the *buffer segments*. Finally, we discard 72 s of data subject to filter transients on both ends of the off-source region. Taking all of these requirements into account, the minimum analyzable time is 2190 s. We require that all of this time be flagged as contiguous *science mode*. Science mode is our designation for the detector operating in its nominal configuration. We require contiguous science mode, as the character of the background can change between science mode stretches. (See the schematic representation in Fig. 10.)

Though the details of candidate generation will be described in Sec. 6.4, we should note here that we require that candidates be found with compatible parameters in multiple detectors for the massive background reduction that coincidence

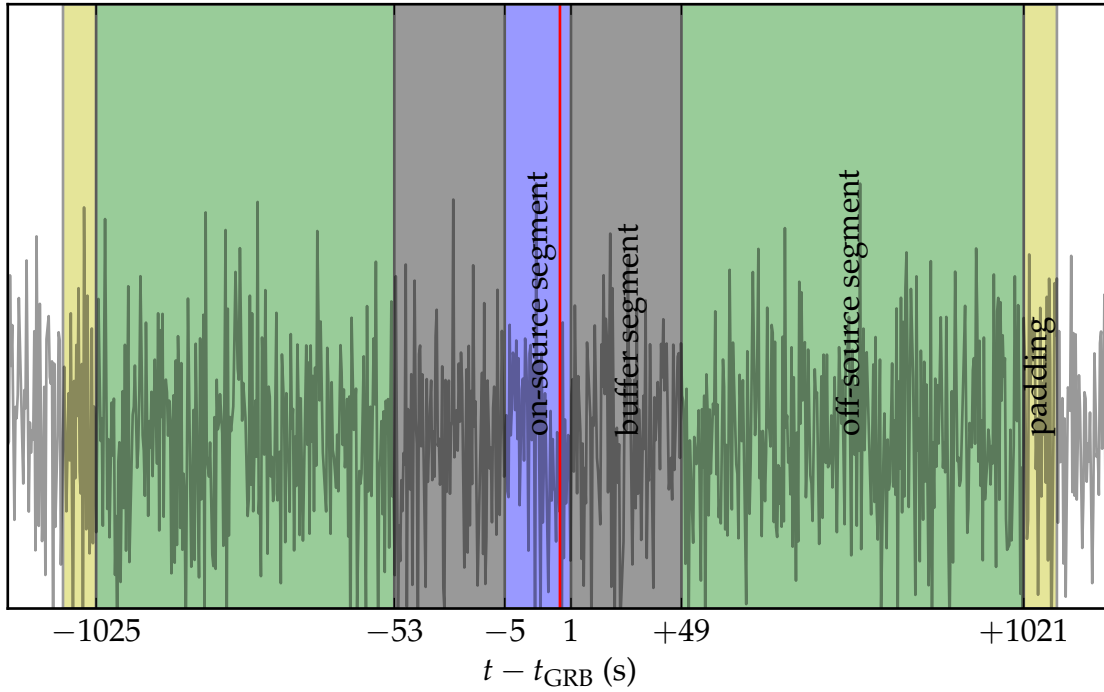


Figure 10 : Experimental setup: segmentation. A schematic representation of how we divided the data near a short GRB into on-source, buffer, off-source, and padding segments.

brings (see Sec. 6.6). As the detectors are not always online and producing science-mode data, it is sometimes impossible to find 2190 s of multiply coincident time arranged symmetrically about the on-source segment. Our implementation of the segmentation described above does not demand symmetry and will choose the minimally asymmetric arrangement of 6 s trials. This means that the actual arrangement of segments may vary from what is shown in Fig. 10.

## 6.2 Data quality

Some periods are found to have data of degraded quality due to instrumental and environmental disturbances such as photodiode saturation, analog to digital converter saturation, uncontrolled laser light from H1 spraying into H2 or vice versa, calibration signals missing, etc. Most of these problems are discovered in real time as the data are taken, but some are noted after the fact. A database holds the data quality segments, which we can query for our periods of interest. Although many conditions are marked with data quality flags, we take only a subset that are known to indicate physically meaningless measurements. We mark each trial that overlaps such a data quality flag and omit them from the analysis entirely.

## 6.3 The role of H1-H2 in triggered and untriggered CBC searches

There is a noteworthy difference with respect to untriggered inspiral searches. For background estimation, untriggered searches use coincidences found between triggers from different detectors, to which they apply unphysical time-shifts greater than the light-travel time between detector sites. Unfortunately, H1 and H2, being co-located, share a common environmental noise that is absent from the time-shift background measurement. Being unable to estimate the significance of H1-H2 candidates reliably, the untriggered search examines them with significantly greater reservation and does not consider them at all in upper-limit statements on rates.

The present search performs its background estimation with unshifted coincidences under the assumption that any gravitational-wave signal will appear only in the on-source trial. Thus, we regain the unconditional use of H1–H2 candidates.

#### **6.4 The untriggered S5/VSR1 low-mass candidate-generation pipeline**

The S5/VSR1 untriggered low-mass search pipeline uses matched filtering over a bank of waveform templates to determine single-instrument triggers. These triggers then go through a multi-detector coincidence test. After coincidence, the pipeline executes the matched-filtering-coincidence cycle again, hierarchically. The second stage adds computationally expensive signal-based vetoes. Besides the same workflow and code, most of the analysis parameters of the externally triggered search have been tuned to identical or nearby values as the S5/VSR1 low-mass untriggered search. The implementation of this pipeline that we use described in Duncan Brown’s 2004 University of Wisconsin–Milwaukee thesis [56] and in Collaboration papers [75]. Although they are major pieces of infrastructure, we omit discussion of data-taking, data-discovery, data-quality queries, and data-conditioning.

The core of the inspiral search involves correlating the measured data against the theoretical waveforms expected from compact binary coalescence, a technique called matched filtering (see Sec. 4.2 for a derivation). The gravitational waves from the inspiral phase, when the binary orbit decays under gravitational-wave emission

prior to merger, are accurately modeled by post-Newtonian approximants in the band of the detector's sensitivity for a wide range of binary masses where the merger and ringdown occur outside of the detector band [76]. The expected gravitational-wave signal, as measured by LIGO and Virgo, depends on the masses ( $m_{\text{NS}}, m_{\text{comp}}$ ) and spins ( $\vec{s}_{\text{NS}}, \vec{s}_{\text{comp}}$ ) of a neutron star and its more massive companion (either another NS or a BH), as well as the spatial location ( $\alpha, \delta$ ), inclination angle  $\iota$ , and polarization angle  $\psi$  of the orbital axis, among other parameters. In general, the power of matched filtering depends most sensitively on accurately tracking the phase evolution of the signal. The phasing of compact binary inspiral signals depends on the masses and spins, the time of merger, and an overall phase. Spin introduces additional angles, but we omit more explicit discussion.

We adopt a discrete bank of template waveforms that span a two-dimensional parameter space (one for each component mass) such that the maximum loss in signal to noise ratio (SNR) for a binary with negligible spins would be 3% [77]. While the spin is ignored in the template waveforms, we verify that the search can still detect binaries with most physically reasonable spin orientations and magnitudes with only moderate loss in sensitivity. The number of template waveforms required to achieve this coverage depends on the detector noise spectrum.

The templates in the bank are deliberately simple inspiral waveforms, as we are describing a low-mass ( $\leq 40 M_{\odot}$ ) search and neither the merger nor ringdown phases contribute much to the SNR. The templates are computed to second post-Newtonian order and are simply computed in terms of elementary functions in the

frequency domain, as they are computed with the stationary phase approximation (SPA).

We filter the data from each of the detectors through each template in the bank. If the matched filter SNR exceeds a threshold, the template masses and the time of the maximum SNR are recorded. For a given template, threshold crossings are clustered in time; that is, only the loudest-SNR candidates are kept in each cluster, where a cluster is defined by a sliding time window equal in duration to the duration of the template [78].

Triggers identified in each detector are further required to be found in at least one other detector with consistent time and mass parameters, up to the uncertainty of time and mass estimation measurements. Our algorithm takes into account the covariance between these parameters [79]. Triggers found to be compatible in this way are called *coincident triggers*. This consistency requirement significantly reduces the number of background triggers that arise from matched filtering in each detector independently and reduce the number of times one must calculate the computationally costly waveform consistency tests, performed in a second hierarchical stage. The coincidence test is described in greater detail in Sec. 6.6.

To prepare for the second stage, we create a reduced template bank for each detector in which templates that did not contribute to coincidences are culled. These reduced banks are then match-filtered once again, but with the  $\chi^2$  and  $r^2$  statistics computed. These statistics are described in slightly greater detail in Sec. 6.5. Candidates with high  $\chi^2$  or  $r^2$  are cut and the  $\chi^2$  is folded into the candidate ranking

as described in Sec. 6.5). The surviving single-detector triggers are subjected to coincidence testing once again and the list of coincident triggers at this stage are then called candidate events.

An optional feature in the candidate-generation portion of the pipeline is that of software injections. Software injections, often just called injections, involve simulating waveforms and adding them to the data to test the efficiency of the search in detecting a population of signals. Injections are also effective diagnostic tools to test the proper functioning of the pipeline at various intermediate stages in the presence of something loud. Despite attempts at mitigation (e.g. employing a median in PSD estimation), too many loud signals in the same analysis chunk can corrupt the PSD estimate, so we inject signals no closer than 800 s apart. We can make many injections by injecting widely spaced injections into the same data again and again. The matched-filtering code is smart enough to filter only a subset of data around each injection rather than an entire stretch of data to save computation. More details on the signals we inject can be found in Sec. 6.7.2.

The full untriggered pipeline is summarized in the workflow of Fig. 11.

## 6.5 Waveform consistency tests

The matched filter is optimal for Gaussian noise in the sense that it is monotonic with the likelihood ratio, which tells us how much to update our beliefs about the existence of a signal. When applied to noise with non-Gaussian tails, it produces

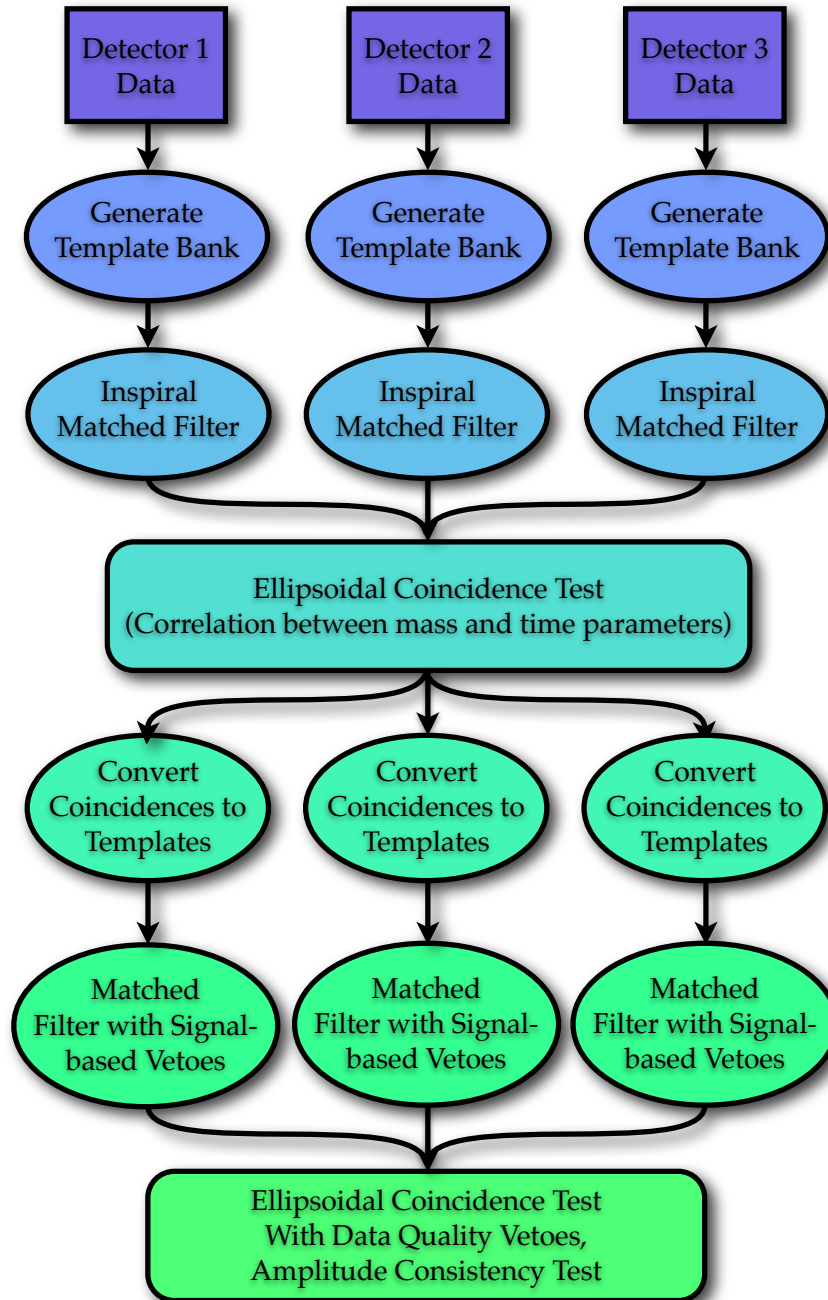


Figure 11 : Schematic of the untriggered S5/VSR1 CBC search pipeline up through candidate generation.

many spurious candidates, which weakens the ability of a search to identify real signals. Waveform consistency tests, also called signal-based vetoes, are techniques to discard or deweight triggers based on the consistency of the data near a trigger with what we expect from the signal in question. As of the S5/VSR1 science run, the CBC search applies two signal-based tests to reduce and refine its trigger sets. First, we compute a  $\chi^2$  statistic [80] to measure how different a trigger's SNR integrand looks from that of a real signal in several frequency bands; we discard triggers with large  $\chi^2$ . Second, we apply the  $r^2$  veto [81], which measures the duration that the  $\chi^2$  statistic stays above a threshold.

The SNR and  $\chi^2$  from a single detector combine into an effective SNR [82], as

$$\rho_{\text{eff}}^2 = \frac{\rho^2}{\sqrt{\left(\frac{\chi^2}{2p-2}\right) \left(1 + \frac{\rho^2}{250}\right)}}, \quad (6.1)$$

where  $p = 16$  is the number of degrees of freedom in the  $\chi^2$  statistic in this search.  $\rho_{\text{eff}}$  provides better separation between triggers due to real signals and spurious noise triggers than  $\rho$  alone.

## 6.6 Trigger consistency cuts in the untriggered search

For a two detectors whose readouts are uncorrelated and for a simple time-window coincidence scheme, we can express the rate of coincident triggers in an untriggered search as:

$$R_{12} = R_1 R_2 \Delta t \quad (6.2)$$

That is, the coincident rate of triggers is the product of the single-detector trigger rates times the duration of the coincidence window. The coincidence window is set by the inter-detector light-travel time plus some stretch to account for error in a trigger's end time to that of a real signal. The scale for the coincidence window is set by the separation between observatory corner stations. The LIGO Hanford and LIGO Livingston corner stations are separated by 3002 km (Euclidean distance, not surface distance), corresponding to a 10 ms light-travel time. Thus, for our simple time-window coincidence test, we would see single-detector trigger rates of 1 Hz reduced by a factor of  $\mathcal{O}(100)$ . The background reduction increases our detection confidence enough that only multiply-coincident triggers are considered gravitational-wave candidates.

For the S5/VSR1 low-mass search, the consistency test utilizes a geometrical technique that compares the time and mass parameters of two triggers, taking into account the correlations between these quantities [79]. This coincidence technique has become known as ellipsoidal thinca or *ethinca*, as it is a refinement of an older coincidence method called thinca. It offers significant background rejection relative to simple time coincidence, a factor of  $\mathcal{O}(10)$  in practice at binary black hole masses and slightly less at lower masses.

The technique works by using the Fisher information matrix of the template waveform normalized by a factor of  $\rho^{-2}$  as a metric in template space. The metric distance is called the mismatch and its complement is the overlap. The Fisher matrix is the inverse of the covariance matrix. It uses variables that are simply related to

the chirp mass, the normalized reduced mass, and the coalescence time. One can set a single threshold on the metric distance between two single-detector triggers.

One subtlety is that the detectors are separated by the inter-site light-travel time,  $t_{\text{LT}}$  and we should not penalize two triggers separated by less than this time. To this end, the ethinca implementation minimizes the metric distance while varying the time-delay between triggers over the range  $[-t_{\text{LT}}, t_{\text{LT}}]$ .

## 6.7 The triggered S5/VSR1 low-mass pipeline

The triggered pipeline slightly modifies the trigger-generation of the CBC search pipeline and adds some superstructure to generate candidates for foreground, background, and simulated signals injected into background, plus the implementation of likelihood-ratio ranking and Feldman–Cousins distance exclusions.

### 6.7.1 Modifications to untriggered candidate generation

Inside the candidate generation of Sec. 6.4, we modify the simulation machinery and the coincidence test.

The simulations are injected into off-source data, which span 2190 s or 36.5 minutes. In this time, the Earth spins about its axis, moving the GRB’s sky location with respect to the detectors’ antenna patterns and altering detector’s sensitivity to a gravitational-wave source at the GRB’s equatorial coordinates. We added the ability to make simulations at fixed Earth-fixed coordinates (fixed antenna pattern)

by shifting the right ascension of the simulation with its sidereal time relative to the GRB time. In this way, our simulations allow us to accurately measure our search efficiency to a CBC associated with a particular GRB.

The key to the ethinca consistency test, described in Sec. 6.6, is determining the metric distance between two triggers in mismatch space. There is no penalization for the inter-site light-travel time. In a search for a GRB counterpart, the time-delay is known since we know the sky location of the GRB and locations of the detectors with time. Thus, optimizing over time delay is inappropriate. We enabled the trigger-consistency code to fix the time delay based on the Earth-fixed coordinate of the GRB and thus narrow the coincidence window down to the coalescence time measurement uncertainty alone ( $\approx (10/\rho)$  ms) and lower the background rate further.

### 6.7.2 Pipeline superstructure

Using our modified untriggered pipeline, described in Sec. 6.7.1, as a building block, we can construct the triggered search pipeline. That is, we can run the candidate generation separately on the off-source trial, on the off-source trials, and also on the injection trials and run them as logical units from a master controlling workflow. Finally, the resulting candidates are collected and put through the likelihood and interpretation calculations, described in Chapters 4 and 5, respectively.

Before candidate generation can begin, the work must be planned. We begin by determining detector availability and data quality in the 2190s around a given

external trigger. If two or more instruments have science-quality data available, the analysis proceeds. We then divvy up the available multiply-coincident time into trials as described in Sec. 6.1. With the list of available detectors and trial segments in hand, we can write the instructions for the batch scheduler to execute the analysis.

The injection workflow is actually split into several nearly identical workflows, distinguished by waveform family and distinct parameter choices. When we inject simulated signals, we rely on a faithful reproduction of realistic waveforms. Numerical relativity can produce extremely faithful simulations, but they are tremendously computationally expensive. Instead, we use approximations to the true waveforms at some fixed post-Newtonian order and including some subset of realistic physics. Sometimes-supported physics includes deviations from point-particle solutions, spin, spin-induced orbital precession, merger dynamics, and post-merger ringdown. We run parallel injection workflows with different waveform families to ensure the robustness of our candidate generation pipeline against perturbations in the waveforms, especially since our waveform templates are very simple, containing none of the optional physics listed above. Additionally, supporting multiple injection workflows proves useful if we decide at a later stage to do additional simulations for improved statistical uncertainty or to target a particular region of parameter space.

Finally, we arrange that the candidates should pass through the likelihood-ratio ranking and Feldman–Cousins exclusion codes. A technical detail is that between

the candidate generation and the likelihood-ratio ranking, we cluster the candidates into  $(\text{trial}, \overline{\mathcal{M}}, C)$  bins, with  $\text{trial}$  referring to the 6 s trial of the candidate and  $\overline{\mathcal{M}}$  and  $C$  as defined in Sec. 4.3.2, keeping on-source, off-source, and injection trials separate, and bin the  $(m_{\text{companion}}, D)$  values of the injections. By clustering, I mean that in each of the  $(\text{trial}, \overline{\mathcal{M}}, C)$  bins, we remove all but the loudest candidate as ranked by  $\rho_{\text{eff}}$ . This is reasonable due to our using the CDF instead of the PDF on  $\rho_{\text{eff}}$  (see Sec. 4.3.2), which is effectively a statement that we expect the likelihood ratio to be monotonic in  $\rho_{\text{eff}}$ . The clustering provides us with a vastly reduced list of candidates that are guaranteed to be the loudest within their own trials. This diminution enables us to run and rerun the likelihood-ratio ranking and Feldman–Cousins codes much more quickly and modularly, which was important in commissioning new features.

The full triggered pipeline is summarized in the workflow of Fig. 12.

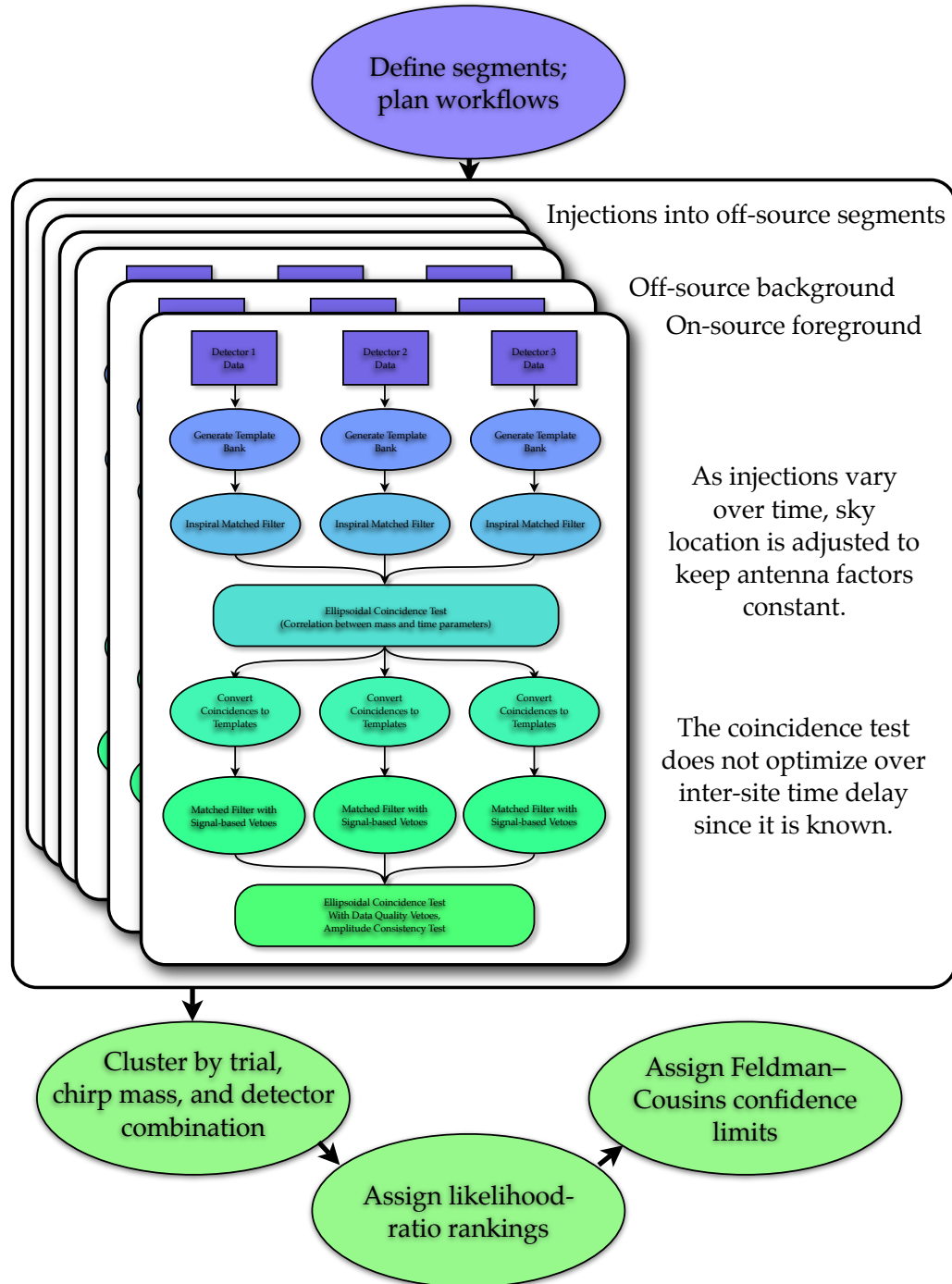


Figure 12 : Schematic of the triggered S5/VSR1 CBC search pipeline. It makes repeated use of the candidate-generation pipeline (shown larger in Fig. 11) used in the untriggered search with minor differences in the injection and coincidence machinery related to the fixed sky location of the search targets.

# Chapter 7

## A worked example: GRB 070201

In this chapter, we apply the pipeline of Chap. 6 to a single short GRB, GRB 070201, tracing in some detail through each stage of the analysis. Chapter 8 defines the full set of GRBs and summarizes the results more briefly, also pulling them together to make a population statement.

### 7.1 The significance of GRB 070201

GRB 070201 was an intense, short duration, hard spectrum GRB, which was detected and localized by three IPN spacecraft (Konus–Wind, INTEGRAL, and MESSENGER); it was also observed by Swift (BAT) but with a high-intensity background as the satellite was entering the South Atlantic Anomaly [83]. The burst light-curve exhibited a multi-peaked pulse with duration  $\sim 0.15$  s, followed by a much weaker, softer pulse that lasted  $\sim 0.08$  s. Using early reports, Perley and Bloom [84] pointed

out that the initial IPN location annulus of the event intersected the outer spiral arms of the Andromeda galaxy (M31). The refined error box, centered  $\approx 1$  degree from the center of M31, was later reported [85, 86], and it still overlaps with the spiral arms of M31 [see Fig. 13 and [87, 88]]. Based on the Konus–Wind observations [87, 89], the burst had a fluence of  $1.57_{-0.21}^{+0.06} \times 10^{-5} \text{ erg cm}^{-2}$  in the 20 keV–1 MeV range.

It was also pointed out [89] that if the burst source were actually located in M31 (at a distance of  $\simeq 770$  kpc) the isotropic energy release would be  $\sim 10^{45}$  erg, comparable to the energy release in giant flares of soft gamma repeaters: e.g., the 5<sup>th</sup> March 1979 event from SGR 0526–66 ( $\sim 2 \times 10^{44}$  erg in the initial pulse) and the 27<sup>th</sup> December 2004 event from SGR 1806–20 ( $\sim 2 \times 10^{46}$  erg). Conversely if the event had an isotropic energy release more typical of short hard GRBs, e.g.,  $\sim 10^{48}$ – $10^{52}$  erg [91], then it would have to be located at least  $\sim 30$  times further than M31 (i.e., further than  $\sim 23$  Mpc).

## 7.2 Data and data quality

At the time of GRB 070201, the LIGO Hanford detectors were stable and recording science-quality data, while the LIGO Livingston, GEO600, and Virgo detectors were not taking data. A standard measure of the sensitivity of a detector to gravitational waves is the distance to which an optimally oriented and located double NS binary would produce a response in the datastream that, when optimally filtered for the inspiral waves, peaks at an SNR of 8 (see, e.g. [92] and references therein). At the

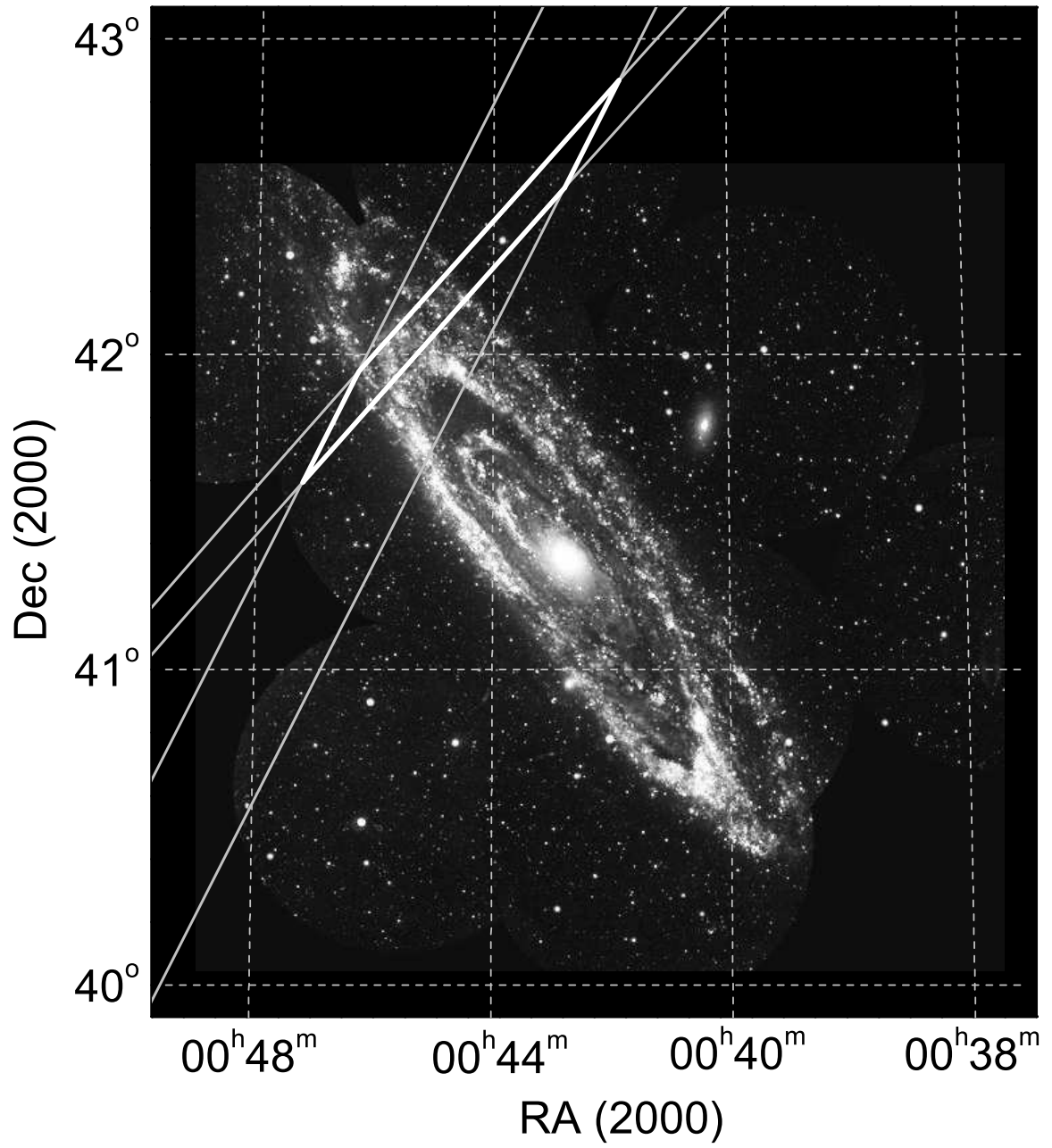


Figure 13 : UV image of the M31 galaxy and the  $3\sigma$  IPN error box of GRB 070201, reproduced directly from [90].

time of GRB 070201, this distance was 35.7 Mpc and 15.3 Mpc for the H1 and H2, respectively. However, the sensitivity of a detector to a gravitational wave from a non-optimally oriented source depends on the location of the source on the sky and on the polarization angle  $\iota$  of the waves. In the case of compact binaries, it also depends on the inclination angle of the orbital plane relative to the line of sight. At the time of GRB 070201, the binary inspiral reach in the direction of M31 was only about 43% of this maximum, assuming a face-on  $\iota = 0$  inclination. More details of the instrumental sensitivity in S5/VSR1 can be found in Sec. 3.4.

We applied a suite of data-quality tests to the data, but found no anomalous behavior in either instrument at the time of GRB 070201 nor in the 2190 s off-source segment for the current CBC GRB search.

## 7.3 Diagnostics throughout the pipeline

### 7.3.1 Template banks

Because the full analysis time of 2190 s is longer than the default matched filtering time of 2048 s, the analysis is done in two parts, with a separate median PSD for each and therefore separate template banks. Nonetheless, the data are fairly stationary on these timescales and the template banks do not vary significantly. We construct template banks such that there is a maximum of 3% mismatch at any point in the designated region. We define the boundaries of the bank by requiring  $m_{\text{component}} > 1 M_{\odot}$  and  $m_{\text{total}} < 40 M_{\odot}$ .

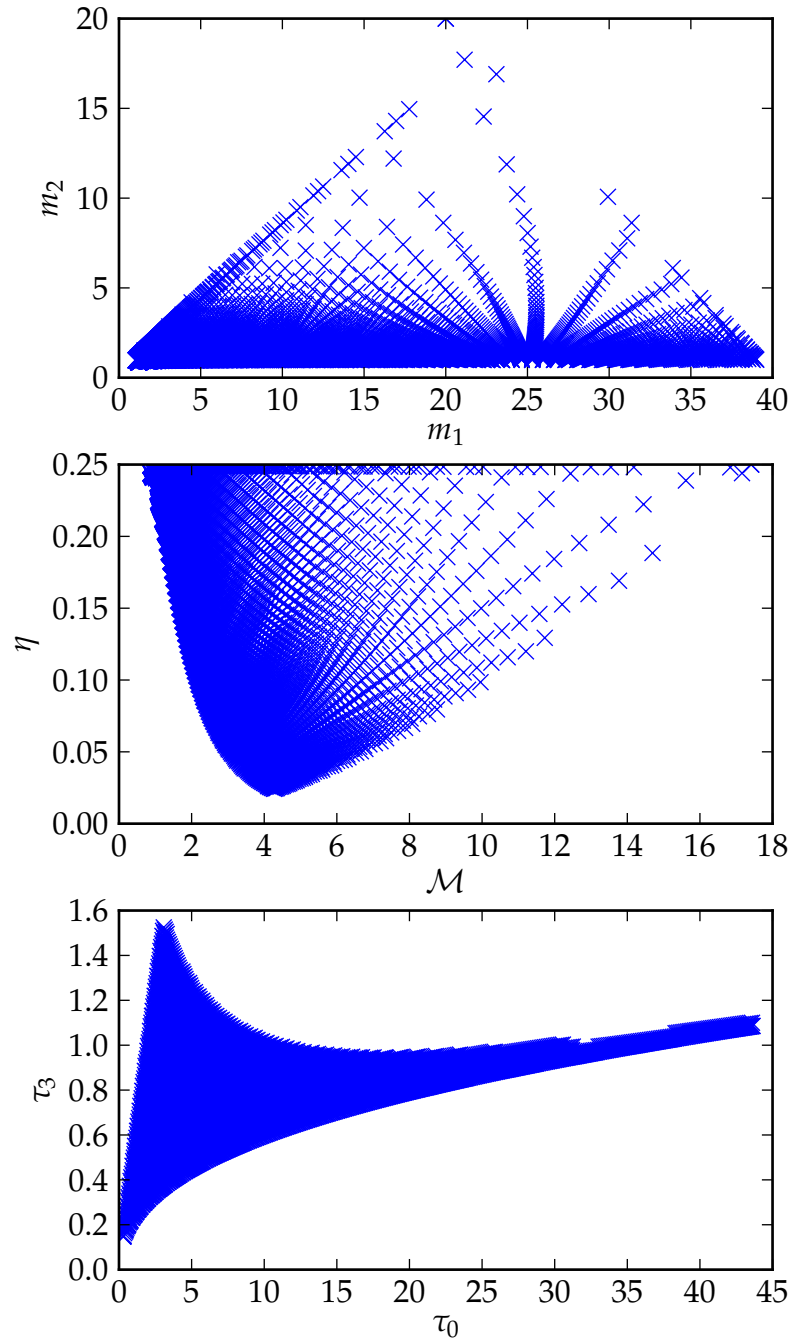


Figure 14 : This GRB 070201 template bank for H1 includes 6993 templates.

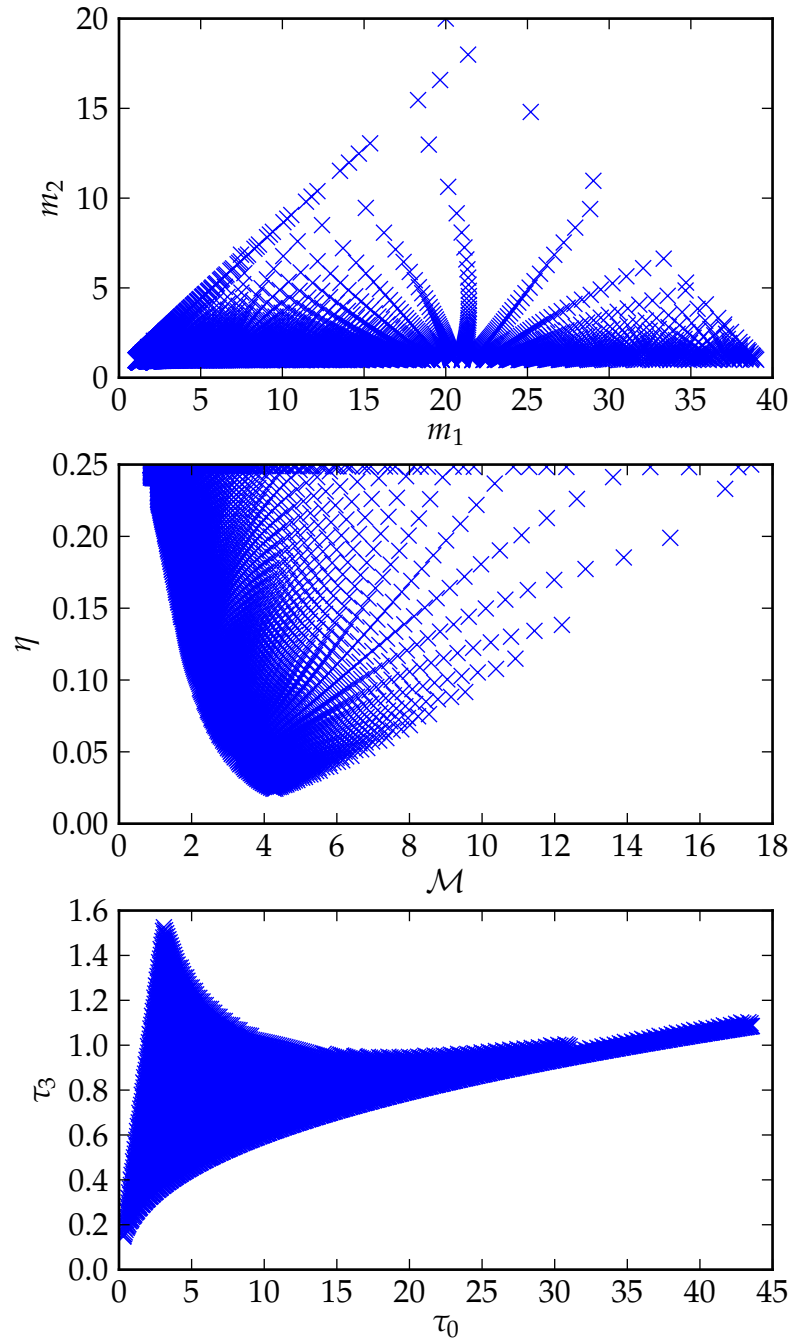


Figure 15 : This GRB 070201 template bank for H2 includes 5328 templates.

Figures 14 and 15 show template banks for the first half of the GRB 070201 data for H1 and H2, respectively. The pairs  $(m_1, m_2)$ ,  $(\mathcal{M}, \eta)$ , and  $(\tau_0, \tau_3)$  can be converted into one another. Note the diagonal boundaries in  $(m_1, m_2)$  corresponding to the minimum component mass and maximum total mass. Note also that the bank was constructed with uniform density in  $(\tau_0, \tau_3)$ , with a few extra templates along the boundaries to ensure coverage of the entire region. H1 has more templates than H2 because its spectrum is flatter; inspiral signals will spend more time in band and accumulate more cycles for H1, allowing it to discern a smaller difference between two signals.

### 7.3.2 Single-detector distributions

After the first stage of matched filtering, we have triggers and their raw SNR values, from which we can characterize the behavior of each instrument. Indeed, it is statistical information about triggers at this stage that feeds into data quality studies. For H1–H2 GRBs, we chose SNR thresholds of 5.5 and 3.5, respectively, as H2 limits our sensitivity by approximately a factor of two. We omit triggers from the buffer region (see Sec. 6.1 for a reminder about the segmentation), as they are not used in the analysis at any point.

Figure 16 shows the SNR versus time of triggers in both H1 and H2 in the off-source region of GRB 070201 and Fig. 17 shows the histogram of SNRs. We see that H2 has a loud trigger with an SNR near 9.5, but otherwise the stretch is not significantly elevated relative to H1. Anecdotally, the level of non-Gaussianity and

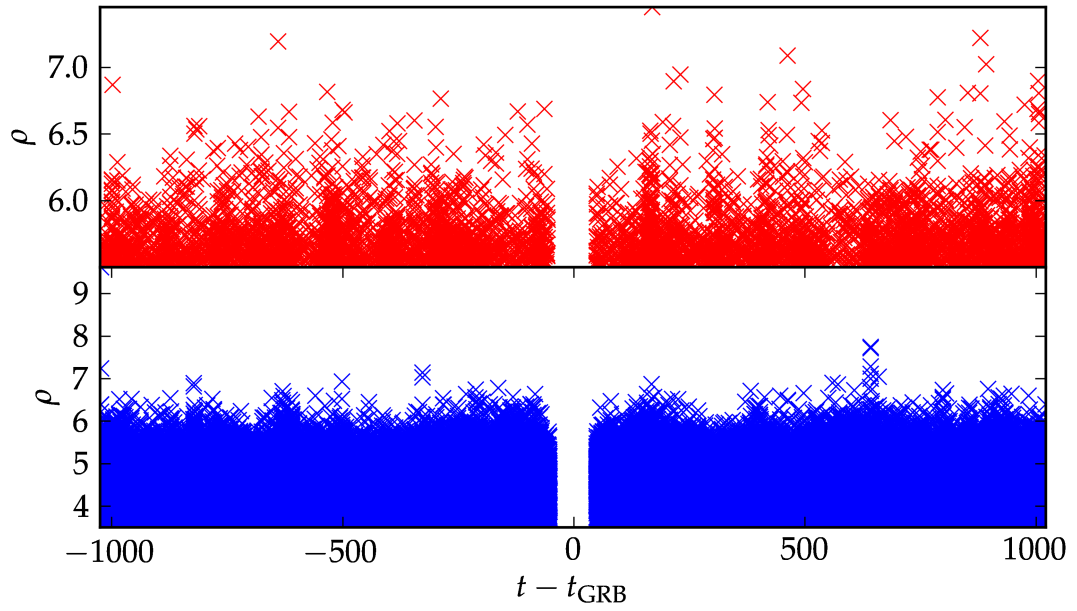


Figure 16 : Matched-filter SNR versus time for H1 (top) and H2 (bottom) around GRB 070201. The central gap arises from the omission of the on-source and buffer segments.

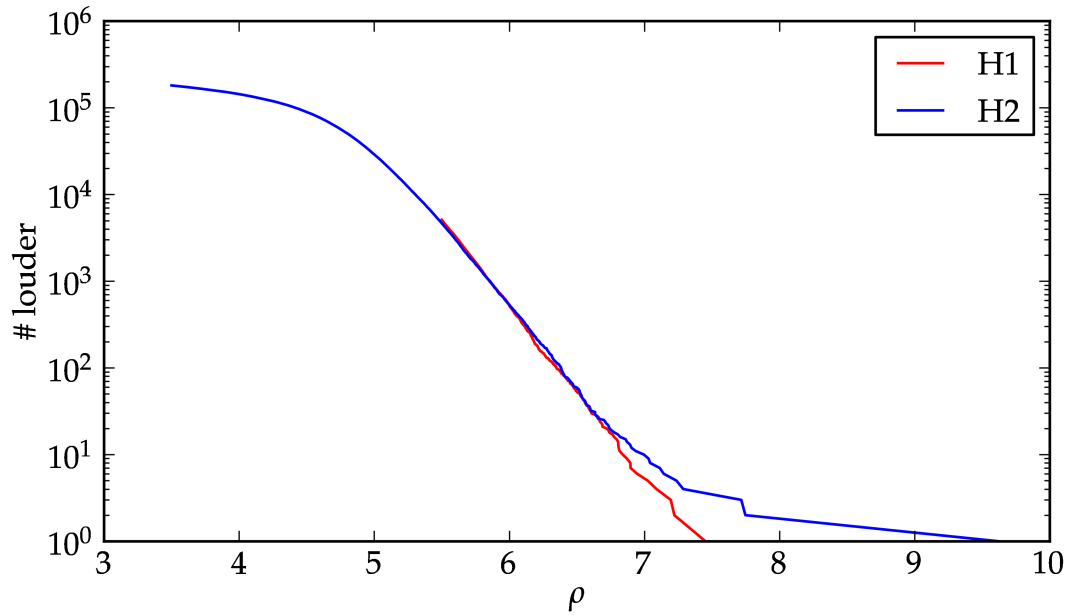


Figure 17 : Histograms of SNR for H1 and H2 around GRB 070201. The histograms are cumulative from the right.

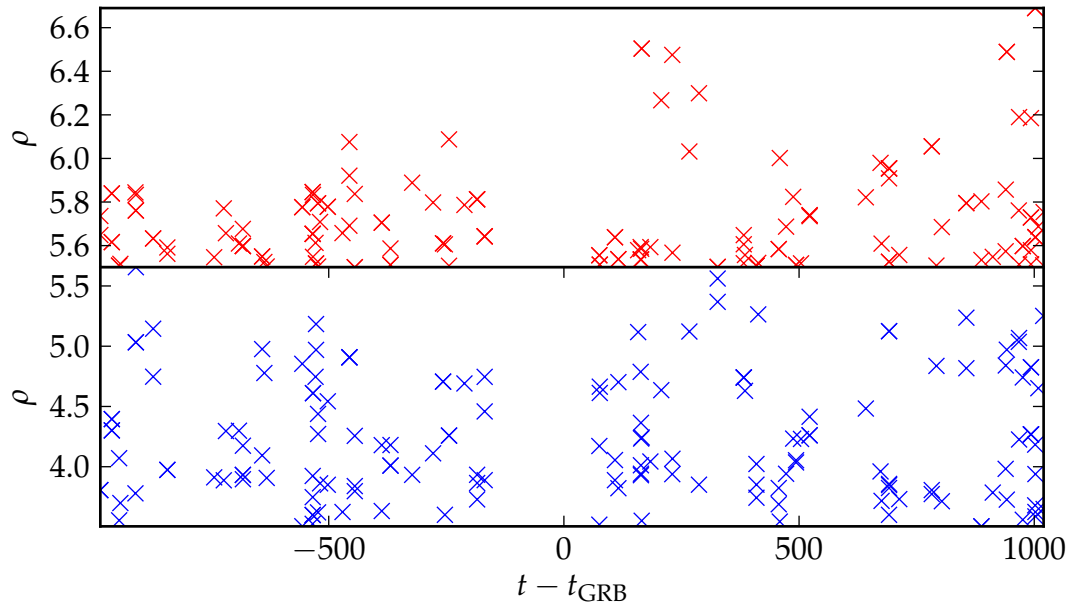


Figure 18 : Matched-filter SNR versus time for coincident H1 (top) and H2 (bottom) triggers around GRB 070201. The central gap arises from the omission of the on-source and buffer segments.

short-timescale non-stationarity we see in these plots is average to good relative to similar stretches of time in all instruments. The significantly lowered threshold of H2 leads to a vastly elevated trigger rate; while H1 yielded 5099 triggers in this time or 2.6 triggers per second, H2 yielded 181026 triggers or 93 triggers per second.

### 7.3.3 Coincidence cuts

The first-stage match-filter triggers are passed through the ethinca coincidence test, described in Sec. 6.6. We used a ellipsoid scaling parameter threshold of 0.8 for all S5 GRBs.

Figure 18 shows the SNR versus time of coincident triggers in both H1 and H2 in the off-source region of GRB 070201 and Fig. 19 shows the histogram of

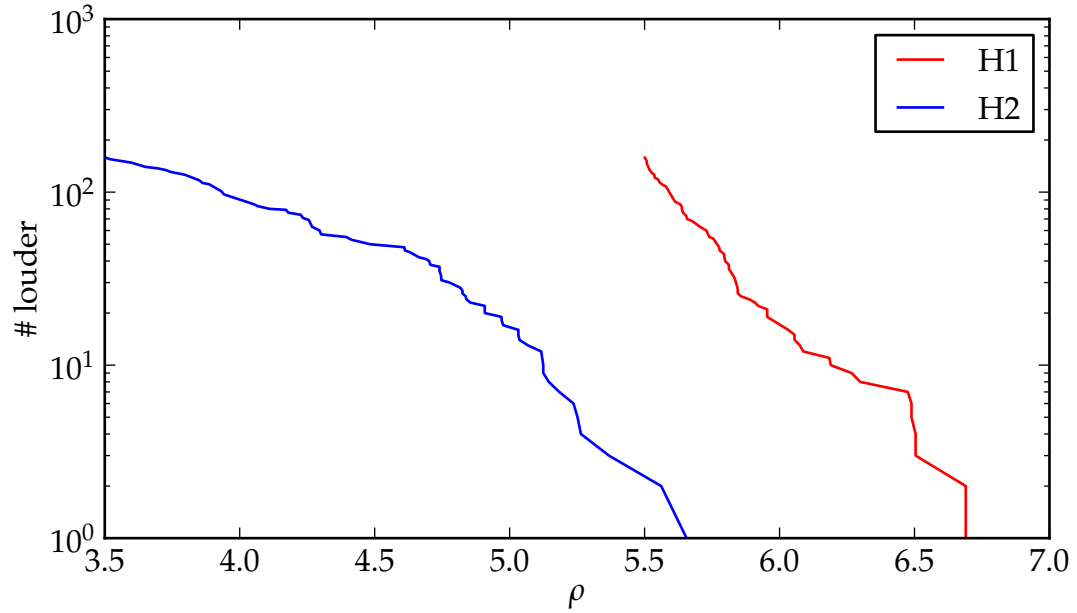


Figure 19 : Histograms of SNR for H1 and H2 around GRB. The histograms are cumulative from the right.

SNRs. Immediately we see the orders of magnitude reduction in trigger rate that motivated coincidence techniques, with 182 surviving coincidences. For H1, which had the lower trigger rate previously, we see improvement by a factor of 28. Note also how  $\rho$  axes are significantly rescaled relative to Figs. 16 and 17; sensitivity distance scales inversely proportionally to SNR and detection rate scales cubically with distance.

Finally, let's look at the down-selected template banks in Figs. 20 and 21 for H1 and H2, respectively. We see vast reductions in the sizes of the banks, factors of 75 and 46, respectively. Note that while matched filtering proceeds in blocks of 2048 s, the coincidence testing proceeds in blocks of 3600 s, which mixes adjacent banks together before the down-selection of templates for the second stage. This often

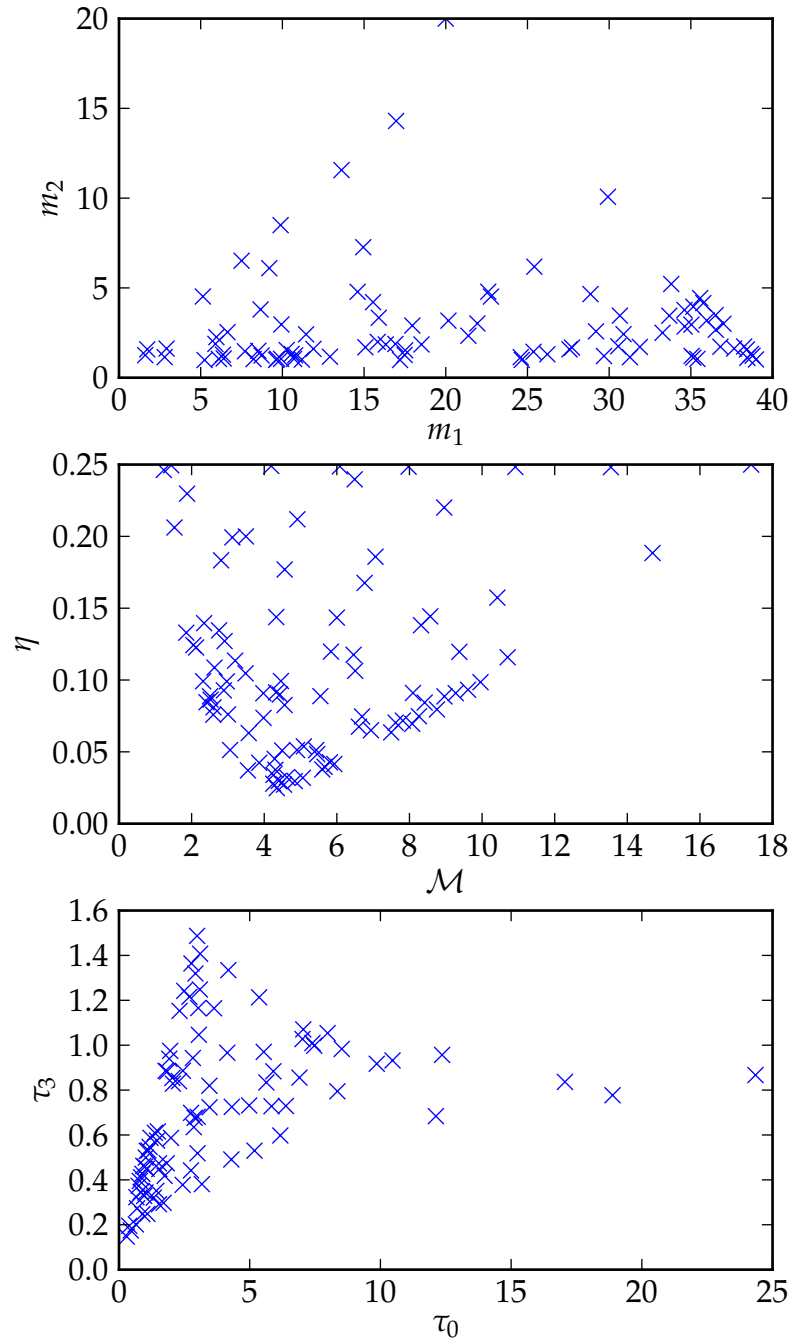


Figure 20 : This GRB 070201 second-stage template bank for H1 includes 93 templates.

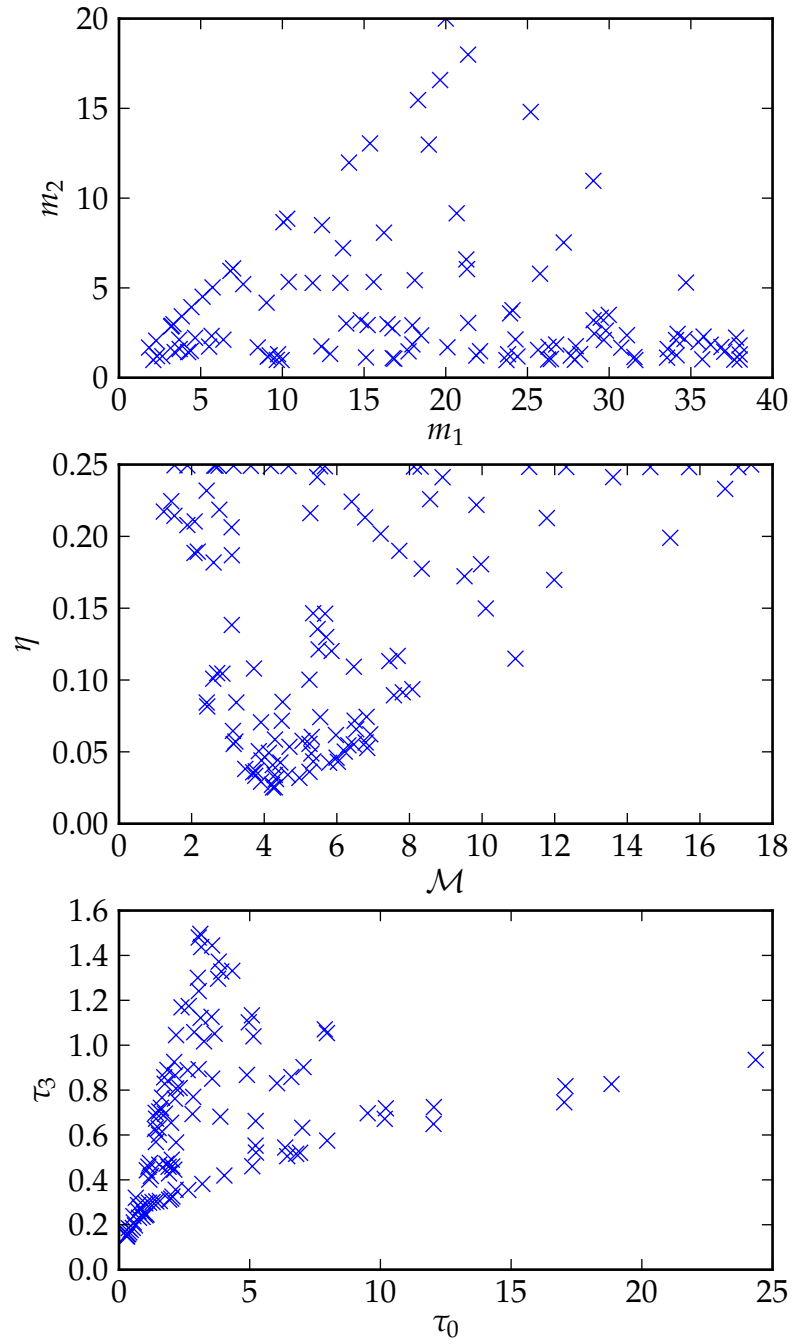


Figure 21 : This GRB 070201 second-stage template bank for H2 includes 116 templates.

leads to double coverage of the relevant template space and inflates the number of templates at this stage, which while suboptimal, will not compromise detection. Finally, comparing the number of templates to the number of coincidences, 182, we see that each template that gave a trigger tended to give multiple triggers.

#### 7.3.4 Waveform consistency cuts

Our waveform consistency tests  $\chi^2$  and  $r^2$  are somewhat computationally expensive, so are only computed for the reduced template bank discussed in Sec. 7.3.3. We make cuts based on the  $\chi^2$  and  $r^2$  values, reducing the trigger rate before a second round of coincidence and thereby allowing us to move from  $\rho$  to  $\rho_{\text{eff}}$  as a ranking statistic, which provides superior discrimination between signal and noise. The coincidences at this stage are our final candidates.

Figures 22 and 23 show our now-familiar SNR versus time and SNR histograms after the second hierarchical step of template bank reduction, second matched-filtering with waveform consistency cuts, and a second round of coincidence. The number of coincidences is 190, slightly larger than after first coincidence. The increase stems from the suboptimality in the template-bank reduction discussed in Sec. 7.3.3 which wastes computation, but should not significantly affect results. Figure 24 shows the H2 SNR versus H1 SNR for both off-source and injection triggers. Asymptotically, the injection triggers follow the line of  $\rho_{\text{H1}} = (D_{\text{H1}}^{\text{horizon}} / D_{\text{H2}}^{\text{horizon}}) \times \rho_{\text{H2}} \approx (7/3) \times \rho_{\text{H2}}$  line down to where the background lies.

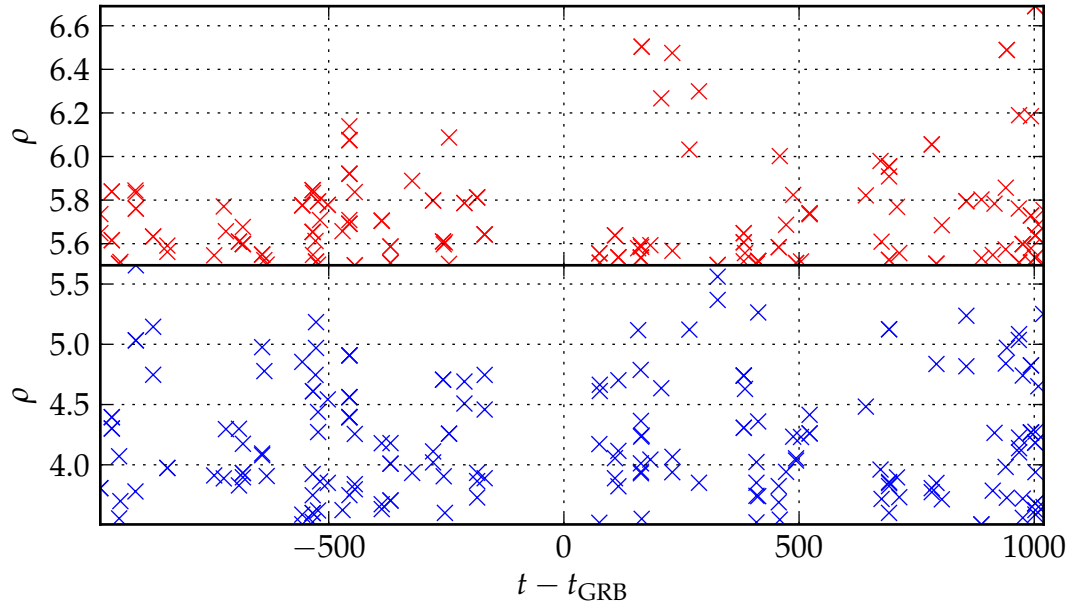


Figure 22 : Second-stage matched-filter SNR versus time for coincident H1 (top) and H2 (bottom) triggers around GRB 070201.

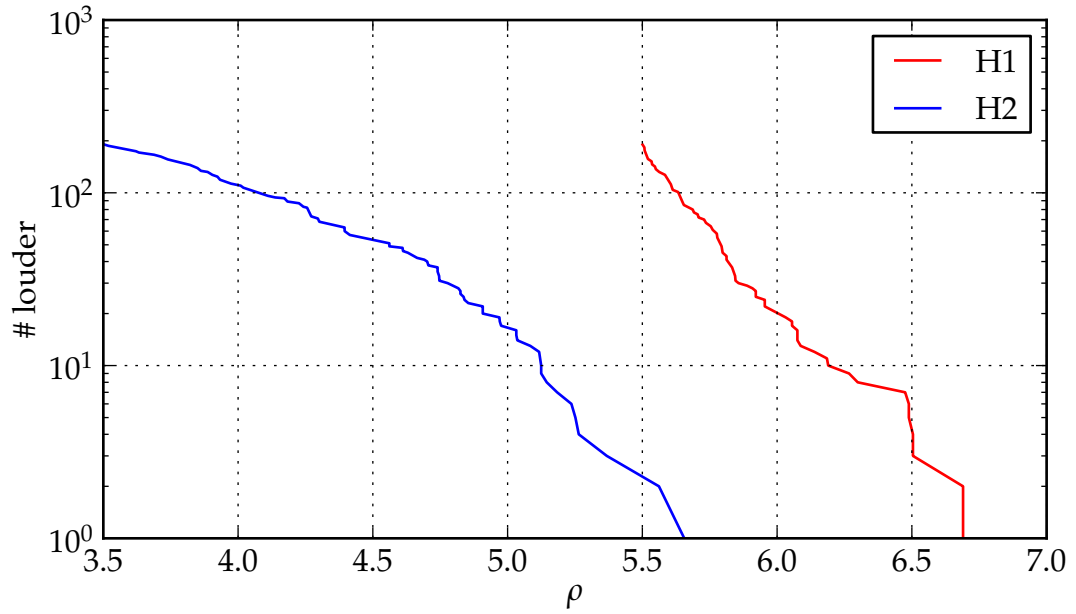


Figure 23 : Histograms of second-stage SNR for coincident H1 and H2 triggers around GRB 070201. The histograms are cumulative from the right.

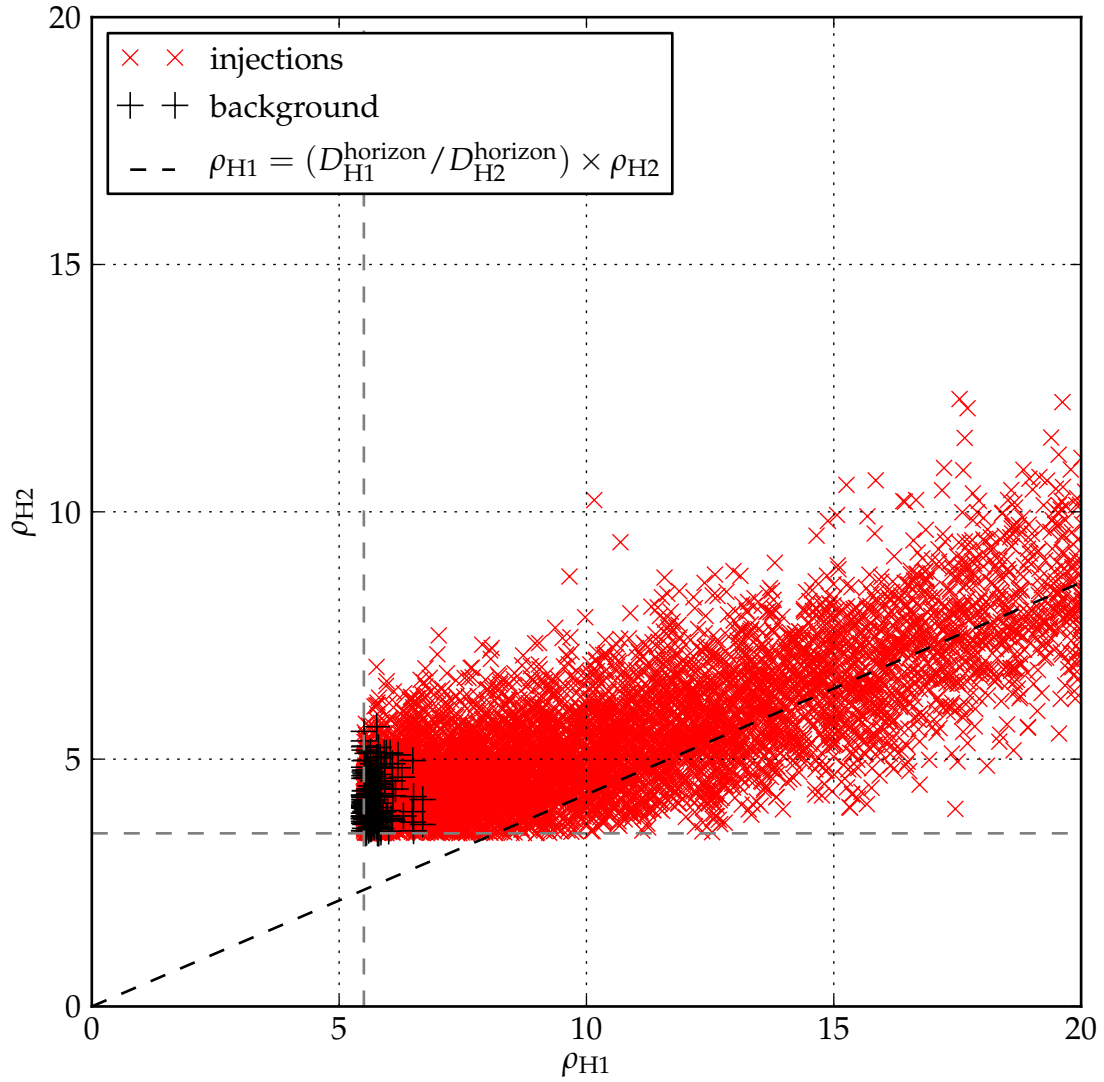


Figure 24 : H2 SNR versus H1 SNR for second-stage coincident triggers around GRB 070201. The light gray dashed lines indicate the SNR thresholds.

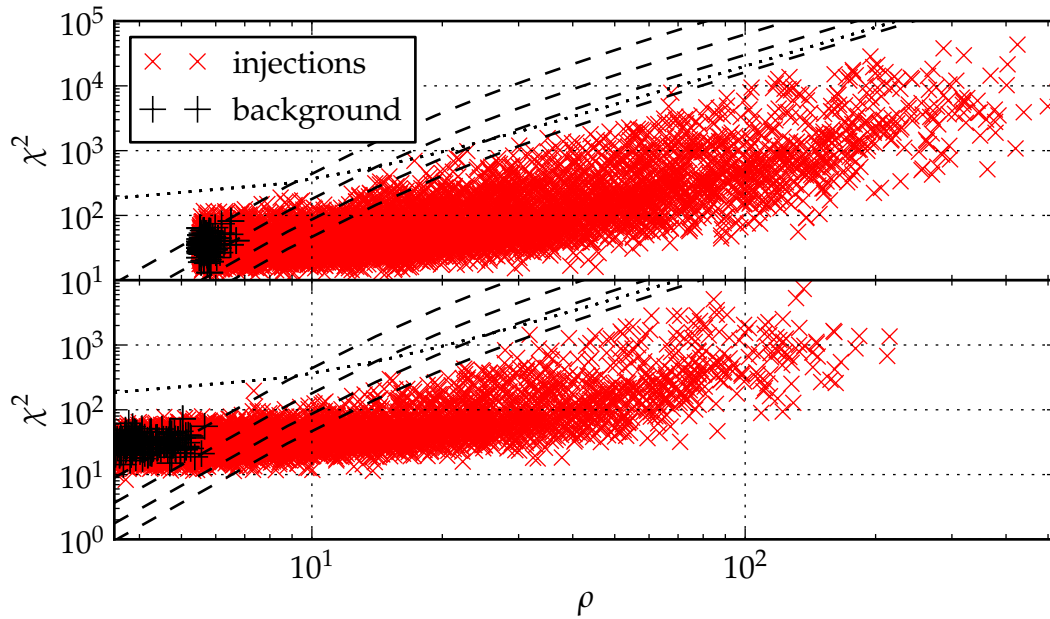


Figure 25:  $\chi^2$  versus  $\rho$  for second-stage coincident triggers around GRB 070201. H1 is the top panel and H2 is the bottom panel. The dashed lines represent contours of constant effective SNR; from left to right, they are  $\rho_{\text{eff}} = (4, 5, 6, 7)$ . The dotted line represents the  $\chi^2$  veto threshold.

Figures 25 and 26 show the distribution of  $\chi^2$  versus  $\rho$  for second-stage coincident triggers with the veto regions demarcated. It is difficult to tell the efficacy of the veto without a before-and-after comparison, but we can at least see that the thresholds do not cut into the injection population. We see an uninspiring lack of separation between foreground and background. Indeed, the data are well behaved and fairly Gaussian in the bulk. For Gaussian noise, matched-filtering SNR is the optimal ranking statistic, so there can be little improvement. We'll compare the various candidate rankings in Sec. 7.3.7 below.

The  $r^2$  versus  $\rho$  distributions appears in Fig. 27 with the veto regions demarcated. Again, it is difficult to tell the efficacy of the veto without a before-and-after

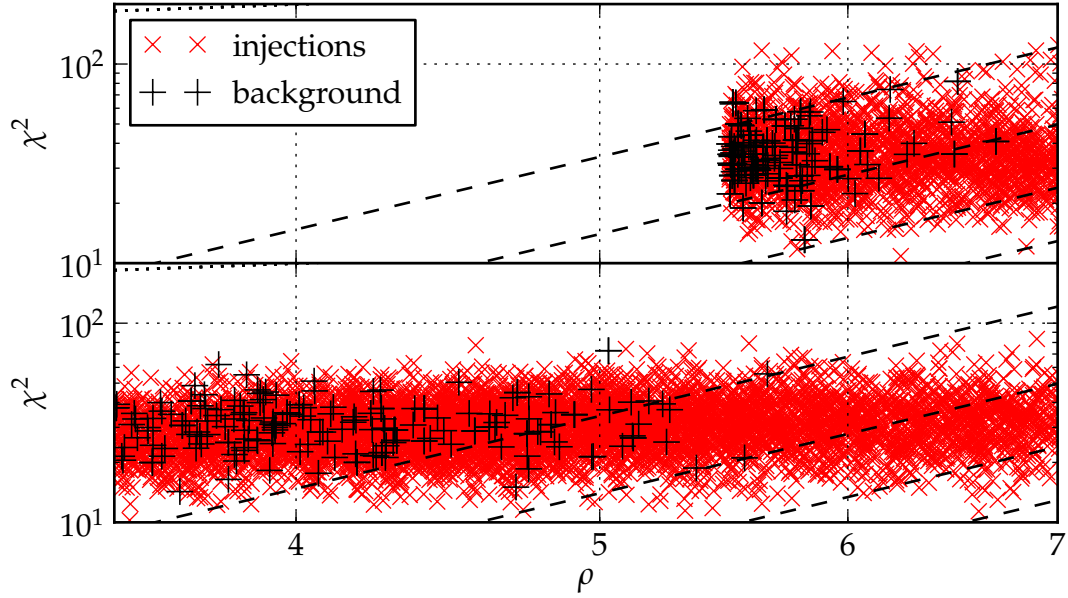


Figure 26 : Zoomed  $\chi^2$  versus  $\rho$  for second-stage coincident triggers around GRB 070201. H1 is the top panel and H2 is the bottom panel. The dashed lines represent contours of constant effective SNR; from left to right, they are  $\rho_{\text{eff}} = (4, 5, 6, 7)$ . The dotted line represents the  $\chi^2$  veto threshold.

comparison, but we can at least see that the thresholds do not cut into the injection population.

### 7.3.5 Effective SNR ranking

Applying the effective SNR ranking of Eq. (6.1) we obtain Figs. 28 and 29, which shows a plot of  $\rho_{\text{eff}}$  versus  $\rho$  for H1 and H2, respectively. Figure 30 shows H1 effective SNR versus H2 effective SNR. In data with a prominent tail of loud background glitches, the effective SNR ranking will vastly downgrade the significance of glitches. Here, with no background outliers, we do not witness much improvement.

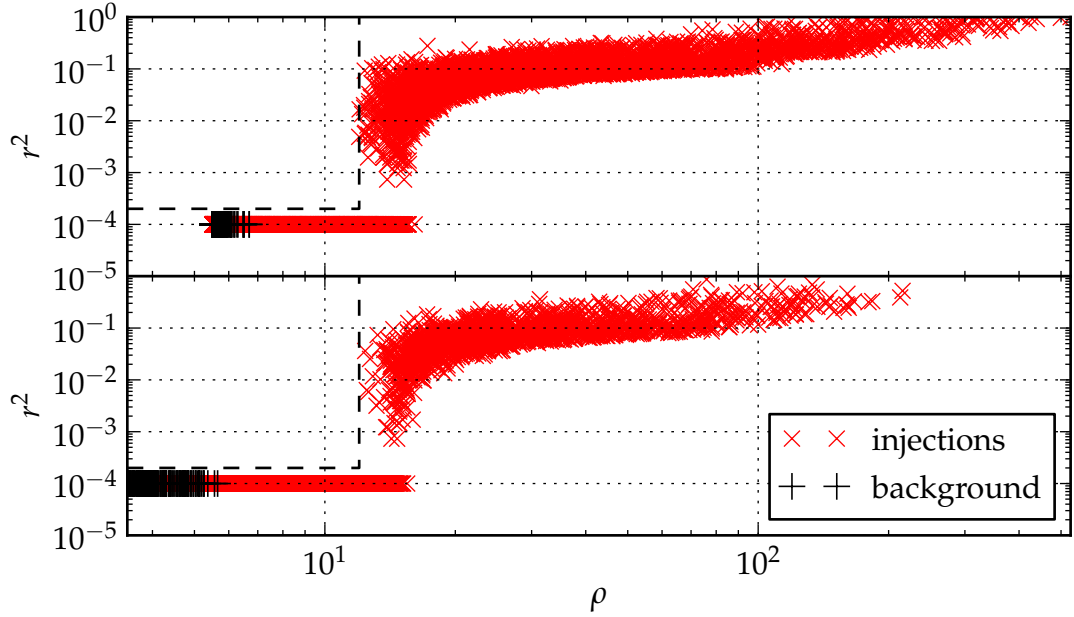


Figure 27 :  $r^2$  versus  $\rho$  for second-stage coincident triggers around GRB 070201. H1 is the top panel and H2 is the bottom panel. The dashed lines represent the veto thresholds. We discarded triggers to the upper left.

### 7.3.6 Effective SNR ranking by chirp mass

The likelihood-ratio ranking, described in Sec. 4.3, is intended to take into account the variation in trigger rate across the template bank and the differences in sensitivity of different detector combinations, plus the difference in sensitivity of certain templates to certain masses of signals.

Let us observe the distribution of combined effective SNR across three chirp-mass bins in Fig. 31. The same plot, but with the only the loudest events in each off-source (trial,  $\overline{\mathcal{M}}$ ) bin kept is Fig. 32. The  $\overline{\mathcal{M}}$  bin definitions were chosen in the S5 untriggered search and we chose not to modify them. They cover every template in our bank. If we retained combined effective SNR as our detection statistic, we

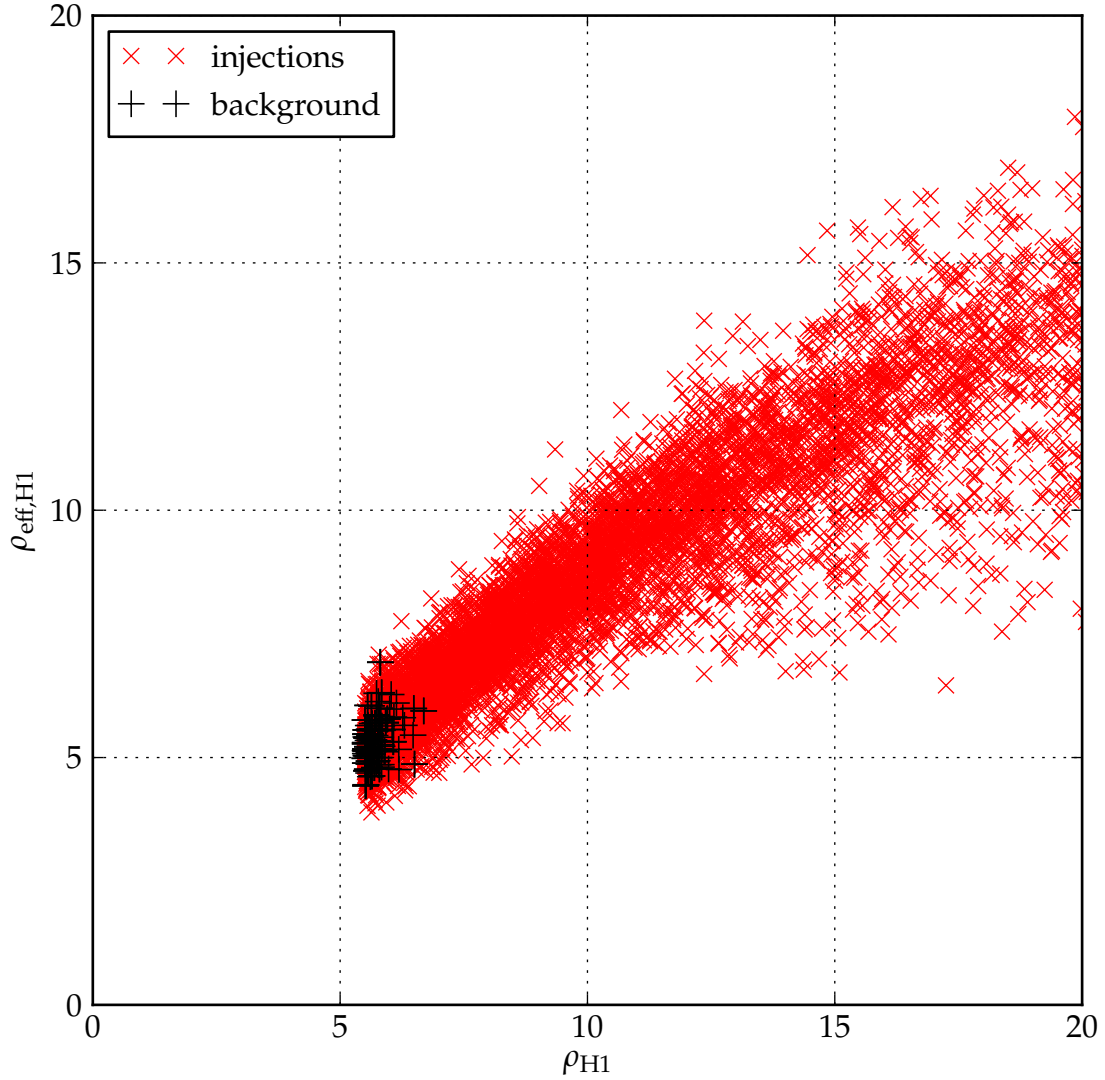


Figure 28 : H1 effective SNR versus H1 SNR for second-stage coincident triggers around GRB 070201. The black + markers represent background triggers and the red × markers represent injection triggers.

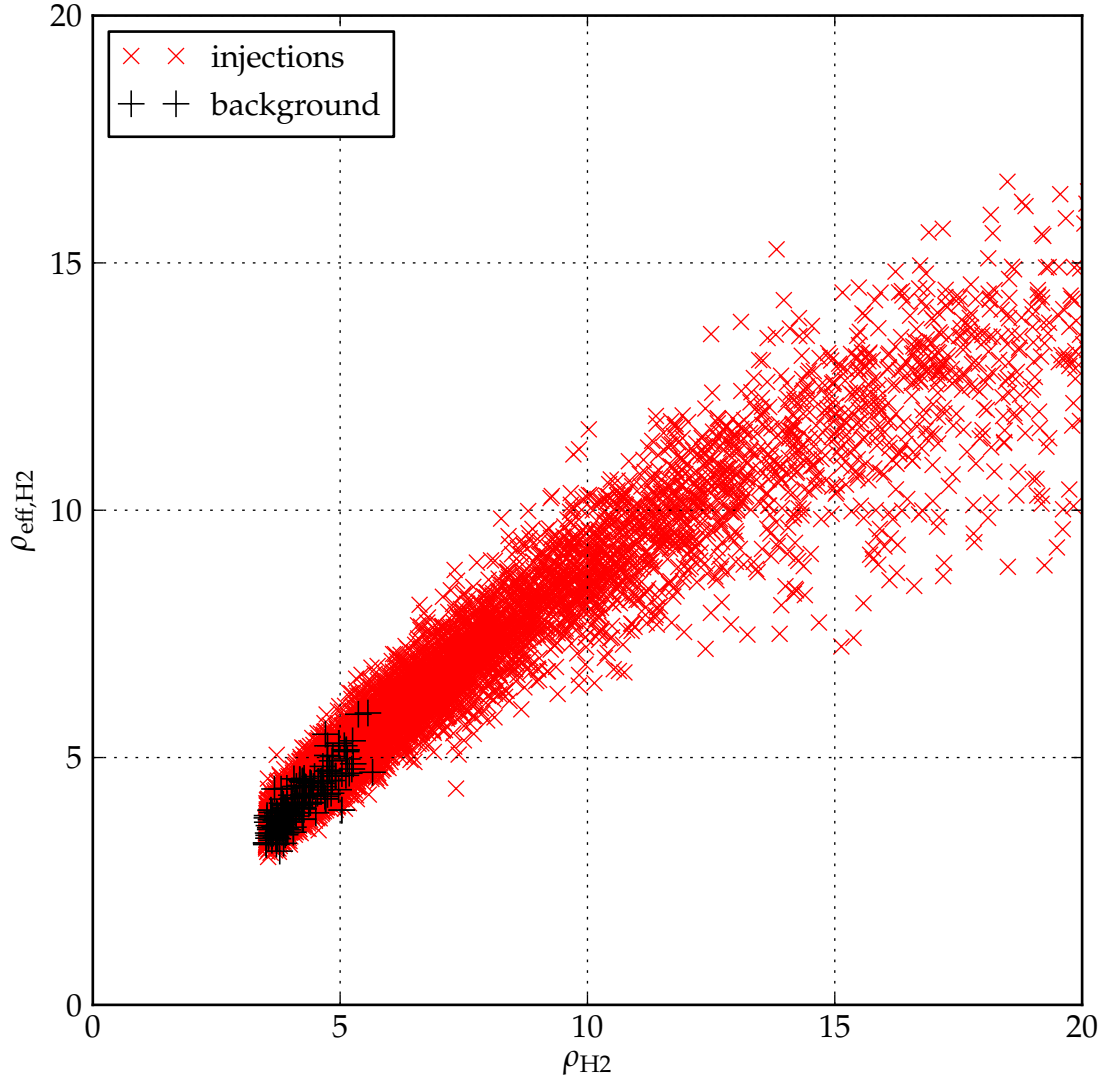


Figure 29 : H2 effective SNR versus H2 SNR for second-stage coincident triggers around GRB 070201. The black + markers represent background triggers and the red × markers represent injection triggers.

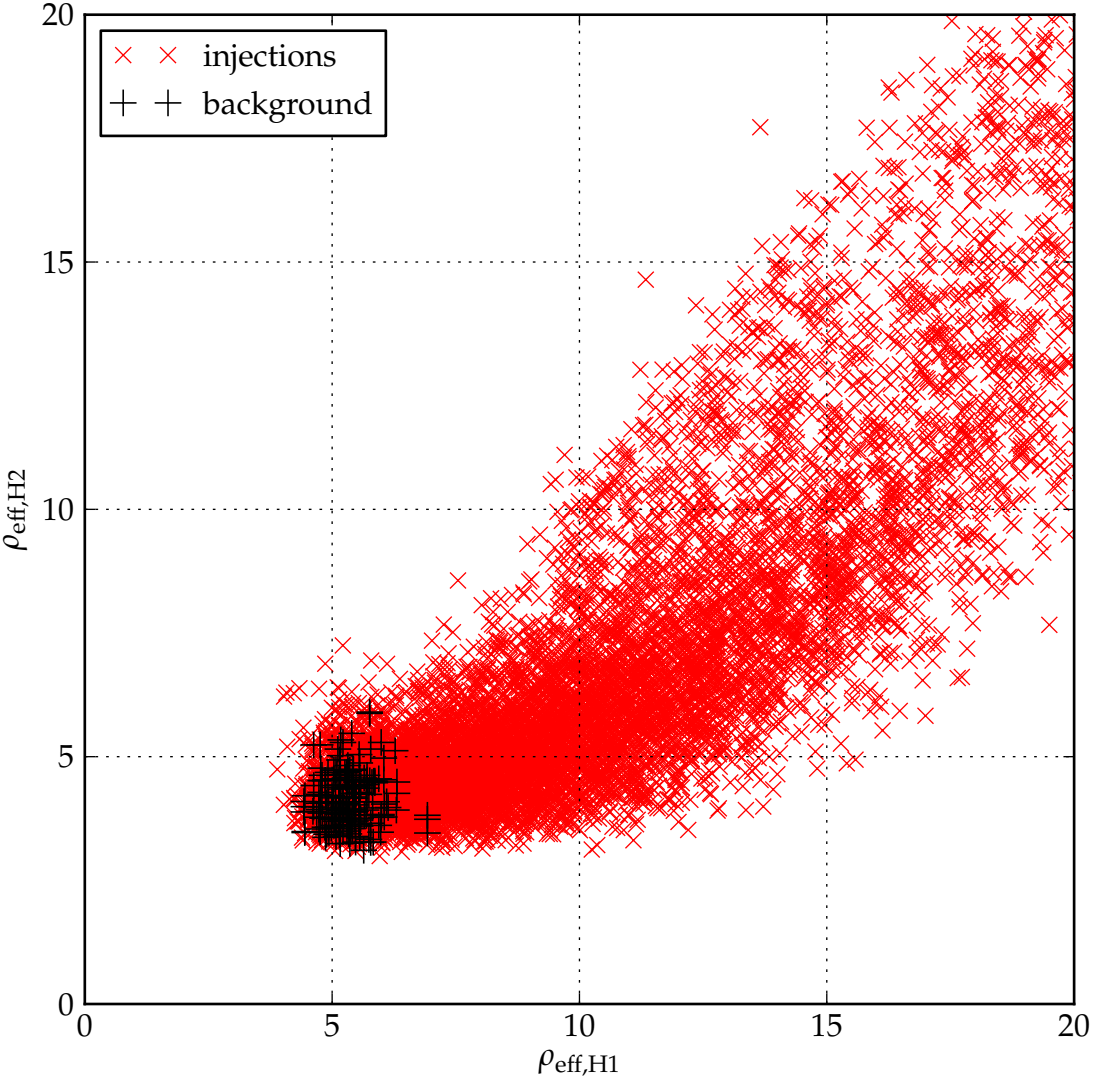


Figure 30 : H2 effective SNR versus H1 effective SNR for second-stage coincident triggers around GRB 070201.

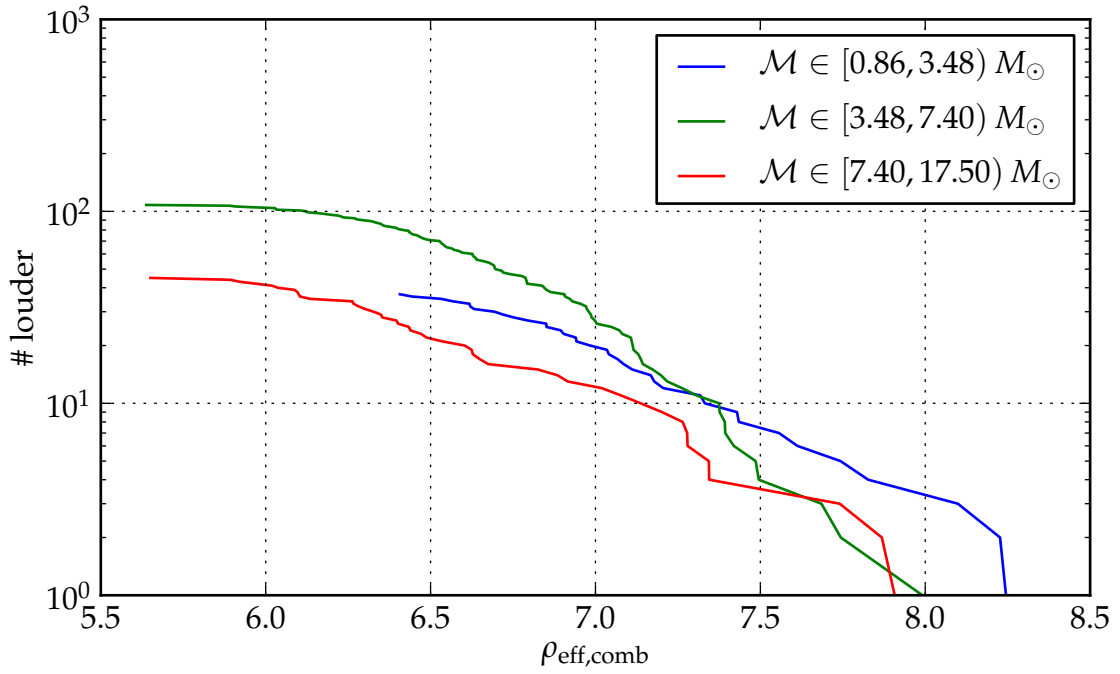


Figure 31 : Combined effective SNR for off-source coincidences around GRB 070201. The distributions are split by the mean chirp mass of the contributing triggers.

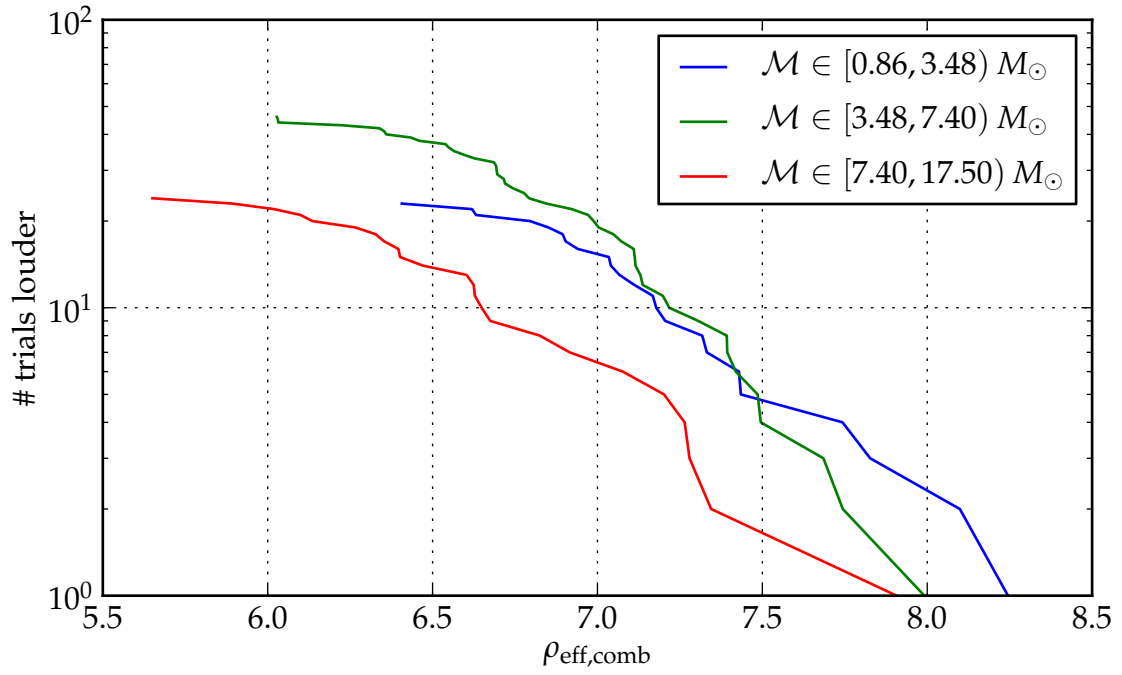


Figure 32 : Combined effective SNR for clustered off-source coincidences around GRB 070201. The distributions are split by the mean chirp mass of the contributing triggers. Clustering means that only the loudest candidate in each (trial,  $\overline{\mathcal{M}}$ ) bin are retained.

can see that at a fixed false-alarm probability, the tail would be dominated by the low-mass candidates. Separately determining false-alarm probability in each chirp mass bin increases our sensitivity to higher mass triggers.

### 7.3.7 Likelihood-ratio ranking

The efficiencies and false-alarm probabilities (numerators and denominators) of the likelihood ratios are measured. However, the false-alarm probabilities are extrapolated in the tail to provide finite estimates for triggers louder than all background. The extrapolation follows the form of Eq. (4.27). We chose to extrapolate from the 70<sup>th</sup> percentile candidate as sorted by effective SNR, where trials without candidates are omitted from this determination. We adopted the spectral index  $\alpha = -1.4$  to provide the best fit for a particular GRB and to maximize receiver operating characteristic (ROC) curves, discussed later. The ROC curves are not very sensitive to the tunings of these parameters.

Figure 33 shows the clustered off-source coincidences, as in Fig. 32, but now normalized to be a false-alarm probability and now demonstrating extrapolation in the tail, exactly as used in the denominator of the likelihood ratio. We judge the extrapolation to be adequate, remembering that this false-alarm probability is not the false-alarm probability reported at the end of the search, but merely an ingredient in the likelihood-ratio ranking.

An efficiency requires a simulation population. We drew the simulations from a distribution in which our marginalized parameters roughly reflect our priors on

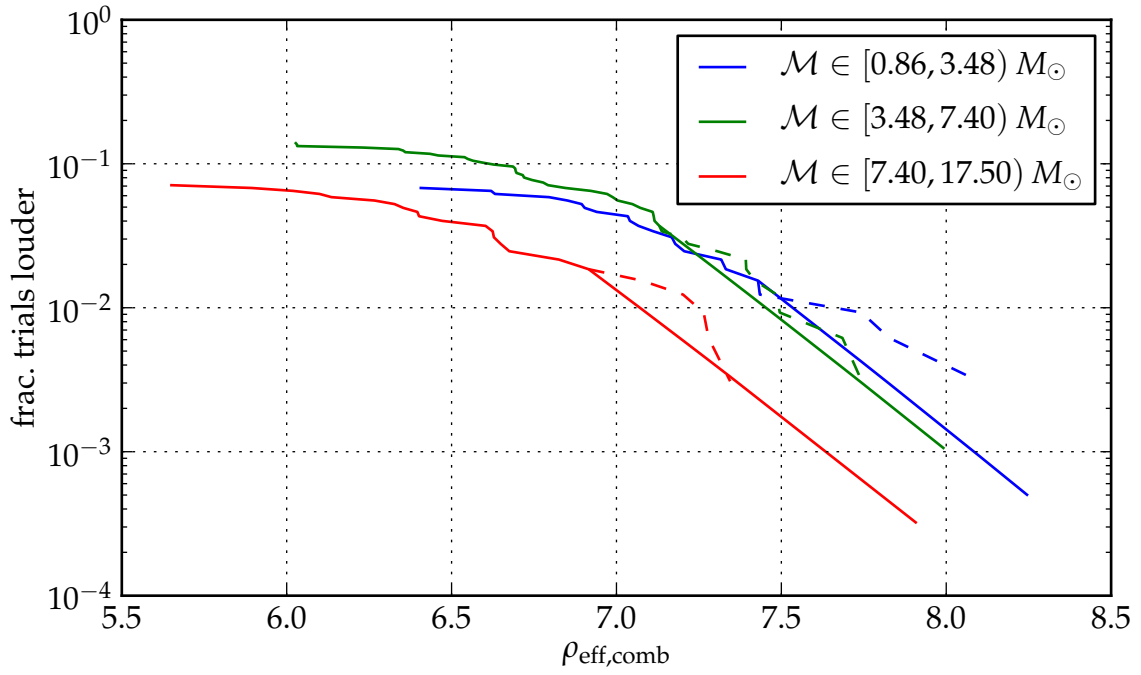


Figure 33 : False-alarm probability versus effective SNR for GRB 070201. The distributions are split by the mean chirp mass of the contributing triggers. The dashed lines indicate the true false-alarm probabilities and the solid lines indicate the used (extrapolated) values.

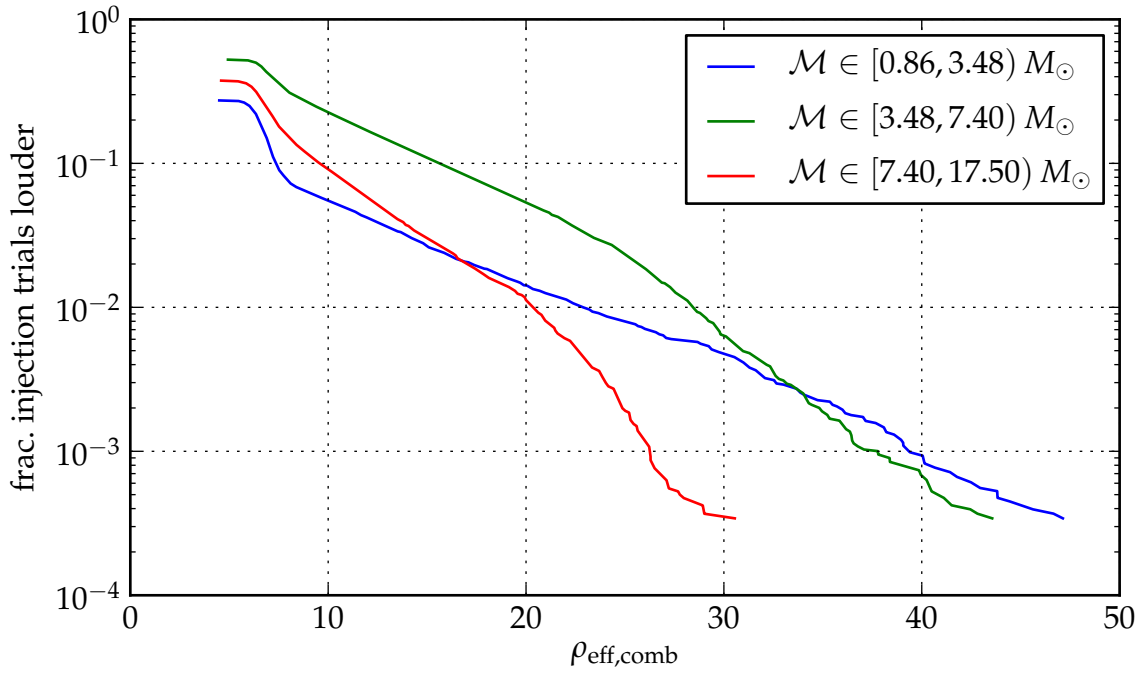


Figure 34 : Efficiency versus effective SNR for GRB 070201. The distributions are split by the mean chirp mass of the contributing triggers.

Parameter name	Symbol	Prior	Unit
NS mass	$m_{\text{NS}}$	$U[1, 3]$	$M_{\odot}$
Inclination angle	$\cos \iota$	$U[-1, 1]$	...
Polarization angle	$\psi$	$U[0, 2\pi]$	rad
Coalescence time	$t_c$	$U[t_{\text{start}}^{\text{off}}, t_{\text{end}}^{\text{off}}]^a$	s
NS spin magnitude	$ \vec{s}_{\text{NS}} $	$U[0, 0.75]^b$	...
Companion spin mag.	$ \vec{s}_{\text{comp}} $	$U[0, 0.98]^b$	...
Spin orientations	$\vec{s}/ \vec{s} $	$U[S^2]^b$	...
Companion mass	$m_{\text{comp}}$	$U[1, 40]$	$M_{\odot}$
Distance	$D$	$U[0.5, 50]^c$	Mpc
Right ascension	$\alpha$	$\alpha_{\text{GRB}} + \text{GMST}(t_c) - \text{GMST}(t_{\text{GRB}})^d$	rad
Declination	$\delta$	$\delta_{\text{GRB}}$	rad

<sup>a</sup> Coalescence time is uniformly distributed over the off-source segment of each GRB.

<sup>b</sup> We injected three waveform families. Two each comprise a quarter of the injections while `SpinTaylorthreePointFivePN` comprises half. The spin distributions are for the latter family, so half of injections are spinless.

<sup>c</sup> The injected waveform amplitudes reflected V3 calibration. Astrophysical statements involving distance incorporate a correction between the V3 and V4 (final) calibration.

<sup>d</sup> Right ascension is varied to keep the simulation at the same antenna factor as the GRB.

Table 2 : Priors and ranges on simulation parameters. The distributions above the line are priors.  $m_{\text{comp}}$  and  $D$  are ranges over which we make astrophysical exclusions, but they are treated as priors in the efficiency assessment of the likelihood ratio statistic.  $\alpha$  and  $\delta$  are completely set by  $t_c$  and the GRB parameters.

these astrophysical compact binary systems. In our models, a signal is completely specified by  $(m_{\text{NS}}, m_{\text{comp}}, \vec{s}_{\text{NS}}, \vec{s}_{\text{comp}}, \iota, \psi, t_c, D, \alpha, \delta)$ . Of these, we wish to constrain  $m_{\text{comp}}$  and  $D$ , and to over everything else. We drew the NS mass  $m_{\text{NS}}$  uniformly from  $[1, 3) M_{\odot}$ ; the magnitudes of the NS spins  $|\vec{s}_{\text{NS}}|$  were half 0 and half uniform in  $[0, 0.75)$  [93]; the magnitudes of the companion spins  $|\vec{s}_{\text{comp}}|$  were half 0 and half uniform in  $[0, 0.98)$  [94]; the orientations of the spins were uniform in solid angle; the inclination  $\iota$  of the normal to the binary's orbital plane relative to our line of sight was conservatively chosen to be uniform in  $\cos \iota$  instead of making an assumption about the GRB beaming angle; the polarization angle  $\phi$  was uniform in  $[0, 2\pi)$ ; the coalescence time  $t_0$  was uniform over the off-source region; the declination  $\delta$  was set to that of the GRB; the right ascension  $\alpha$  was also set to that of the GRB, but was adjusted based on  $t_0$  to keep each simulation at the same location relative to the detector as the GRB. These parameters are summarized in Table 2.

Marginalizing over these priors, we determine the efficiency, which is shown in Fig. 34. Note that the simulations are distributed uniformly in  $D$  rather than  $D^3$ . This is given short discussion in Sec. 4.3.2. The plot demonstrates that different regions of template space do not detect signals with uniform efficiency. Unfortunately, GRB 070201 does not demonstrate the difference in the efficiency of different detector combinations, as only two detectors are used.

Putting the efficiency and false-alarm probability together, we get the likelihood ratio, which is plotted in Fig. 35. There are several noteworthy features:

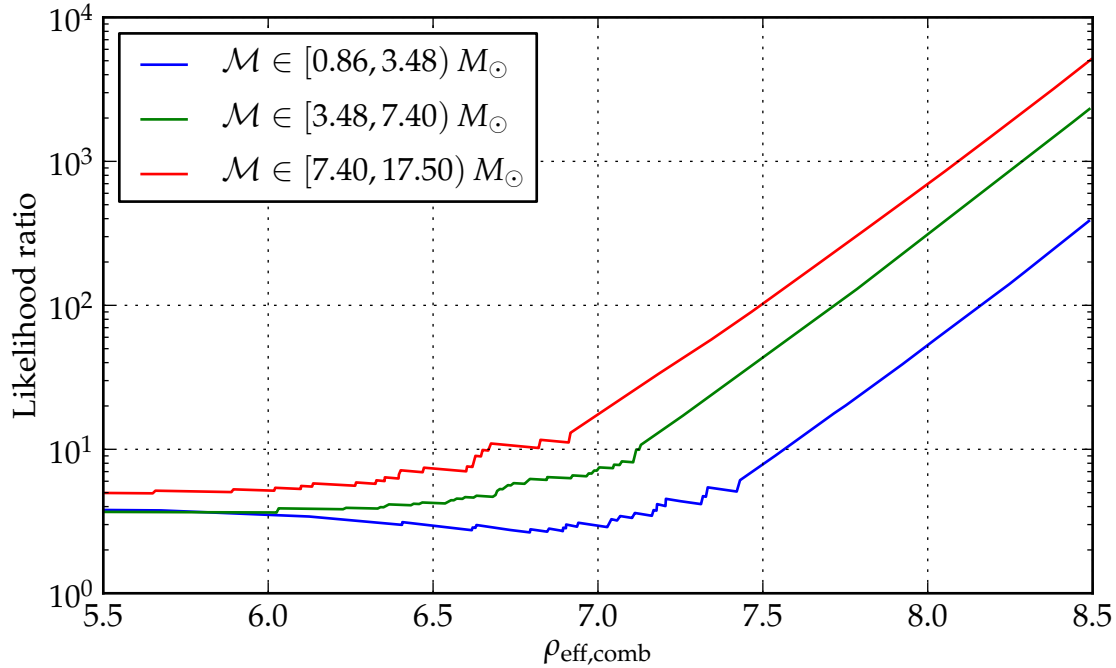


Figure 35 : Likelihood ratio versus effective SNR for GRB 070201. The distributions are split by the mean chirp mass of the contributing triggers.

1. The low-mass region of the template bank yields a likelihood ratio that is non-monotonic with effective SNR. This counterintuitive result means that between  $\rho_{\text{eff,combined}} = 6$  and 7, the efficiency dropped faster than the false-alarm probability. We can see the precipitous drop in Fig. 34. It's possible that  $D^3$  reweighting (see Sec. 4.3.2) would have changed this behavior.
2. In the limit of weak signals, the likelihood ratio does not go to 1. The limit of signal strength approaching zero is background. With PDFs, this would be the ratio of background to background, so should be 1. However, we use the CDF, so the probabilities are cumulative from the right (see Sec. 4.3.2), so this limit is not expected to hold.
3. Proceeding to the right, the likelihood will jump up, then slowly slide down, then jump up, then slowly slide down. This originates in the discreteness of the false-alarm probability estimate. The effect becomes worse at higher  $\rho_{\text{eff,combined}}$  and this drove the choice that the extrapolation point should be set at the 70<sup>th</sup> percentile of  $\rho_{\text{eff,combined}}$ .
4. Again, we only have one detector combination for GRB 070201 (H1–H2), so we cannot see the important reweighting that the likelihood ratio does between different detector combinations.

Applying our likelihood-ratio ranking to all candidates, then maximizing over each trial, we obtain Fig. 36. We again see the same three chirp-mass tracks as in

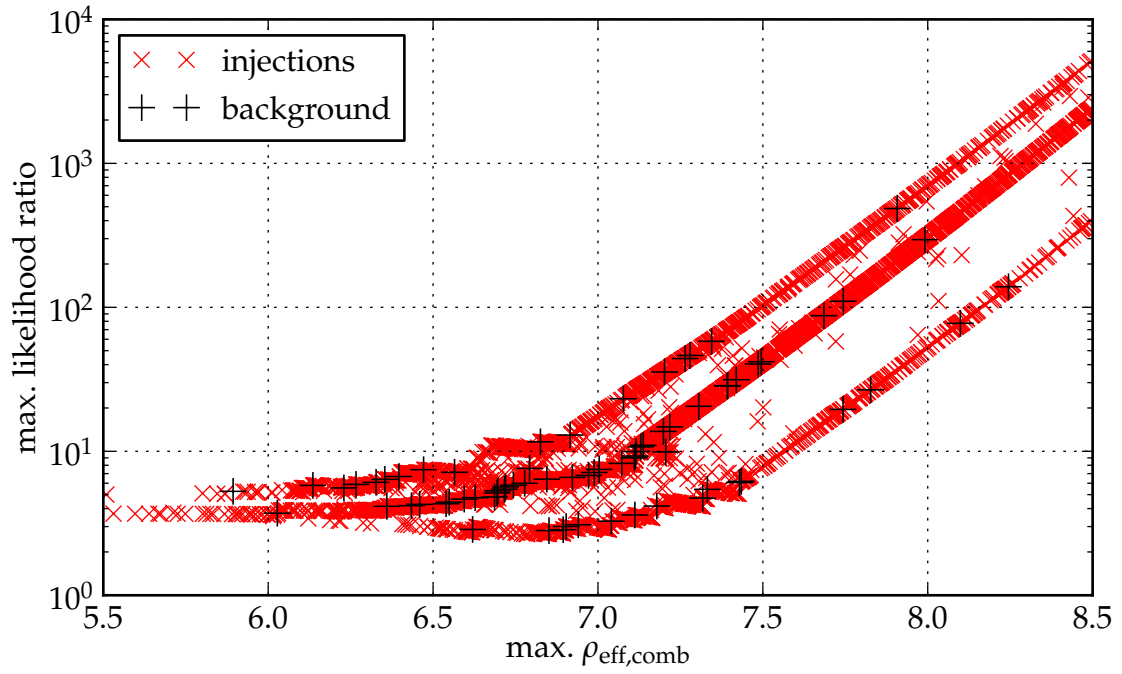


Figure 36 : Maximum likelihood ratio versus maximum effective SNR for GRB 070201. The maximum is over the candidates in a given trial.

Fig. 35, but there are points that do not lie along the tracks. The non-conforming trials are those that yielded a different loudest event when ranked by likelihood ratio versus by effective SNR. These maxima are the quantities that appear in the comparisons below.

The correct apples-to-apples comparison of the efficacy of detection statistics is the receiver operating characteristic (ROC) curve. In an ROC curve, the abscissa specifies a false-alarm probability, which corresponds to a threshold in the ranking statistic. The ordinate specifies the efficiency, the fraction of foreground events with statistic louder than the threshold set by the false-alarm probability. These quantities give a useful measure of effectiveness versus significance, independent of the normalizations of statistics. The only knob to twist is the signal population against which we measure the efficiency, i.e., the parameter space covered by the simulated foreground. The likelihood ratio is the statistic that, by construction, will maximize the ROC curve if it is implemented correctly; our implementation details, described in Sec. 4.3.2, degrade its performance.

Figure 37 contains the ROC curve comparing the likelihood-ratio technique and the simple effective SNR for GRB 070201. Here, we performed the Monte–Carlo integration for efficiency with a  $D^2$  weighting to reflect a prior on  $D$  that is uniform in volume rather than uniform in  $D$ , as we actually drew them. Thus, the ratio of efficiencies is the true ratio of detection rates of these methods. The figure shows some advantage for the likelihood-ratio ranking over the effective SNR at low false-alarm probability (high significance), better by a few percent in absolute terms,

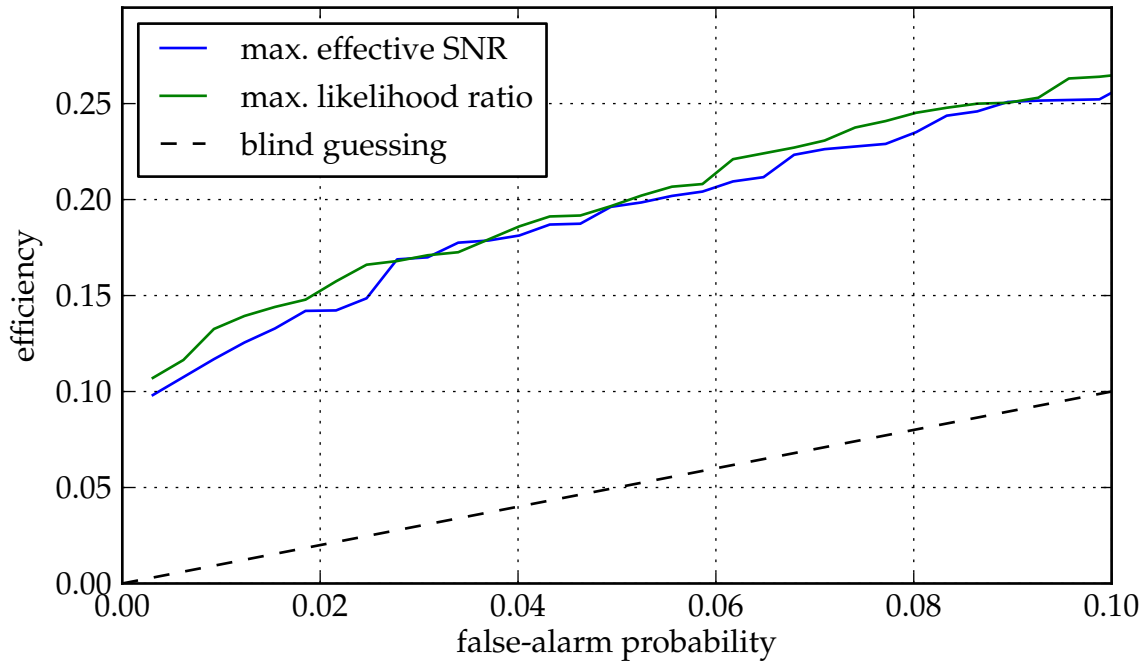
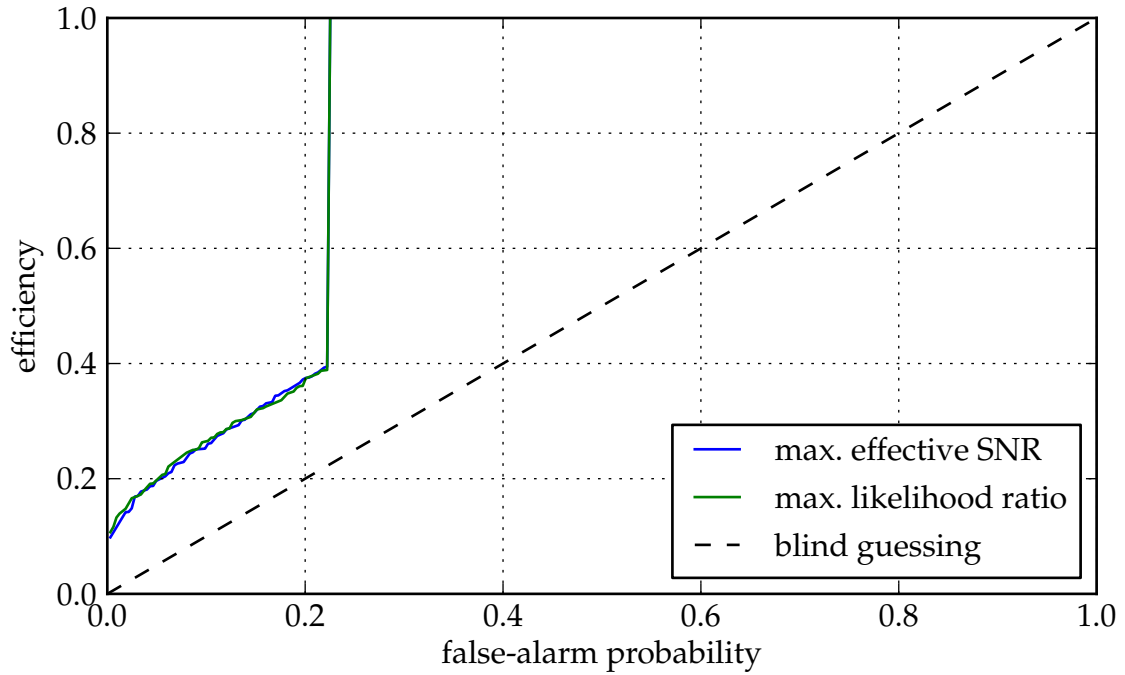


Figure 37 : ROC curve for maximum likelihood versus maximum effective SNR for GRB 070201. The bottom panel shows a zoom of the top panel. The Monte-Carlo integration has been reweighted to reflect a population uniform in volume.

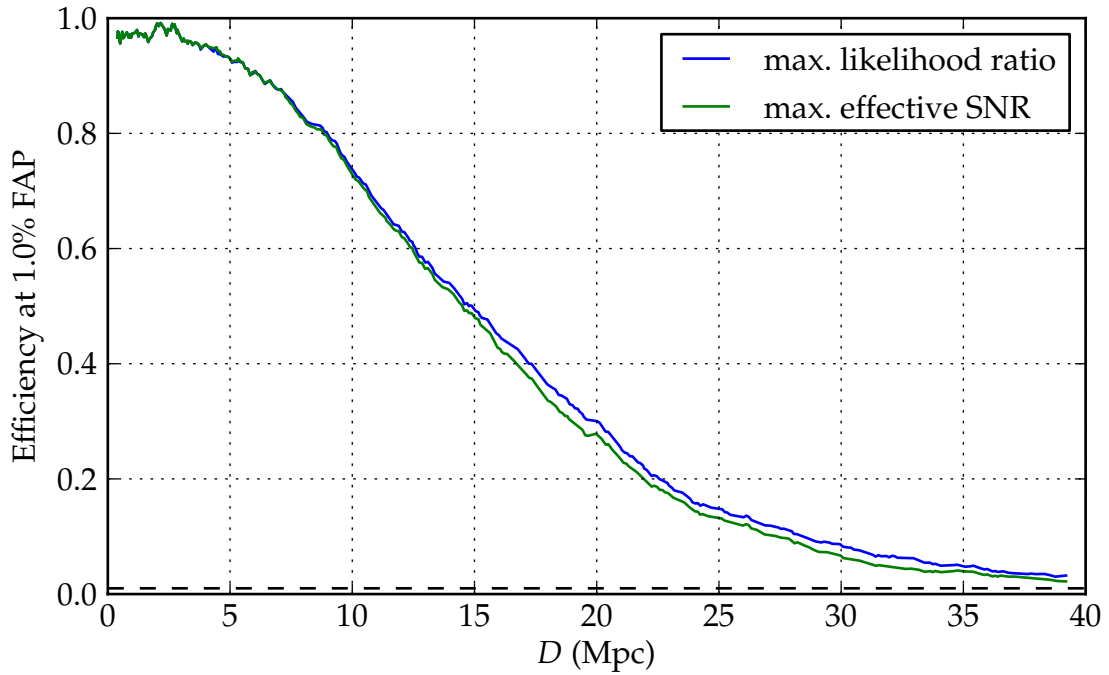


Figure 38 : Efficiency versus distance for GRB 070201. At each distance, efficiency was measured using injections within  $\pm 2$  Mpc, reweighted to be uniform in volume. The threshold was set at 1% false-alarm probability for each ranking statistic. The distances were adjusted for a change in calibration as well as calibration uncertainty as per Sec. 3.5.

$\overline{M}$ bin ( $M_{\odot}$ )	$\rho_{\text{eff,H1}}$	$\rho_{\text{eff,H2}}$	$\rho_{\text{eff,comb}}$	$\overline{M}$ ( $M_{\odot}$ )	Likelihood ratio
[0.86, 3.48)	5.7	3.9	6.9	1.3	3.0
[3.48, 7.40)	5.7	4.3	7.2	4.7	11.7
[7.40, 17.50)	...	...	...	...	...

Table 3 : On-source CBC candidates associated with GRB 070201

but better by tens of percent in relative terms. We can see the effect on sensitivity to systems at various distances in Fig. 38. The likelihood ratio does better near threshold. We might also give the techniques a characteristic sensitivity distance, for example, distance at which we achieve 50% efficiency with a threshold set by 1% false-alarm probability; the distances are 14.5 Mpc for effective SNR and 14.8 Mpc for the likelihood ratio, an improvement of 2% by distance and 6% by volume. The advantage is larger for some data than others. Again, where the data are almost Gaussian, it is difficult to improve upon a simple matched filter.

## 7.4 Significance

Until now, we have examined only off-source and injection trials in tuning the analysis in order to keep the analysis blind. Here we examine the unblinded result. That is, we obtain candidates in the on-source trial, assign the likelihood-ratio ranking to those candidates, and interpret the significance of the loudest event.

Table 3 lists the basic parameters of the loudest on-source candidates in each  $\overline{M}$  bin. As one can see from Fig. 39, the loudest event is insignificant by both likelihood ratio and by effective SNR. Comparing the maximum likelihood ratio

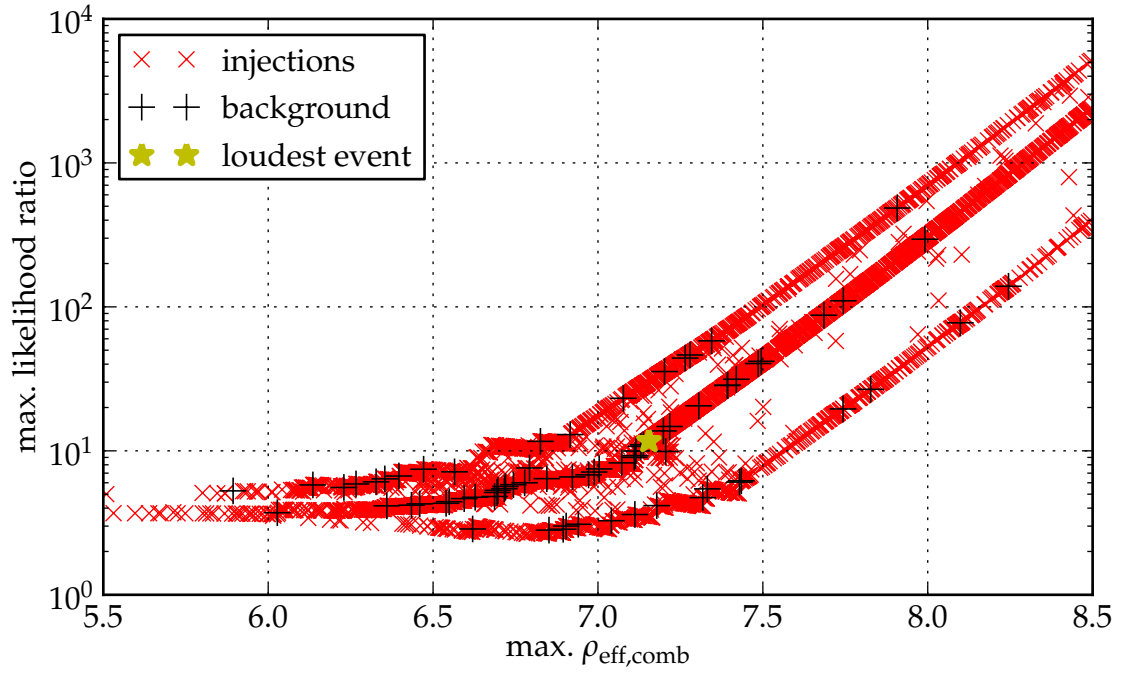


Figure 39 : Maximum likelihood ratio versus maximum effective SNR for GRB 070201 including the on-source trial's loudest event.

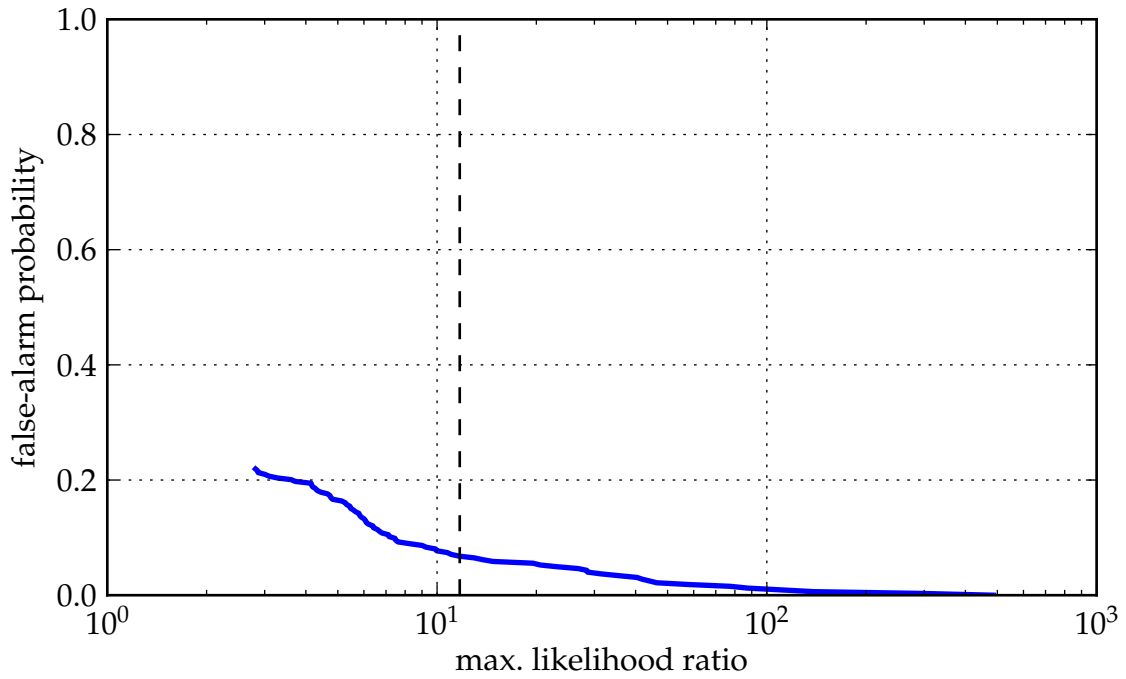


Figure 40 : Significance of the maximum likelihood ratio for GRB 070201. The blue trace is the locus of off-source trials' maximum likelihood ratios and the vertical dashed line represents the on-source trial.

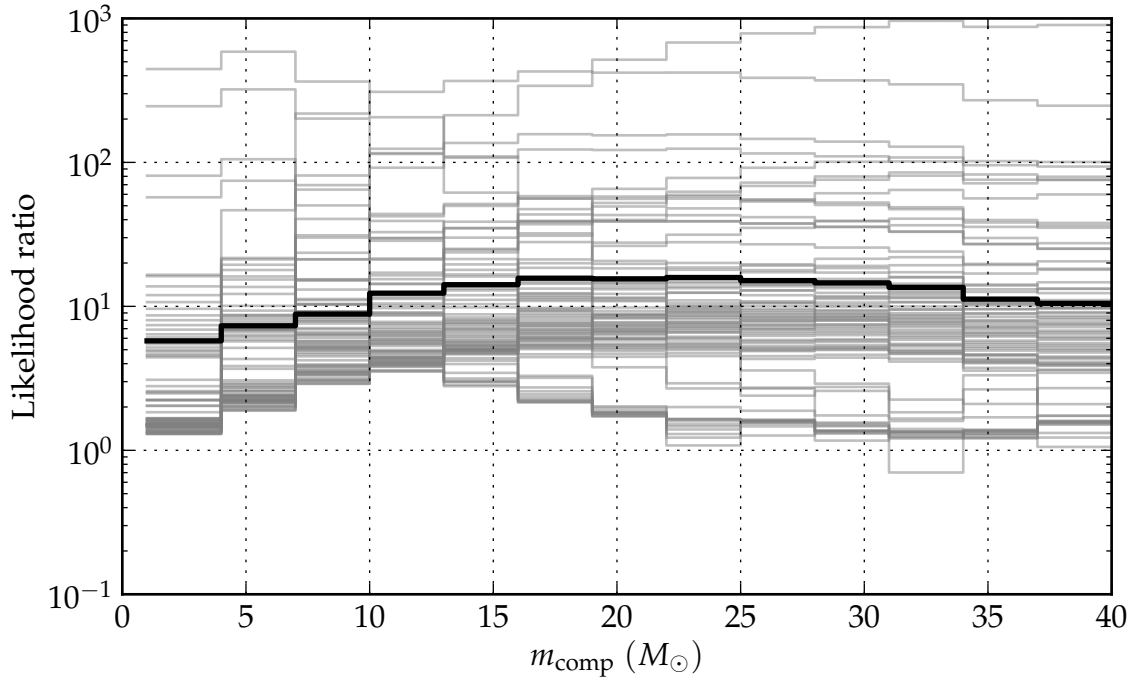


Figure 41 : Maximum likelihood ratios for sub-populations, separated by companion mass, for GRB 070201. Each thin, gray line represents an off-source trial. The thick, black line represents the on-source trial.

more rigorously to off-source values, as shown in Fig. 40, we find a false-alarm probability of 6.8%. This is not a detection.

## 7.5 Distance exclusion

I described the theoretical underpinnings and left some implementation notes for the distance exclusions in Sec. 5.2. In short, we form likelihood ratios for candidates against several distinct subsets of our simulations, separated by the companion mass. For each of these  $m_{\text{comp}}$  bins, we find the loudest candidate and use the Feldman–Cousins (FC) confidence belts to form a confidence interval in  $D$ . The

maximum likelihood ratios in each  $m_{\text{comp}}$  bin for on-source and off-source trials appears in Fig. 41.

For one of these  $m_{\text{comp}}$  bins, let us look closely at the construction of the confidence belts in the FC style. We include a calibration correction factor of 0.273, as per the considerations of Sec. 3.5 and the belts are stretched to cover 1.28 times the Monte–Carlo uncertainty, as explained in Sec. 5.2.4. Figure 42 shows the raw  $p(\Lambda(m_{\text{comp}}) | D)$  distribution and the resulting belts. Each row of pixels sums to 1. Empty trials are put in the lowest  $\Lambda$  bin, which is set by the quietest of the trials’ loudest candidate events in this  $m_{\text{comp}}$  slice. The FC 90% confidence interval is 6.23–39.3 Mpc, where  $50/1.273 = 39.3$  Mpc is the outer edge of the simulated  $D$  range after calibration correction.

We note that the distribution is quite rough and the belts are absurdly wide, as we have approximately 19000 injection trials, split among 13  $m_{\text{comp}}$  bins, 40  $D$  bins for an average of 36 injections per row. We established in Sec. 5.2.4 that with 32 simulations or less per row, we must take the whole row as our confidence belt, leaving no robustness against outliers. Spreading the injections so thinly across parameter space greatly weakens our ability to make astrophysical statements. We cannot increase the number of injections due to computational constraints, but we can employ importance sampling, wherein we put injections where we most believe there to be interesting physics — there is no need to waste injections very far away if our sensitivity for a GRB is low and there is little need to inject higher-mass signals if we do not consider these systems as plausible progenitors. This approach will be

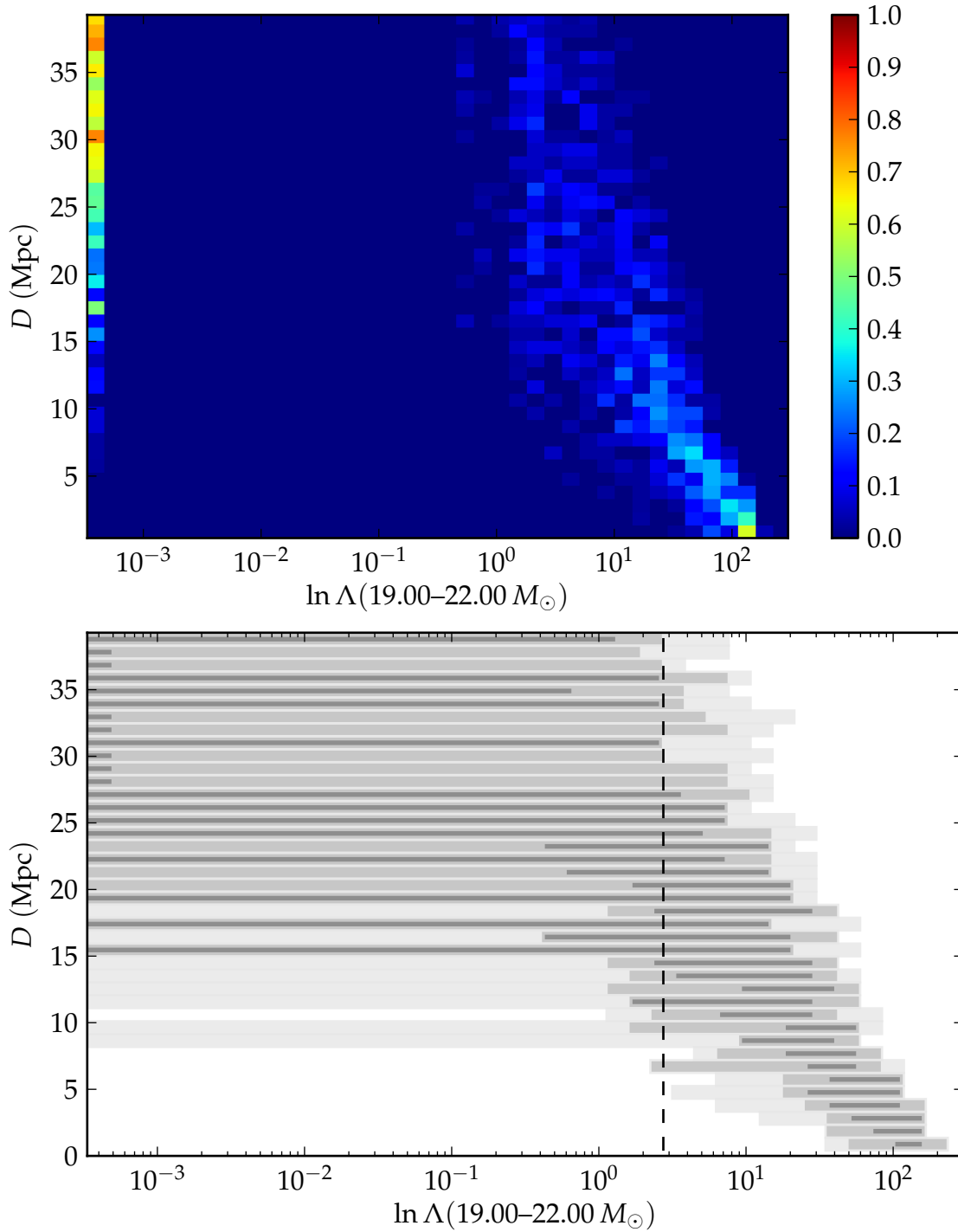


Figure 42 :  $\ln p(\Lambda(m_{\text{comp}}) | D)$  and confidence belts for  $m_{\text{comp}}$  between 19 and 22  $M_{\odot}$  for GRB 070201. This is the raw probability measurement without smoothing or thresholding. The vertical dashed line is the likelihood ratio of our on-source trial's loudest candidate. The shaded regions are, from lightest to darkest, 0.5, 0.75, and 0.9.

used in future analyses.

Figures 43 and 44 show our in-production attempts at mitigating the problems of poor rank estimation in the low  $\Lambda$  gap and the issue of high discreteness from only 36 injections per row on average. Poor rank estimation is overcome slightly in Fig. 43 by the technique of Sec. 5.2.3, removing the gap; that is, putting every trial with non-existent or lower  $\Lambda$  into the  $\ln \Lambda = 1$  ( $\Lambda = e$ ) bin. This essentially makes  $R(\Lambda(m_{\text{comp}}) | D)$  constant across the gap. The FC 90% confidence interval is 6.23–39.3 Mpc. Additionally, Fig. 44 shows the effects of smoothing. The smoothing is a Gaussian kernel in (input)  $D$  that gets wider with increasing (output)  $D$ . The kernel is explicitly

$$K(D_i, D_j) = \exp\left(-\frac{(D_i - D_j)^2}{2\alpha D_j^2}\right) \quad (7.1)$$

$$p_{\text{smoothed}}(\Lambda(m_{\text{comp}}) | D_j) = \sum_i p(\Lambda(m_{\text{comp}}) | D_i) K(D_i, D_j), \quad (7.2)$$

where we have set  $\alpha = 0.025$ , indicating a Gaussian whose standard deviation is growing as  $\sqrt{\alpha}D \approx 16\% \times D$ . Indeed, we observe many fewer outliers among the confidence belts.

With the full thresholding and smoothing apparatus, in our example 19–22  $M_{\odot}$  sub-population, we obtain an FC 90% confidence interval of 5.25–39.3 Mpc. Figure 45 shows the confidence intervals for all sub-populations for GRB 070201. At the end of the search, we report only the lower distances for the two most astrophysically plausible sub-populations, 1–4  $M_{\odot}$  and 7–10  $M_{\odot}$ , roughly corresponding

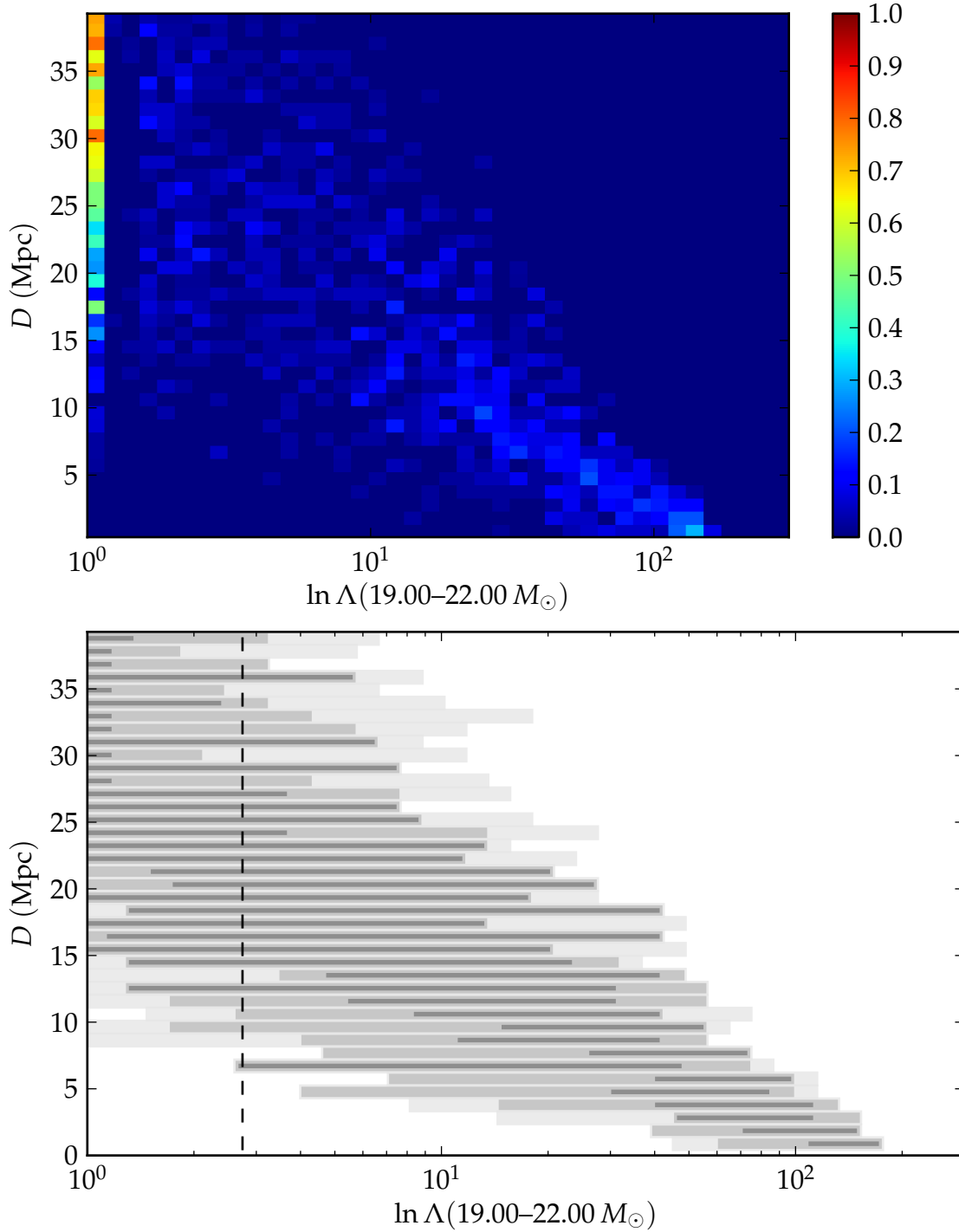


Figure 43 :  $\ln p(\Lambda(m_{\text{comp}}) | D)$  and confidence belts for  $m_{\text{comp}}$  between 19 and 22  $M_{\odot}$  for GRB 070201. These plots introduce thresholding at  $\ln \Lambda = 1$ . The vertical dashed line is the likelihood ratio of our on-source trial's loudest candidate. The shaded regions are, from lightest to darkest, 0.5, 0.75, and 0.9.

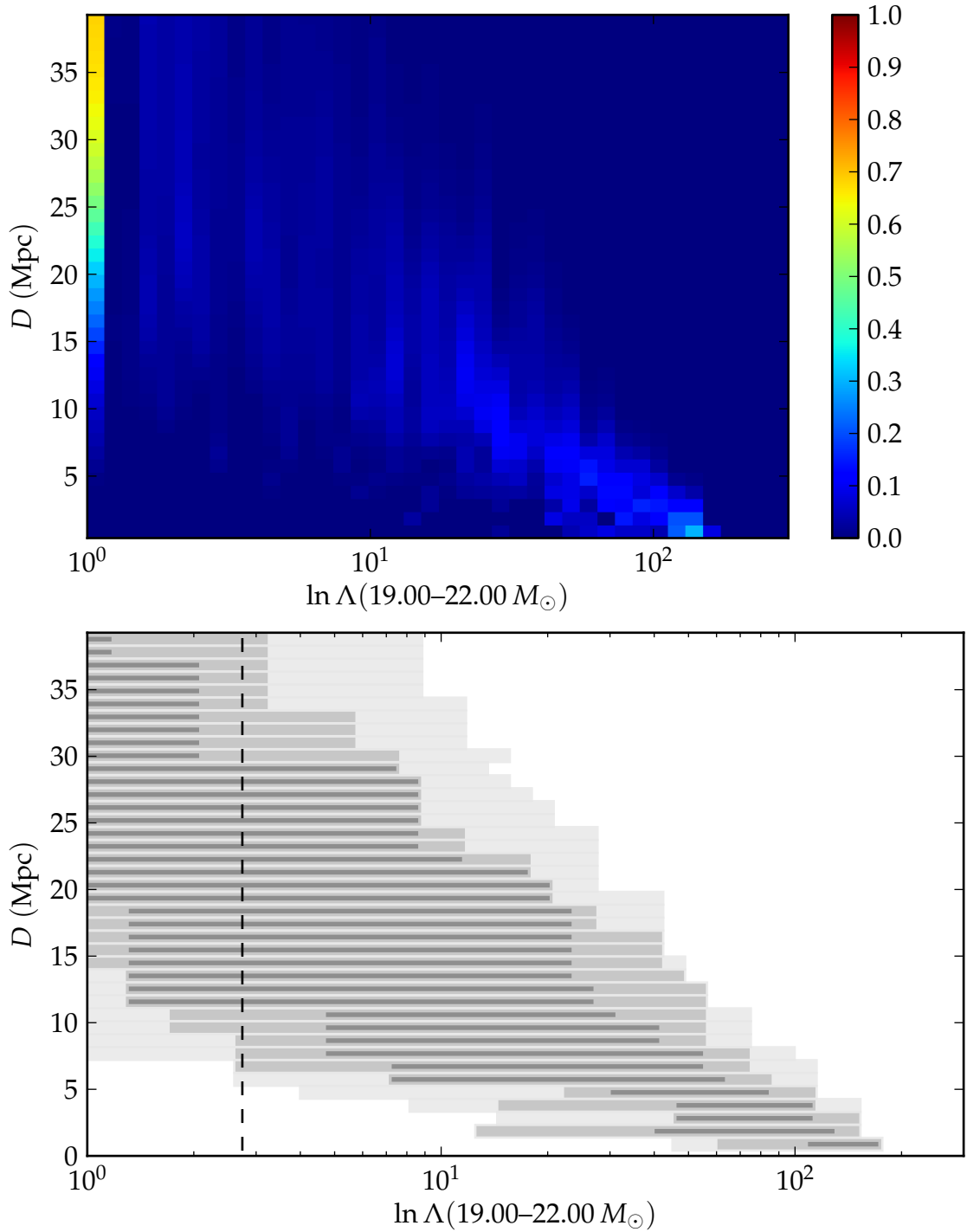


Figure 44 :  $\ln p(\Lambda(m_{\text{comp}}) | D)$  and confidence belts for  $m_{\text{comp}}$  between 19 and 22  $M_{\odot}$  for GRB 070201. These plots introduce thresholding at  $\ln \Lambda = 1$  and additionally Gaussian smoothing that varies with  $D$ . The vertical dashed line is the likelihood ratio of our on-source trial's loudest candidate. The shaded regions are, from lightest to darkest, 0.5, 0.75, and 0.9.

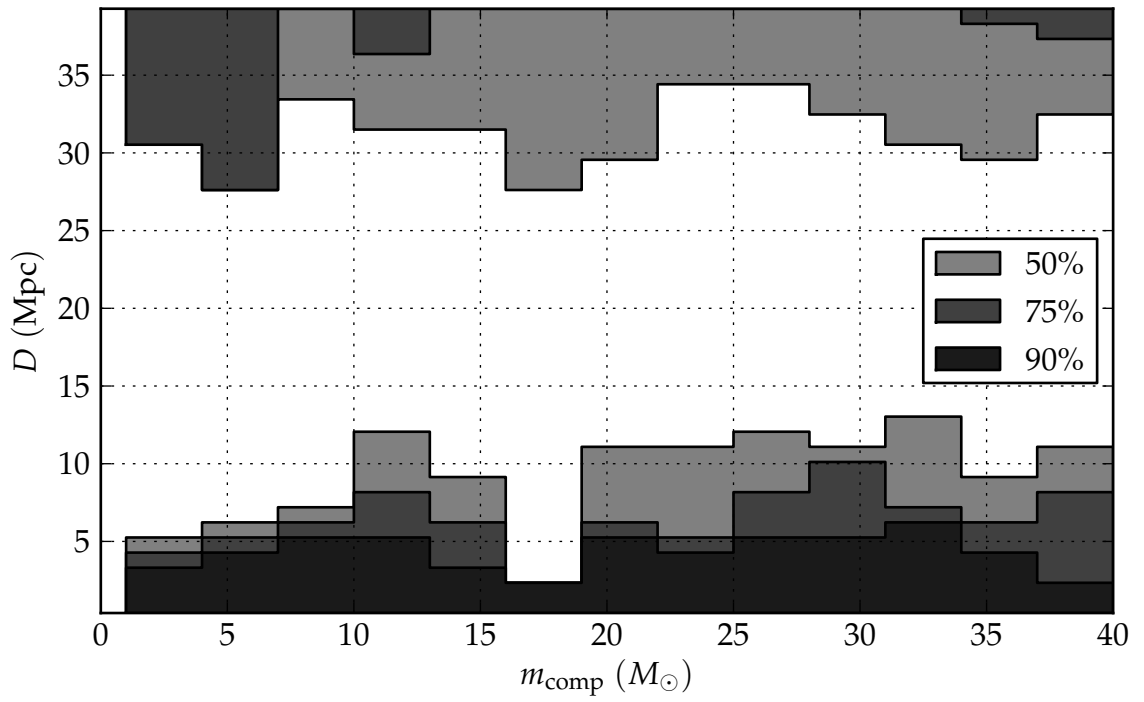


Figure 45 : Feldman–Cousins confidence intervals for all companion-mass sub-populations for GRB 070201

to NS–NS and NS–BH populations, respectively, as in Table 5 and Fig. 46.

## Chapter 8

# The search for CBCs in association with short GRBs in S5/VSR1

In this chapter, I report on a search for gravitational-wave inspiral signals associated with the short GRBs that occurred during S5/VSR1. Details of the science run can be found in Sec. 3.4. The findings of this search were first published in [5], but are reported here again in the context of the detailed explanations of the past chapters. Chapter 6 described the high-level design of the analysis pipeline and Chap. 7 walked through one GRB in great detail; this chapter provides a summary of all GRBs in S5/VSR1.

GRB	Redshift	Duration (s)	References
051114	...	2.2	G4272, G4275
051210	...	1.2	G4315, G4321
051211	...	4.8	G4324, G4359
060121	...	2.0	G4550
060313	< 1.7	0.7	G4867, G4873, G4877
060427B	...	2.0	G5030
060429	...	0.25	G5039
061006	...	0.50	G5699, G5704
061201	...	0.80	G5881, G5882
061217	0.827	0.30	G5926, G5930, G5965
070201	...	0.15	G6088, G6103
070209	...	0.10	G6086
070429B	...	0.50	G6358, G6365
070512	...	2.0	G6408
070707	...	1.1	G6605, G6607
070714	...	2.0	G6622
070714B	0.92	64.0	G6620, G6623, G6836
070724	0.46	0.40	G6654, G6656, G6665
070729	...	0.90	G6678, G6681
070809	...	1.3	G6728, G6732
070810B	...	0.08	G6742, G6753
070923	...	0.05	G6818, G6821

Table 4 : Parameters of the 22 GRBs selected for this search. The values in the references column give the number of the GRB Coordinates Network (GCN) notice from which we took the preceding information [95].

## 8.1 Sample selection

X-ray and gamma-ray instruments identified a total of 212 GRBs during the S5 run: 211 have measured durations; 30 of them have a  $T_{90}$  duration smaller than 2 seconds, where  $T_{90}$  is the time interval over which 90% of all counts from a GRB are recorded. While the  $T_{90}$  classifies a burst as long or short, it is not a definitive discriminator of progenitor systems. In addition to the short GRBs, GRB 051211 [96] and GRB 070714B [97] are formally long GRBs, but they have spectral features hinting at an underlying coalescence progenitor. GRB 061210 is another long-duration burst, but it exhibits the typical short spikes of a short GRB [98]. This gives a list of 33 interesting GRBs with which to search for an association with gravitational waves from compact binary coalescence.

Around the trigger time of each interesting GRB, we required 2190 s of multiply-coincident data. The detectors operated with individual duty cycles of 67–81% over the span of the S5 and VSR1 runs. Where more than two detectors had sufficient data, we selected the most sensitive pair based on the average inspiral range, because including a third, less sensitive detector does not usually enhance the sensitivity greatly. The one exception was GRB 070923, described below. In descending order of sensitivity, the detectors are H1, L1, H2, and V1. This procedure yielded 11 GRBs searched for in H1–L1 coincident data, 9 GRBs in H1–H2, and 1 in H2–L1.

In addition to these 21, we analyze GRB 070923 with V1 because its sky location

relative to the detectors' response functions favors Virgo. The antenna pattern changes with the location of a source relative to a detector and can be expressed by the response (see Eq. (3.13) and Table 4), assuming optimal orientation ( $\iota = 0$ ). A value of 1 corresponds to an optimal location of the putative gravitational-wave source relative to the observatory, while a value of 0 corresponds to a source location that will not induce any strain in the detector. For this particular GRB, the optimal antenna response for Virgo is around 0.7, while those for the two LIGO sites are about half of that (see Table 5), yielding a comparable sensitivity in the direction of GRB 070923 for all three of them. Data from H1, L1, and V1 were analyzed, making this the only GRB involving triple coincidences.

Table 4 lists all 22 target GRBs after applying the selection criteria described in this section. Plausible redshifts have been published for only three of these GRBs, placing them well outside of our detectors' range, but short GRB redshift determinations are in general sufficiently tentative to warrant searching for all of these GRBs.

GRB 070201 is also worth special mention. It was previously analyzed in a high-priority search because of the striking spatial coincidence of this GRB with M31, a galaxy only  $\sim 780$  kpc from Earth (see [99] and Fig. 13). No gravitational-wave signal was found and a coalescence scenario could be ruled out with  $>99\%$  confidence at that distance, lending additional support for a soft gamma repeater hypothesis [100]. However, because of improvements in the analysis pipeline, we re-analyzed this GRB and reported the results in [5] and here. See Chap. 7 for a

complete walkthrough of the new analysis.

## 8.2 Tuning

We generated candidates using the standard, untriggered compact binary coalescence search pipeline described in detail in [75] and summarized in Sec. 6.4. For simplicity, we choose a template bank symmetric in component masses, spanning the range  $[2, 40) M_{\odot}$  in total mass. For the data analyzed in this chapter, the number of templates was around 7000 for each detector.

The SNR threshold for the matched filtering step was chosen differently depending on which detectors' data are available for a given GRB. If data from H1 and L1 were analyzed, the threshold for each detector was set to 4.25, reflecting their comparable sensitivity. If data from H1 and H2 were analyzed, the threshold of the latter detector — the less sensitive of the two — was set to 3.5 to gain maximum network sensitivity, while the threshold of the more sensitive detector, H1, was set to 5.5 since any signal seen in H2 would be twice as loud in H1, with some uncertainty. In the single case of analyzing only H2–L1 data (GRB 070707) the threshold was 4.25 for L1 and 3.5 for H2, and for the single case of analyzing data with Virgo (GRB 070923), the threshold was set to 4.25 for all involved detectors (H1, L1, and V1). For comparison, a uniform SNR threshold of 5.5 was used in the untriggered S5 search (J. Abadie et al., in preparation).

## 8.3 Results

### 8.3.1 Individual GRB results

We found no evidence for a gravitational-wave signal in coincidence with any GRB in our sample. We ran the search as described in the previous section and found that the loudest observed candidates in each GRB's on-source segment is consistent with the expectation from its off-source trials. The results are summarized in Table 5, with brief highlights in the following subsections. A graphical comparison of on-source to off-source false-alarm probability is shown in Fig. 46.

#### GRB 070201

The reanalysis of GRB 070201 yielded candidates in the on-source segment, despite having no coincident candidate at all in the previous analysis [99]. This is consistent because the threshold for H2 has been lowered from 4.0 to 3.5 and the coincident trigger found in this reanalysis happened to lie very close to the larger threshold in the previous search. The reanalysis yields a false-alarm probability of 6.8%, the smallest in the set of analyzed GRBs\*. This value is completely within our expectations when we consider that we examined 22 GRBs.

---

\*In public presentations of preliminary results, GRB 061006 was erroneously highlighted as having the loudest candidate due to a 22.8 s offset in the GRB time. Swift's initial GCN alert [101] was later corrected [102], but we initially overlooked this correction.

GRB	Antenna response				F.A.P.	Excluded distance (Mpc)	
	H1	H2	L1	V1		NS-NS	NS-BH
051114	0.56	0.56	...	...	1	2.3	6.2
051210	0.61	0.61	...	...	0.10	3.3	4.3
051211	0.53	...	0.62	...	0.66	2.3	8.9
060121	0.11	...	0.09	...	0.58	0.4	1.3
060313	0.59	0.59	...	...	0.16	1.4	4.3
060427B	0.91	...	0.92	...	1	7.0	12.7
060429	0.92	0.92	...	...	0.21	4.3	6.2
061006	0.61	0.61	...	...	1	2.3	8.2
061201	0.85	0.85	...	...	1	4.3	10.1
061217	0.77	...	0.52	...	0.23	3.2	11.8
070201	0.43	0.43	...	...	0.07	3.3	5.3
070209	0.19	...	0.12	...	0.76	2.3	4.2
070429B	0.99	...	0.93	...	0.31	8.9	14.6
070512	0.38	...	0.51	...	0.97	6.1	8.9
070707	...	0.87	0.79	...	0.87	4.2	7.1
070714	0.28	...	0.40	...	0.72	4.2	2.3
070714B	0.25	...	0.38	...	0.54	3.2	5.1
070724	0.53	...	0.70	...	0.84	5.1	11.8
070729	0.85	0.85	...	...	0.40	7.0	10.8
070809	0.30	0.30	...	...	1	2.3	4.3
070810B	0.55	...	0.34	...	0.50	2.3	6.1
070923	0.32	...	0.40	0.69	0.74	5.1	7.9

Table 5 : Summary of the results for the search for gravitational waves from each GRB. The Antenna Response column contains the response for each detector as explained in Sec. 8.1; an ellipsis (...) denotes that a detector's data were not used. F.A.P. is the false-alarm probability of the most significant on-source candidate for a GRB as measured against its off-source trials, as explained in Sec. 5.1.1. On-source trials with no candidates above threshold are assigned a F.A.P. of 1. The last two columns show the lower limits at 90% CL on distances, explained in Sec. 8.3.2.

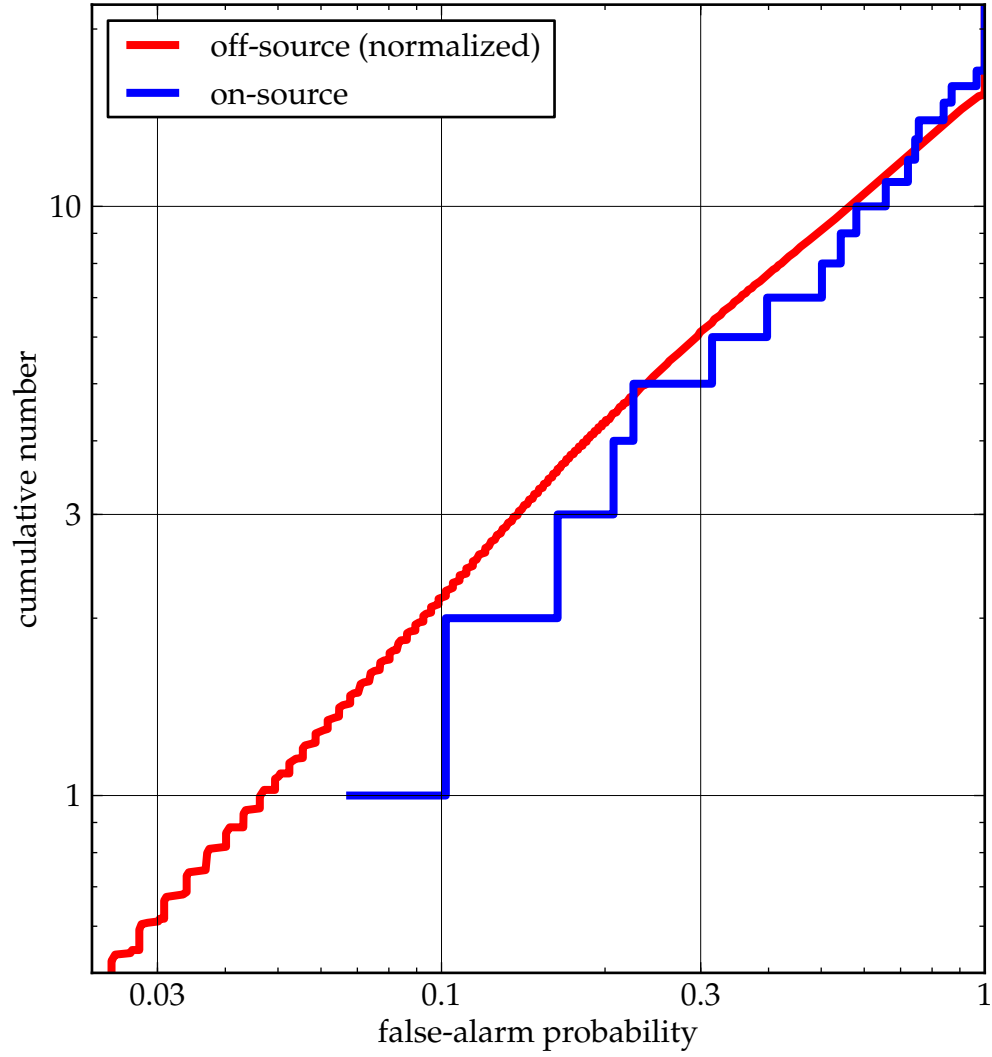


Figure 46 : Cumulative false-alarm probabilities for the most significant candidate in each on- and off-source trial, as described in Sec. 5.1.1.

## GRB 070923

GRB 070923 was the GRB for which H1, L1, and V1 had comparable sensitivity and we accepted triggers from all three detectors. There were no triply-coincident candidates in the on-source trial, but there were surviving doubly-coincident candidates, the loudest of which had a false-alarm probability of 74.5%.

### 8.3.2 Distance exclusions

With our null observations and a large number of simulations, drawn from the distributions of Table 2, we can constrain the distance to each GRB assuming it was caused by a compact binary coalescence with a neutron star (with a mass in the range  $[1, 3) M_{\odot}$ ) and a companion of mass  $m_{\text{comp}}$ . Section 5.2 contains the details. In summary, for a given  $m_{\text{comp}}$  range, we used the approach of Feldman and Cousins [69] to compute regions in distance where gravitational-wave events would, with a given confidence, have produced results inconsistent with our observations. Figure 47 shows the lower Feldman–Cousins distances for the 22 analyzed GRBs at 90% confidence for two illustrative choices for the companion mass range. The values are also listed in Table 5. Because the companion mass range has been divided into equally spaced bins, we report on a ‘NS–NS’ system in which the companion mass is in the range  $[1, 4) M_{\odot}$  and a ‘NS–BH’ system in which the BH has a mass in the range  $[7, 10) M_{\odot}$ . The median exclusion distance for a NS–BH system is 6.7 Mpc and for a NS–NS system is 3.3 Mpc. Note that these distances

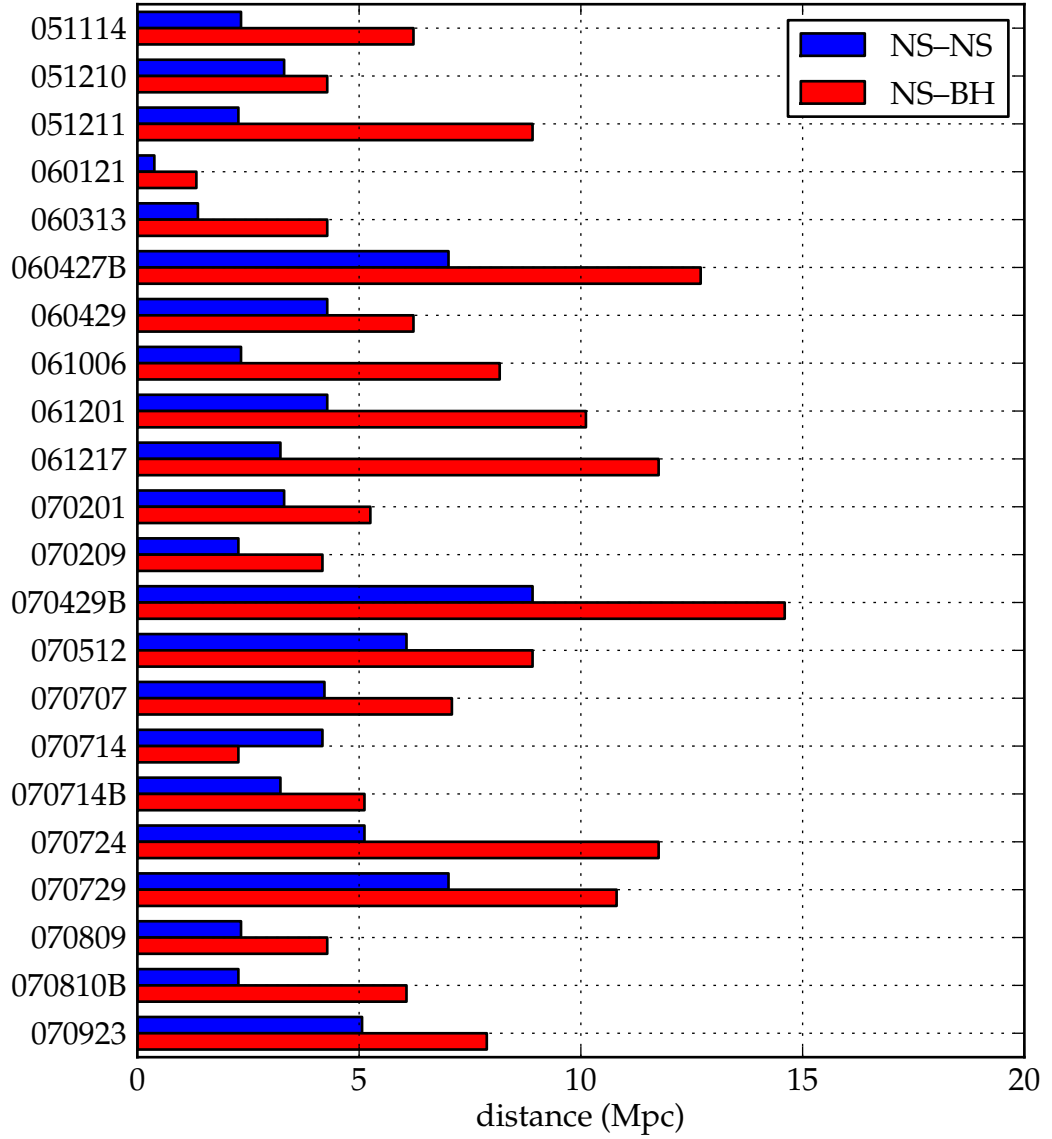


Figure 47 : Lower limits on distances at 90% CL to putative NS-NS and NS-BH progenitor systems, as listed in Table 5 and explained in Sec. 8.3.2.

were derived assuming no beaming (uniform prior on  $\cos \iota$ ). NS–BH distances are typically higher than NS–NS because more massive systems radiate more total gravitational-wave energy. The excluded distance depends on various parameters: the location of the GRB on the sky, the detectors used for the GRB, the noise floor of the data itself, and the likelihood ratio of the loudest on-source candidate event for the GRB.

A number of systematic uncertainties enter into this analysis, but amplitude calibration error and Monte–Carlo counting statistics from the injection trials have the largest effects. We multiplied exclusion distances by  $1.28 \times (1 + \delta_{\text{cal}})$ , where  $\delta_{\text{cal}}$  is the fractional uncertainty. See Sec. 3.5 for discussion of the calibration uncertainty for S5/VSR1. The factor of 1.28 corresponds to a 90% pessimistic fluctuation, assuming Gaussianity. To take the counting statistics into account, we stretched the Feldman–Cousins confidence belts to cover the probability  $\text{CL} + 1.28\sqrt{\text{CL}(1 - \text{CL})/n}$ , where CL is the desired confidence limit and  $n$  is the number of simulations contained in the  $(m_{\text{comp}}, D)$  bin for which we are constructing the belt.

### 8.3.3 Population statement

In addition to the individual detection searches above, we would like to assess the presence of gravitational-wave signals that are too weak to stand out above background separately, but that are significant when the entire population of analyzed GRBs is taken together. We compare the cumulative distribution of the false-alarm

probabilities of the on-source sample with the off-source sample. The on-source sample consist of the results of all 22 individual searches, including those for GRBs with known redshifts, and the off-source sample consists of 6801 results from the off-source trials. This number is lower than  $22 \times 324$ , where 324 is the nominal number of off-source trials for each GRB, because for some GRBs, some off-source trials were discarded due to known data quality issues.

These two distributions are compared in Fig. 46. To determine if they are consistent with being drawn from the same parent distribution, we employ the non-parametric Wilcoxon–Mann–Whitney  $U$  statistic, which is a measure of how different two populations are (see Sec. 5.3 for details). With this size sample, we can assume Gaussianity of the  $U$  statistic to a good approximation; in this approximation,  $\mu_U = 74811$  and  $\sigma_U = 9224$ . Applying the  $U$  test, we find that  $U = 75128.5 = \mu_U - 0.07\sigma$ , suggesting that the two distributions are consistent with each other; if the on-source and off-source significances were drawn from the same distribution, they would yield a  $U$  statistic greater than what we observed 53% of the time. Therefore, we find no evidence for an excess of weak gravitational-wave signals associated with GRBs.

### 8.3.4 Discussion

We searched data taken with the three LIGO detectors and the Virgo detector for gravitational-wave signatures of compact binary coalescences associated with 22 GRBs but found none. We were sensitive to systems with total masses  $2 M_\odot < M <$

$40 M_{\odot}$ . We also searched for a population of signals too weak to be individually detected, but again found no evidence. While there are few redshift determinations for short GRBs, it appears that the distribution is peaked around  $\langle z \rangle \sim 0.25$  [21], far outside of initial detector sensitivity, so it is not surprising that the S5/VSR1 run yielded no detections associated with short GRBs.

A related search in the same LIGO/Virgo data set was performed in [103], looking for short-duration gravitational-wave bursts in association with 137 GRBs recorded during S5/VSR1, both long and short. The analysis reported upper limits on the strain of a generic burst of circularly polarized gravitational radiation, predominantly at the detectors' most sensitive frequencies. These were translated into lower limits in distance by assuming that  $0.01 M_{\odot}$  is converted into isotropically emitted gravitational waves. In contrast, the search described here does not make any assumption on the polarization of the gravitational waves and searches for the specific signals expected from binary coalescences. Importantly, the present search can distinguish a coalescence signal from other models and estimate the progenitor parameters.

## Chapter 9

### Epilogue

Looking back, this thesis has provided a concrete workflow for searching for compact binary coalescence counterparts to short gamma-ray bursts. We executed the pipeline on S5/VSR1 LIGO/Virgo data, finding no serious candidates. We used the null results to constrain the distance to the progenitors, assuming that they were each compact binaries.

Astronomers have acknowledged LIGO's first, small contributions to the GRB mystery, providing additional evidence that GRB 070201 was a soft gamma repeater [100]. In the Astro2010 decadal survey, in which the astronomical community decides the priorities of the coming decade, ground-based gravitational-wave detectors figured prominently [1, 2, 3, 4]. The Enhanced and Advanced configurations of LIGO and Virgo hold great promise for detection [104]. The science run S6/VSR2 is currently underway with improved sensitivity over S5/VSR1. In 2014, Advanced LIGO should operate with 10 times the initial sensitivity, or 1000 times the event

rate. We will have the sensitivity to realize our science goals.

The LIGO Scientific Collaboration and the Virgo Collaboration are now wrestling with the data analysis requirements in the Advanced detector era; our current searches are clumsy, first prototypes. Our analysis strategy will need to shift from analyzing a large block of data at a time to a streaming mode, where data are incorporated incrementally. We will need to integrate the current LIGO/Virgo transient searches more tightly with other electromagnetic transient searches including the Palomar Transient Factory and ROTSE. There are collaborations forming to search for non-electromagnetic triggers such as ultra-high energy cosmic rays from Auger or neutrinos from IceCube. We have begun to send triggers the opposite direction, as well, launching rapid, automated, wide-field followup with robotic telescopes with fast pointing capabilities such as *Swift*, ROTSE, and QUEST, with other optical and radio telescopes under consideration. The likelihood ratio methods of Chap. 4 show the greatest promise of integrating evidence from all sides into coherent statements about the universe. There is a lot of work ahead, but the payoff will be great.

# Bibliography

- [1] Joshua S. Bloom et al. Astro2010 decadal survey whitepaper: Coordinated science in the gravitational and electromagnetic skies, 2009. (Cited on pages 2 and 142.)
  
- [2] E. S. Phinney. Finding and Using Electromagnetic Counterparts of Gravitational Wave Sources, 2009. (Cited on pages 2 and 142.)
  
- [3] T. A. Prince and for the LISA International Science Team. The Promise of Low-Frequency Gravitational Wave Astronomy, 2009. (Cited on pages 2 and 142.)
  
- [4] Benjamin J. Owen. Probing neutron stars with gravitational waves, 2009. (Cited on pages 2 and 142.)
  
- [5] J Abadie et al. Search for gravitational-wave inspiral signals associated with short Gamma-Ray Bursts during LIGO's fifth and Virgo's first science run, January 2010. arXiv:1001.0165. (Cited on pages 2, 129, and 132.)

- [6] Ray W. Klebesadel, Ian B. Strong, and Roy A. Olson. Observations of Gamma-Ray Bursts of Cosmic Origin. *ApJ*, 182:L85, 1973. (Cited on page 3.)
- [7] P Mészáros. Gamma ray bursts. *Rep. Prog. Phys.*, 69:2259–2321, 2006. (Cited on pages 3 and 8.)
- [8] K. Hurley, T. Cline, I. G. Mitrofanov, D. Golovin, M. L. Litvak, A. B. Sanin, W. Boynton, C. Fellows, K. Harshman, R. Starr, S. Golenetskii, R. Aptekar, E. Mazets, V. Pal'shin, D. Frederiks, D. M. Smith, C. Wigger, W. Hajdas, A. Zehnder, A. von Kienlin, G. G. Lichti, A. Rau, K. Yamaoka, M. Ohno, Y. Fukazawa, T. Takahashi, M. Tashiro, Y. Terada, T. Murakami, K. Makishima, S. Barthelmy, J. Cummings, N. Gehrels, H. Krimm, J. Goldsten, E. Del Monte, M. Feroci, and M. Marisaldi. The status and future of the third interplanetary network. In Charles Meegan, Chryssa Kouveliotou, and Neil Gehrels, editors, *GAMMA-RAY BURST: Sixth Huntsville Symposium*, volume 1133, pages 55–57. AIP, 2009. (Cited on page 3.)
- [9] G. R. Ricker, J.-L. Atteia, G. B. Crew, J. P. Doty, E. E. Fenimore, M. Galassi, C. Graziani, K. Hurley, J. G. Jernigan, N. Kawai, D. Q. Lamb, M. Matsuoka, G. Pizzichini, Y. Shirasaki, T. Tamagawa, R. Vanderspek, G. Vedrenne, J. Villasenor, S. E. Woosley, and A. Yoshida. The High Energy Transient Explorer (HETE): Mission and Science Overview. In G. R. Ricker & R. K. Vanderspek, editor, *Gamma-Ray Burst and Afterglow Astronomy 2001: A Workshop Celebrating*

*the First Year of the HETE Mission*, volume 662 of *American Institute of Physics Conference Series*, pages 3–16, April 2003. (Cited on page 3.)

- [10] N. Gehrels et al. The Swift Gamma-Ray Burst Mission. *AIP Conf. Proc.*, 727:637–641, 2004. (Cited on page 3.)
- [11] R. L. Aptekar, D. D. Frederiks, S. V. Golenetskii, V. N. Il'ynskii, E. P. Mazets, V. N. Panov, Z. J. Sokolova, M. M. Terekhov, L. O. Sheshin, T. L. Cline, and D. E. Stilwell. Konus-W Gamma-Ray Burst Experiment for the GGS Wind Spacecraft. *Space Science Reviews*, 71:265–272, February 1995. (Cited on page 3.)
- [12] C. Winkler, T. J.-L. Courvoisier, G. Di Cocco, N. Gehrels, A. Giménez, S. Grebenev, W. Hermsen, J. M. Mas-Hesse, F. Lebrun, N. Lund, G. G. C. Palumbo, J. Paul, J.-P. Roques, H. Schnopper, V. Schönfelder, R. Sunyaev, B. Teegarden, P. Ubertini, G. Vedrenne, and A. J. Dean. The INTEGRAL mission. *A&A*, 411:L1–L6, November 2003. (Cited on page 3.)
- [13] W. B. Atwood et al. The Large Area Telescope on the Fermi Gamma-ray Space Telescope Mission. *ApJ*, 697:1071–1102, 2009. (Cited on page 3.)
- [14] C Kouveliotou et al. Identification of two classes of gamma-ray bursts. *ApJ*, 413:L101–104, 1993. (Cited on page 4.)
- [15] N Gehrels et al. Swift detects a remarkable gamma-ray burst, GRB 060614, that introduces a new classification scheme. *Nature*, 444:1044, 2006. (Cited on page 4.)

- [16] S. Campana et al. The shock break-out of GRB 060218/SN 2006aj. *Nature*, 442:1008–1010, 2006. (Cited on page 4.)
- [17] T. J. Galama et al. Discovery of the peculiar supernova 1998bw in the error box of GRB980425. *Nature*, 395:670, 1998. (Cited on page 4.)
- [18] Jens Hjorth et al. A very energetic supernova associated with the gamma-ray burst of 29 March 2003. *Nature.*, 423:847–850, 2003. (Cited on page 4.)
- [19] D. Malesani et al. SN 2003lw and GRB 031203: A Bright Supernova for a Faint Gamma-ray Burst. *ApJ*, 609:L5, 2004. (Cited on page 4.)
- [20] Jochen Greiner. GRBs localized with BSAX or BATSE/RXTE or ASM/RXTE or IPN or HETE or INTEGRAL or Swift or AGILE or Fermi/GLAST, 2009. <http://www.mpe.mpg.de/~jcg/grbgen.html>. (Cited on page 4.)
- [21] Ehud Nakar. Short-hard gamma-ray bursts. *Phys. Rep.*, 442:166–236, 2007. (Cited on pages 4, 5, 8, 9, and 141.)
- [22] Bing Zhang et al. Making a Short Gamma-Ray Burst from a Long one: Implications for the Nature of GRB 060614. *ApJL*, 655:L25–L28, 2007. (Cited on page 5.)
- [23] Joshua S. Bloom, Nathaniel R. Butler, and Daniel A. Perley. Gamma-ray bursts, classified physically. In M. Galassi, David Palmer, and Ed Fenimore, editors, *Gamma Ray Bursts*, volume 1000, pages 11–15. AIP, 2008. (Cited on page 5.)

- [24] Ehud Nakar, Avishay Gal-Yam, and Derek B. Fox. The Local Rate and the Progenitor Lifetimes of Short-Hard Gamma-Ray Bursts: Synthesis and Predictions for LIGO. *ApJ*, 650:281, 2006. (Cited on page 5.)
- [25] R. Chapman, R. S. Priddey, and N. R. Tanvir. Short gamma-ray bursts from SGR giant flares and neutron star mergers: two populations are better than one. *MNRAS*, 395:1515–1522, May 2009. (Cited on page 5.)
- [26] Kevin Hurley et al. A tremendous flare from SGR1806-20 with implications for short-duration gamma-ray bursts. *Nature*, 434:1098–1103, 2005. (Cited on page 5.)
- [27] David M. Palmer et al. Gamma-Ray Observations of a Giant Flare from The Magnetar SGR 1806-20. *Nature*, 434:1107–1109, 2005. (Cited on page 5.)
- [28] Lorenzo Amati. The  $E_{p,i}$  - Eiso correlation in GRBs: updated observational status, re-analysis and main implications. *MNRAS*, 372:233–245, 2006. (Cited on page 5.)
- [29] Kevin Hurley. The Status and Future of the 3rd Interplanetary Network, 2009. Poster at The Shocking Universe, San Servolo Island, Italy. (Cited on page 7.)
- [30] M B Davies, A J Levan, and A R King. The ultimate outcome of black hole - neutron star mergers. *Mon. Not. R Astron. Soc.*, 356:54–59, 2005. (Cited on page 8.)

- [31] M. Shibata and K. Taniguchi. Merger of black hole and neutron star in general relativity: Tidal disruption, torus mass, and gravitational waves. *Phys. Rev. D*, 77(8):084015–+, April 2008. (Cited on page 8.)
- [32] Joshua A. Faber, Thomas W. Baumgarte, Stuart L. Shapiro, Keisuke Taniguchi, and Frederic A. Rasio. Black Hole-Neutron Star Binary Merger Calculations: GRB Progenitors and the Stability of Mass Transfer. *AIP Conf. Proc.*, 861:622–629, 2006. (Cited on page 8.)
- [33] Stephan Rosswog. Last moments in the life of a compact binary system: gravitational waves, gamma-ray bursts and magnetar formation. *Revista Mexicana de Astronomía y Astrofísica*, 027:57–79, 2006. (Cited on page 8.)
- [34] Zachariah B. Etienne et al. Fully General Relativistic Simulations of Black Hole- Neutron Star Mergers. *Phys. Rev. D*, 77:084002, 2008. (Cited on page 8.)
- [35] J. A. Wheeler. *A journey into gravity and spacetime*. W. H. Freeman & Company, 1990. (Cited on page 10.)
- [36] K. S. Thorne. Multipole expansions of gravitational radiation. *Reviews of Modern Physics*, 52:299–340, April 1980. (Cited on page 16.)
- [37] David W. Hogg. Distance measures in cosmology, 1999. (Cited on page 19.)
- [38] K S Thorne. Gravitational radiation. In S. W. Hawking and W. Israel, editors, *Three hundred years of gravitation*, chapter 9, pages 330–458. Cambridge University Press, Cambridge, 1987. (Cited on page 19.)

- [39] C Cutler and E Flanagan. Gravitational waves from merging compact binaries: How accurately can one extract the binary's parameters from the inspiral waveform? *Phys. Rev. D*, 49:2658, 1994. (Cited on page 19.)
- [40] L. S. Finn and D. F. Chernoff. Observing binary inspiral in gravitational radiation: One interferometer. *Phys. Rev. D*, 47:2198–2219, March 1993. (Cited on page 19.)
- [41] Eric Poisson and Clifford M. Will. Gravitational waves from inspiraling compact binaries: Parameter estimation using second postNewtonian wave forms. *Phys. Rev. D*, 52:848–855, 1995. (Cited on page 19.)
- [42] Éanna É. Flanagan and Tanja Hinderer. Constraining neutron-star tidal love numbers with gravitational-wave detectors. *Phys. Rev. D*, 77(2):021502, 2008. (Cited on page 19.)
- [43] J. S. Read, C. Markakis, M. Shibata, K. Uryū, J. D. E. Creighton, and J. L. Friedman. Measuring the neutron star equation of state with gravitational wave observations. *Phys. Rev. D*, 79(12):124033–+, June 2009. (Cited on pages 19 and 20.)
- [44] Clifford M. Will. The confrontation between general relativity and experiment. *Living Rev. Rel.*, 9:3, 2005. (Cited on page 19.)

- [45] Samaya Nissanke, Scott A. Hughes, Daniel E. Holz, Neal Dalal, and Jonathan L. Sievers. Exploring short gamma-ray bursts as gravitational-wave standard sirens, 2009. (Cited on pages 19 and 21.)
- [46] Jocelyn S. Read, Benjamin D. Lackey, Benjamin J. Owen, and John L. Friedman. Constraints on a phenomenologically parameterized neutron- star equation of state. *Phys. Rev. D*, 79:124032, 2009. (Cited on page 20.)
- [47] E. Komatsu et al. Five-Year Wilkinson Microwave Anisotropy Probe (WMAP) Observations: Cosmological Interpretation. *ApJS*, 180:330–376, 2009. (Cited on page 20.)
- [48] Daniel J. Eisenstein et al. Detection of the Baryon Acoustic Peak in the Large-Scale Correlation Function of SDSS Luminous Red Galaxies. *ApJ*, 633:560–574, 2005. (Cited on page 20.)
- [49] W. L. Freedman et al. Final Results from the Hubble Space Telescope Key Project to Measure the Hubble Constant. *ApJ*, 553:47–72, 2001. (Cited on page 20.)
- [50] B. Abbott et al. LIGO: The Laser Interferometer Gravitational-Wave Observatory. *Rept. Prog. Phys.*, 72:076901, 2009. (Cited on pages 22, 30, 34, and 35.)
- [51] F. Acernese et al. Status of Virgo. *Class. Quant. Grav.*, 25(11):114045–+, June 2008. (Cited on pages 22 and 30.)

- [52] H. Grote and the LIGO Scientific Collaboration. The status of GEO 600. *Classical and Quantum Gravity*, 25(11):114043–+, June 2008. (Cited on page 22.)
- [53] R. Savage, P. King, and S. Seel. A highly stabilized 10-watt Nd:YAG laser for the laser interferometer gravitational-wave observatory (LIGO). *Laser Physics*, 8:679, 1998. (Cited on pages 25 and 30.)
- [54] Lee Samuel Finn. Response of interferometric gravitational wave detectors. *Phys. Rev. D*, 79(2):022002, Jan 2009. (Cited on page 28.)
- [55] Neil J. Cornish. Alternative derivation of the response of interferometric gravitational wave detectors. *Phys. Rev.*, D80:087101, 2009. (Cited on page 28.)
- [56] Duncan A Brown. *Search for gravitational radiation from black hole MACHOs in the Galactic halo*. PhD thesis, University of Wisconsin–Milwaukee, 2004. (Cited on pages 29, 49, and 72.)
- [57] Peter Fritschel, Rolf Bork, Gabriela González, Nergis Mavalvala, Dale Ouimette, Haisheng Rong, Daniel Sigg, and Michael Zucker. Readout and control of a power-recycled interferometric gravitational-wave antenna. *Appl. Opt.*, 40(28):4988–4998, 2001. (Cited on page 30.)
- [58] Rana Adhikari. *Sensitivity and Noise Analysis of 4 km Laser Interferometric Gravitational Wave Antennae*. PhD thesis, MIT, Cambridge, MA, 2004. (Cited on pages 31 and 36.)

- [59] J. Giaime, P. Saha, D. Shoemaker, and L. Sievers. A passive vibration isolation stack for LIGO: design, modeling, and testing. *Rev. Sci. Instrum.*, 67:208, 1996. (Cited on page 31.)
- [60] C Hardham, B Abbott, R Abbott, G Allen, R Bork, C Campbell, K Carter, D Coyne, D DeBra, T Evans, J Faludi, A Ganguli, J Giaime, M Hammond, W Hua, J Kern, J LaCour, B Lantz, M Macinnis, K Mailand, K Mason, R Mittleman, J Nichol, J Niekerk, B O'Reilly, D Ottaway, H Overmier, C Parameswariah, J Phinney, B Rankin, N A Robertson, D Sellers, P Sarin, D H Shoemaker, O Spjeld, G Traylor, S Wen, R Wooley, and M Zucker. Quiet Hydraulic Actuators for LIGO, 2006. LIGO Document Number P060028-00-Z. (Cited on page 31.)
- [61] A. Gillespie and Frederick J. Raab. Thermal noise in the test mass suspensions of a laser interferometer gravitational wave detector prototype. *Phys. Lett. A*, 178:357–363, 1993. (Cited on page 31.)
- [62] Gregory M. Harry, Helena Armandula, Eric Black, D. R. M. Crooks, Gianpietro Cagnoli, Jim Hough, Peter Murray, Stuart Reid, Sheila Rowan, Peter Sneddon, Martin M. Fejer, Roger Route, and Steven D. Penn. Thermal noise from optical coatings in gravitational wave detectors. *Appl. Opt.*, 45(7):1569–1574, 2006. (Cited on page 32.)
- [63] Eanna Flanagan and Kip Thorne. Noise due to backscatter off baffles, the

- nearby wall, and objects at the far end of the beam tube; and recommended actions, 1994. LIGO Technical Report LIGO-T940063-00-R. (Cited on page 32.)
- [64] R. Bork, R. Abbott, D. Barker, and J. Heefner. An overview of the LIGO control and data acquisition system, 2001. (Cited on page 33.)
- [65] Stephen Fairhurst. Triangulation of gravitational wave sources with a network of detectors. *New J. Phys.*, 11:123006, 2009. (Cited on page 37.)
- [66] Frederique Marion, Benoit Mours, and Loic Rolland.  $h(t)$  reconstruction for vsr1; version 2 and 3. Technical Report VIR-078A-08, Virgo Project, 2008. (Cited on page 40.)
- [67] L A Wainstein and V D Zubakov. *Extraction of signals from noise*. Prentice-Hall, Englewood Cliffs, NJ, 1962. (Cited on page 41.)
- [68] L Blackburn et al. The LSC Glitch Group : Monitoring Noise Transients during the fifth LIGO Science Run. *Class. Quant. Grav.*, 25:184004, 2008. (Cited on page 50.)
- [69] Gary J. Feldman and Robert D. Cousins. A unified approach to the classical statistical analysis of small signals. *Phys. Rev. D*, 57:3873–3889, 1998. (Cited on pages 57, 59, 60, and 137.)
- [70] J. Weber. Gravitational-wave-detector events. *Phys. Rev. Lett.*, 20(23):1307–1308, Jun 1968. (Cited on page 58.)

- [71] E. L. Crow and R. S. Gardner. Confidence intervals for the expectation of a Poisson variable. *Biometrika*, 46:441–453, 1959. (Cited on page 60.)
- [72] H. B. Mann and D. R. Whitney. On a test of whether one of two random variables is stochastically larger than the other. *Ann. Math. Statist.*, 18(1):50–60, 1947. (Cited on page 65.)
- [73] D. Burlon, G. Ghirlanda, G. Ghisellini, J. Greiner, and A. Celotti. Time resolved spectral behavior of bright BATSE precursors. *A&A*, 505:569–575, October 2009. (Cited on page 68.)
- [74] B. Abbott et al. Search for gravitational-wave bursts in the first year of the fifth LIGO science run, 2009. submitted. (Cited on page 69.)
- [75] B. Abbott et al. Search for Gravitational Waves from Low Mass Binary Coalescences in the First Year of LIGO’s S5 Data. *Phys. Rev. D*, 79:122001, 2009. (Cited on pages 72 and 133.)
- [76] Luc Blanchet. Gravitational radiation from post-Newtonian sources and inspiralling compact binaries. *Living Rev. Rel.*, 9:3, 2006. (Cited on page 73.)
- [77] Thomas Cokelaer. Gravitational wave from inspiralling compact binaries: hexagonal template placement and its efficiency in detecting physical signals. *Phys. Rev. D*, 76:102004, 2007. (Cited on page 73.)

- [78] Bruce Allen, Warren G. Anderson, Patrick R. Brady, Duncan A. Brown, and Jolien D. E. Creighton. FINDCHIRP: An algorithm for detection of gravitational waves from inspiraling compact binaries, 2005. (Cited on page 74.)
- [79] C. A. K. Robinson, B. S. Sathyaprakash, and Anand S. Sengupta. Geometric algorithm for efficient coincident detection of gravitational waves. *Phys. Rev. D*, 78(6):062002, 2008. (Cited on pages 74 and 78.)
- [80] Bruce Allen. A  $\chi^2$  time-frequency discriminator for gravitational wave detection. *Phys. Rev. D*, 71:062001, 2005. (Cited on page 77.)
- [81] Andres Rodríguez. Reducing false alarms in searches for gravitational waves from coalescing binary systems. Master's thesis, Louisiana State University, 2007. (Cited on page 77.)
- [82] B. Abbott et al. Search for gravitational waves from binary inspirals in S3 and S4 LIGO data. *Phys. Rev. D*, 77:062002, 2008. (Cited on page 77.)
- [83] S. Golenetskii, R. Aptekar, E. Mazets, V. Pal'Shin, D. Frederiks, T. Cline, A. von Kienlin, G. Lichti, A. Rau, D. Gotz, S. Mereghetti, J. Cummings, S. Barthelmy, N. Gehrels, H. Krimm, K. Hurley, D. M. Smith, R. P. Lin, J. McTiernan, R. Schwartz, C. Wigger, W. Hajdas, A. Zehnder, K. Yamaoka, M. Ohno, Y. Fukazawa, T. Takahashi, M. Tashiro, Y. Terada, T. Murakami, and K. Makishima. IPN localization of very intense short GRB 070201. *GRB Coordinates Network*, 6088:1–+, 2007. (Cited on page 84.)

- [84] D. A. Perley and J. S. Bloom. GRB 070201: proximity of IPN annulus to M31. *GRB Coordinates Network*, 6091:1–+, 2007. (Cited on page 84.)
- [85] V. Pal’Shin. GRB 070201: correction to GCN 6094. *GRB Coordinates Network*, 6098:1–+, 2007. (Cited on page 85.)
- [86] K. Hurley, J. Goldsten, S. Golenetskii, R. Aptekar, E. Mazets, V. Pal’Shin, D. Frederiks, T. Cline, A. von Kienlin, G. Lichti, and A. Rau. IPN triangulation of GRB070201 (refined error box using MESSENGER data). *GRB Coordinates Network*, 6103:1–+, 2007. (Cited on page 85.)
- [87] E. Mazets et al. GRB 070201 IPN error box. Private communication Kevin Hurley and Mazets et al., companion paper, 2007. (Cited on page 85.)
- [88] IPN3. The Third Interplanetary Network (IPN3), 2007. <http://www.ssl.berkeley.edu/ipn3/>. (Cited on page 85.)
- [89] S. Golenetskii, R. Aptekar, E. Mazets, V. Pal’Shin, D. Frederiks, and T. Cline. GRB 070201: clarification on localization and konus-wind spectra. *GRB Coordinates Network*, 6094:1–+, 2007. (Cited on page 85.)
- [90] E. P. Mazets et al. A Giant Flare from a Soft Gamma Repeater in the Andromeda Galaxy, M31, 2007. (Cited on page 86.)
- [91] E. Berger. The Prompt Gamma-Ray and Afterglow Energies of Short-Duration Gamma-Ray Bursts. *Submitted to ApJ [astro-ph/0702694]*, 2007. (Cited on page 85.)

- [92] B. Abbott et al. Search for gravitational waves from galactic and extra-galactic binary neutron stars. *Phys. Rev. D*, 72:082001, 2005. (Cited on page 85.)
- [93] Gregory B. Cook, Stuart L. Shapiro, and Saul A. Teukolsky. Rapidly rotating neutron stars in general relativity: Realistic equations of state. *ApJ*, 424:823, 1994. (Cited on page 111.)
- [94] Ilya Mandel and Richard O’Shaughnessy. Compact Binary Coalescences in the Band of Ground-based Gravitational-Wave Detectors, 2009. (Cited on page 111.)
- [95] S. D. Barthelmy. The GCN website, 2009. <http://gcn.gsfc.nasa.gov/gcn/>. (Cited on page 130.)
- [96] N Kawai et al. GRB051211A (=H3979): Refined Analysis. *GRB Coordinates Network*, 4359:1–+, 2005. (Cited on page 131.)
- [97] L Barbier et al. GRB 070714B, Swift-BAT refined analysis of the short hard burst. *GRB Coordinates Network*, 6623:1–+, 2007. (Cited on page 131.)
- [98] J K Cannizzo et al. GRB 061210: Swift-BAT detection of a short burst. GCN Circular 5904, 2006. (Cited on page 131.)
- [99] B. Abbott et al. Implications for the Origin of GRB 070201 from LIGO Observations. *ApJ*, 681:1419–1428, 2008. (Cited on pages 132 and 134.)

- [100] E. O. Ofek, M. Munro, R. Quimby, S. R. Kulkarni, H. Stiele, W. Pietsch, E. Nakar, A. Gal-Yam, A. Rau, P. B. Cameron, S. B. Cenko, M. M. Kasliwal, D. B. Fox, P. Chandra, A. K. H. Kong, and R. Barnard. GRB 070201: A Possible Soft Gamma-Ray Repeater in M31. *ApJ*, 681:1464–1469, July 2008. (Cited on pages 132 and 142.)
- [101] P. Schady, D. N. Burrows, J. R. Cummings, N. Gehrels, C. Guidorzi, S. T. Holland, S. D. Hunsberger, V. Mangano, D. C. Morris, P. T. O’Brien, C. Pagani, K. L. Page, D. M. Palmer, S. B. Pandey, J. L. Racusin, P. Romano, G. Sato, M. Stamatikos, R. L. C. Starling, D. E. V. Berk, and H. Ziaeepour. GRB 061006: Swift detection of a burst. GCN Circular 5699, 2006. (Cited on page 134.)
- [102] P. Schady, A. Breeveld, T. S. Poole, J. R. Cummings, E. Troja, S. B. Pandey, S. D. Barthelmy, D. N. Burrows, and A. Wells. Swift Observations of GRB 061006. GCN Report 6.1, 2006. (Cited on page 134.)
- [103] B. Abbott et al. Search for gravitational-wave bursts associated with gamma-ray bursts using data from LIGO Science Run 5 and Virgo Science Run 1, 2009. (Cited on page 141.)
- [104] J. Abadie et al. Predictions for the Rates of Compact Binary Coalescences Observable by Ground-based Gravitational-wave Detectors, 2010. (Cited on page 142.)

## Curriculum Vitae

### Title of Dissertation

The search for compact binary coalescence in association with short GRBs with LIGO/Virgo S5/VSR1 data

### Full Name

**Nickolas V Fotopoulos**

### Place and Date of Birth

Omaha, Nebraska, USA

April 23, 1982

### Colleges and Universities

Carnegie Mellon University

Massachusetts Institute of Technology

University of Wisconsin–Milwaukee

### Years attended and degrees

2000–2003, B.S. Physics

2003–2006, S.M. Physics

2006–2010, Ph.D. Physics

## Publications

(bold entries are those for which I was a lead investigator)

34. J. Abadie et al. [LIGO Scientific Collaboration and the Virgo Collaboration] "All-sky search for gravitational-wave bursts in the first joint LIGO-GEO-Virgo run", To appear in *Phys. Rev. D*, (2010). arXiv:01002.1036
33. **J. Abadie et al. [LIGO Scientific Collaboration and the Virgo Collaboration] "Search for gravitational-wave inspiral signals associated with short gamma-ray bursts during LIGO's fifth and Virgo's first science run" To appear in *Astrophys. J.* arXiv:1001.0165**
32. B. P. Abbott et al. [LIGO Scientific Collaboration and the Virgo Collaboration] "Searches for gravitational waves from known pulsars with S5 LIGO data", *Astrophys. J* **713** 671 (2010). arXiv:0909.3583
31. B. Abbott et al. [LIGO Scientific Collaboration and the Virgo Collaboration] "Search for gravitational-wave bursts associated with gamma-ray bursts using data from LIGO Science Run 5 and Virgo Science Run 1.", To appear in *Astrophys. J.*, (2010). arXiv:0908.3824
30. B. Abbott et al. [LIGO Scientific Collaboration and Virgo Collaboration] "An upper limit on the stochastic gravitational-wave background of cosmological origin" *Nature* **460** 990 (2009).
29. B. Abbott et al. [LIGO Scientific Collaboration] "Observation of a kilogram-scale oscillator near its quantum ground state" *New J. Phys.* **11** (2009) 073032
28. B. Abbott et al. [LIGO Scientific Collaboration] "Search for Gravitational Waves from Low Mass Compact Binary Coalescence in 186 Days of LIGO's fifth Science Run", *Phys. Rev. D* **80** (2009) 047101. arXiv:0905.3710

27. B. Abbott et al. [LIGO Scientific Collaboration] “Einstein@Home search for periodic gravitational waves in early S5 LIGO data” *Phys. Rev. D* **80** (2009) 042003. arXiv:0905.1705
26. B. Abbott et al. [LIGO Scientific Collaboration] “Search for gravitational wave ringdowns from perturbed black holes in LIGO S4 data” *Phys. Rev. D* **80** (2009) 062001. arXiv:0905.1654
25. B. Abbott et al. [LIGO Scientific Collaboration] “Search for gravitational-wave bursts in the first year of the fifth LIGO science run” *Phys. Rev. D* **80** (2009) 102001. arXiv:0905.0020
24. B. Abbott et al. [LIGO Scientific Collaboration] “Stacked Search for Gravitational Waves from the 2006 SGR 1900+14 Storm” *Astrophys. J.* **701** (2009) L68-L74. arXiv:0905.0005
23. B. Abbott et al. [LIGO Scientific Collaboration] “Search for High Frequency Gravitational Wave Bursts in the First Calendar Year of LIGO’s Fifth Science Run” *Phys. Rev. D* **80** 102002 (2009), arXiv:0904.4910
22. B. Abbott et al. [LIGO Scientific Collaboration] “First LIGO search for gravitational wave bursts from cosmic (super)strings” *Phys. Rev. D* **80** (2009) 062002 arXiv:0904.4718
21. B. Abbott et al. [LIGO Scientific Collaboration] “Search for Gravitational Waves from Low Mass Binary Coalescences in the First Year of LIGO’s S5 Data” *Phys. Rev. D* **79** 122001, (2009). arXiv:0901.0302
20. B. Abbott et al. [LIGO Scientific Collaboration], “All-sky LIGO Search for Periodic Gravitational Waves in the Early S5 Data” *Phys. Rev. Lett.* **102** 111102 (2009) arXiv:0810.0283

19. B. Abbott et al. [LIGO Scientific Collaboration], "LIGO: The Laser Interferometer Gravitational-Wave Observatory" *Rep. Prog. Phys.* **72** (2009) 076901 arXiv:0711.3041
18. The LIGO Scientific Collaboration, Barthelmy, Gehrels, Hurley, Palmer, "Search for Gravitational Wave Bursts from Soft Gamma Repeaters" *Phys. Rev. Lett.* **101** 211102, (2008). arXiv:0808.2050
17. B. Abbott et al. [LIGO Scientific Collaboration] "Beating the spin-down limit on gravitational wave emission from the Crab pulsar" *Astrophys. J. Lett.* **683** (2008) 45. arXiv:0805.4758
16. **B. Abbott et al. [LIGO Scientific Collaboration] "Implications for the Origin of GRB 070201 from LIGO Observations" *Astrophys. J.* **681** 1419-1428, (2008). arXiv:0711.1163**
15. B. Abbott et al. [LIGO Scientific Collaboration], "First cross-correlation analysis of interferometric and resonant-bar gravitational-wave data for stochastic backgrounds", *Phys. Rev. D*, **76**, (2007) 022001. astro-ph/0703234
14. B. Abbott et al. [LIGO Scientific Collaboration], "Upper limit map of a background of gravitational waves", *Phys. Rev. D* **76** (2007) 082003. astro-ph/0703234
13. B. Abbott et al. [LIGO Scientific Collaboration], "Searching for a Stochastic Background of Gravitational Waves with the Laser Interferometer Gravitational-Wave Observatory", *Astrophys. J.* **659**, 918–930 (2007). astro-ph/0608606
12. B. Abbott et al. [LIGO Scientific Collaboration], "The Einstein@Home search for periodic gravitational waves in LIGO S4 data" *Phys. Rev. D* **79** (2009) 022001 arXiv:0804.1747

11. B. Abbott et al. [LIGO Scientific Collaboration], "All-sky search for periodic gravitational waves in LIGO S4 data", *Phys. Rev. D* **77** (2008) 022001. arXiv:0708.3818
10. **N. Fotopoulos for the LIGO Scientific Collaboration "Searching for stochastic gravitational-wave background with the co-located LIGO interferometers."**, *J. Phys. Conf. Ser.* **122** 012032, (2008). arXiv:0801.3429
9. B. Abbott et al. [LIGO Scientific Collaboration], "Search for gravitational waves from binary inspirals in S3 and S4 LIGO data" *Phys. Rev. D* **77** (2008) 062002 arXiv:0704.3368
8. B. Abbott et al. [LIGO Scientific Collaboration], "First joint search for gravitational-wave bursts in LIGO and GEO600 data" *Class. Quantum Grav.* **25** (2008) 245008 arXiv:0807.2834
7. B. Abbott et al. [LIGO Scientific Collaboration], "Search for Gravitational Waves Associated with 39 Gamma-Ray Bursts Using data from the Second, Third, and Fourth LIGO Runs" *Phys. Rev. D* **77** (2008) 062004 arXiv:0709.0766
6. B. Abbott et al. [LIGO Scientific Collaboration], "A Joint Search for Gravitational Wave Bursts with AURIGA and LIGO." *Class. Quant. Grav.* **25** (2008) 095004 arXiv:0710.0497
5. B. Abbott et al. [LIGO Scientific Collaboration], "Search of S3 LIGO data for gravitational wave signals from spinning black hole and neutron star binary inspirals." *Phys. Rev. D* **78** (2008) 042002 arXiv:0712.2050
4. B. Abbott et al. [LIGO Scientific Collaboration], "Upper Limits on Gravitational Wave Emission from 78 Radio Pulsars", *Phys. Rev. D* **76** (2007) 042001. gr-qc/0702039

3. B. Abbott et al. [LIGO Scientific Collaboration], "Search for gravitational-wave bursts in LIGO data from the fourth science run", *Class. Quant. Grav.* **24** (2007) 5343-5369. arXiv:0704.0943
2. B. Abbott et al. [LIGO Scientific Collaboration], "Search for gravitational wave radiation associated with the pulsating tail of the SGR 1806-20 hyperflare of December 27, 2004 using LIGO", *Phys. Rev. D* **76** (2007) 062003. astro-ph/0703419
1. **N. Fotopoulos for the LIGO Scientific Collaboration, "Identifying correlated environmental noise in co-located interferometers with application to stochastic gravitational wave analysis." *Class. Quant. Grav.* 23 S693-S704, (2006).**

#### Awards and Fellowships

- 2009–10 Papastamatiou Scholarship for Theoretical Physics
- 2009–10 UWM Dissertator Fellowship
- 2008–09 UWM Graduate School Fellowship
- 2006–10 UWM Chancellor's Graduate Student Fellowship

#### Major Department

Physics

---

Professor Jolien Creighton

Date